12-2016

On the use of mechanical and acoustical excitations for selective heat generation in polymer-bonded energetic materials

Daniel C. Woods
Purdue University

PURDUE UNIVERSITY
GRADUATE SCHOOL
Thesis/Dissertation Acceptance

This is to certify that the thesis/dissertation prepared

By Daniel Curtis Woods

Entitled

On the Use of Mechanical and Acoustical Excitations for Selective Heat Generation in Polymer-Bonded Energetic Materials

For the degree of Doctor of Philosophy

Is approved by the final examining committee:

Jeffrey F. Rhoads Co-chair	Ronald G. Reifenberger
J. Stuart Bolton Co-chair	
Patricia Davies	
Charles M. Krousgrill	

To the best of my knowledge and as understood by the student in the Thesis/Dissertation Agreement, Publication Delay, and Certification Disclaimer (Graduate School Form 32), this thesis/dissertation adheres to the provisions of Purdue University's "Policy of Integrity in Research" and the use of copyright material.

Approved by Major Professor(s): Jeffrey F. Rhoads

Approved by: Jay P. Gore 11/8/2016

Head of the Departmental Graduate Program Date

ON THE USE OF MECHANICAL AND ACOUSTICAL EXCITATIONS FOR SELECTIVE HEAT GENERATION IN POLYMER-BONDED ENERGETIC MATERIALS

A Dissertation

Submitted to the Faculty

of

Purdue University

by

Daniel C. Woods

In Partial Fulfillment of the

Requirements for the Degree

of

Doctor of Philosophy

December 2016

Purdue University

West Lafayette, Indiana

ACKNOWLEDGMENTS

This research was supported primarily by the U.S. Office of Naval Research through ONR grant no. N00014-10-1-0958 as a Multidisciplinary University Research Initiative on "Sound and Electromagnetic Interacting Waves." Parts of the research were also supported by the U.S. Air Force Office of Scientific Research through award no. FA9550-15-1-0102 and by the U.S. Office of Naval Research through ONR grant no. N00014-16-1-2275.

TABLE OF CONTENTS

Page

LIST OF FIGURES

Figure Page

Figure Page

Figure Page

Figure Page

Figure Page

ABSTRACT

Woods, Daniel C., Ph.D., Purdue University, December 2016. On the Use of Mechanical and Acoustical Excitations for Selective Heat Generation in Polymer-Bonded Energetic Materials. Major Professors: Jeffrey F. Rhoads and J. Stuart Bolton, School of Mechanical Engineering.

To address security issues in both military and civilian settings, there is a pressing need for improved explosives detection technologies suitable for trace vapor detection. In light of the strong dependence of vapor pressure on temperature, trace vapor detection capabilities may be enhanced by selectively heating target materials by external excitation. Moreover, polymer-bonded energetic materials may be particularly susceptible to heating by mechanical or acoustical excitation, due to the high levels of damping and low thermal conductivities of most polymers. In this work, the thermomechanical response of polymer-based energetic composites and methods for acoustical excitation are investigated in order to improve the understanding of the temperature rises induced by applied excitation, and to uncover waveforms which may efficiently transmit excitation energy to generate heat and enhance trace vapor detection capabilities.

The heat generation in the binder material of energetic and surrogate systems under harmonic excitation was investigated analytically through the application of a viscoelastic material model. Specifically, structural-scale heating was considered under low-frequency direct mechanical excitation as applied to a beam geometry. Experiments were conducted with a mock mechanical material, wherein the mechanical and thermal responses were recorded by scanning laser Doppler vibrometry and infrared thermography, respectively. Direct comparisons between the model and experimental results demonstrated good agreement with the predicted response, with low-order, bulk-scale heating observed along the modal structure in areas of higher

strains. In addition, localized heating near individual crystals was investigated analytically by extending the viscoelastic heating model to general three-dimensional stress-strain states. Application of the model to a Sylgard® 184 binder system with an embedded HMX (octogen) crystal under ultrasonic excitation revealed predictions of significant heating rates, particularly near the front edge of the crystal, due to the wave scattering and the resulting stress concentrations.

In considering methods for such excitation through incident acoustical or ultrasonic waves, the form of the wave profile was tuned in this work for the purpose of maximizing the energy transmission into solid materials. That transmission is generally limited by the large impedance mismatch at typical fluid–solid interfaces, but by varying the spatial distribution of the incident wave pressure, significant transmission increases can be achieved. In particular, tuned incident inhomogeneous plane waves were found to predict much lower values of the reflection coefficient, and hence large increases in the energy transmission in the context of lossless and low-loss dissipative media. Also, material dissipation was found to have a strong effect on the optimal incident waveform, generally causing a shift to lower inhomogeneity values. Similar results were obtained for parameterized forms of bounded incident waves with respect to the local reflection phenomena and surface wave excitation. These results suggest that, depending on the targeted solid material, substantial energy transmission and heat generation increases may be achieved by tailoring the spatial form of the incident wave profile.

1. INTRODUCTION

To address security concerns in both military and civilian settings, there is an urgent need for improved technologies for detecting explosive materials. In particular, improvised explosive devices (IEDs) are a pervasive and growing threat, and present a number of challenges to detection. For one, the composition of IEDs varies widely, as their construction is limited by the available materials and ease of preparation [1–4]. As a result, such devices often contain components and materials that are not common in military or commercial explosives, which may render detection methods for common explosives ineffective. In addition, the composition of IEDs varies from region to region and evolves over time as countermeasures are implemented, which presents further challenges to detection.

A wide array of detection methods are currently in use, which may be broadly divided into those which seek to detect bulk explosive materials or components, and those which attempt to sense trace material, whether deposited on a given surface or in the form of vapors in the surrounding air [1–3, 5]. For the detection of bulk explosives, x-rays, infrared waves, neutron beams, terahertz lasers, and other types of interrogation have been employed to produce subsurface images that may be used to identify suspicious objects [1, 5–7]. However, these methods are often severely limited by metal barriers, which can prevent effective imaging. Similarly, methods which identify circuitry elements that may be indicative of explosive devices, such as metal detectors or non-linear junction detectors, suffer from an inability to distinguish between IED components and parts of common, innocuous electronic devices [1, 5, 8].

In light of the limitations of bulk detection systems, much of the recent and current research has focused on methods for trace detection [2, 3, 9, 10]. Trace material may be deposited on a surface during the preparation or packaging of an explosive, and vapors associated with the material may exist in the surrounding air. Recent efforts

have focused on improving the sensitivity of trace detection methods, as low amounts of deposited material or low vapor concentrations can render detection impossible. Of particular note for this work is the observation of the strong dependence of vapor pressures on temperature, which suggests that if temperatures of explosive materials could be increased in a controlled manner (and prior to deflagration or detonation), then the resulting increase in vapor pressure may better facilitate the detection of trace vapors.

1.1 Brief Review of Trace Detection Technologies

Trace detection of explosives is an active area of research, with many recent advances [2, 3, 9, 10]. The existing methods for trace detection can be divided into those which attempt to sense material deposited on surfaces, whether by swabbing the surface or by non-contact spectroscopic methods, and those which attempt to detect associated vapors in the surrounding air.

Methods of trace detection which attempt to sense deposited material, or surface residue, often do so by swabbing surfaces which may have come into contact with the explosive. The obtained surface sample is then analyzed by techniques such as mass spectrometry [11, 12] or ion mobility spectrometry [13–15], or by other chemical methods [16, 17]. However, in light of recent advances, non-contact methods for detecting surface residue, which use laser-based excitation and spectroscopic methods, have become more prominent [3, 9, 10]. These methods seek to leverage characteristics in the scattered spectrum which may be indicative of target species. Examples include Infrared Absorption Spectroscopy [9, 18], Raman Spectroscopy [19–21], and terahertz-range methods [22–24], the interest in which has especially grown in recent years. Deposited materials on surfaces usually offer higher concentrations than do surrounding vapors and, as such, surface residue detection methods have the advantage of good sensitivity and selectivity as compared to trace vapor detection methods. However, methods which swab the surface require direct contact with the device or

packaging, which is often not possible, and may be hazardous depending on the material's volatility. Similarly, the spectroscopic methods, which are especially hampered by metal barriers, generally require direct visual access, and also may be of limited utility for composite materials, whose structures interfere with the desired scattering characteristics. Perhaps most importantly, surface residue methods are dependent on the presence of the material on the interrogated surfaces, which may be absent if the deposits are allowed to evaporate over time or if care is taken in the preparation, packing, and cleaning of the device.

On the other hand, trace vapor detection methods attempt to detect saturated vapors in the vicinity of explosive materials. The use of trained animals remains the most sensitive means of detecting trace vapors [2, 3, 10]. Dogs, as the gold standard in sensitivity in detection, have been the most commonly employed, but rats, honey bees, and moths have also been successfully trained and deployed [25–27]. Other methods of trace vapor detection directly sample the surrounding air and identify present species in conjunction with methods such as gas chromatography or mass spectroscopy [28–31]. However, these approaches generally require extensive preconcentration methods, due to the low concentrations of vapors, and still yield samples below the detection limits for some explosives, including RDX, HMX (octogen), and pentaerythritol tetranitrate (PETN) [1, 2]. In addition, micro- and nano-scale devices have been investigated for detection on the basis of changes in the resonant behavior of, for example, microcantilevers in the presence of such vapors [32, 33].

Trace vapor detection suffers from, as mentioned above, low vapor concentrations, particularly as the distance from the surface of the explosive increases [1–3]. This issue is exacerbated if the explosive material is sealed or packed in a bag, as is often the case, which causes severe decreases in vapor pressures. In addition, the pressures may also drop significantly in certain environmental conditions, such as in the presence of strong winds or at lower temperatures [1]. However, provided these issues in sensitivity can be addressed, trace vapor methods offer the possibility of detection from a safe, standoff distance and do not require direct visual access to the

sample. The prospect of selective heating of target explosives, also preferably from a standoff distance, may help to address the low vapor concentrations by increasing the temperatures and vapor pressures of these materials.

1.2 Vapor Pressure Dependence on Temperature

A recent review of the vapor pressures of many common explosives was presented by Östmark et al. [4], including for RDX, HMX, ammonium perchlorate (AP), PETN, acetone peroxide (TATP), trinitrotoluene (TNT), and nitroglycerin (NG), among others. The vapor pressures of all of the explosive materials were shown to increase dramatically with temperature. For example, the vapor pressure of RDX, referenced at 25 °C, increases by approximately 40% with a 2 °C increase in temperature and by nearly 430% with a 10 °C increase. The increase in vapor pressure for HMX is even more dramatic, with increases of approximately 60% for a 2 °C increase in temperature and 880% for a 10 °C increase, again referenced to 25 °C. The aggregated vapor pressure vs. temperature plots for RDX and HMX as presented by Östmark et al. [4] are shown in Figures 1.1(a) and 1.1(b), respectively.

If it is sought to selectively heat explosives for the purpose of increasing the vapor pressures, polymer-bonded explosives may be especially susceptible to temperature increases induced by external excitations. Due to the large levels of internal dissipation and poor thermal conductivities of most polymers, significant heat is generated when polymer-based materials are subjected to intensive loading [34–37]. Moreover, though considerable variation exists in the composition of explosive materials, particularly improvised explosives, many traditional energetic compositions consist of a polymer-based binder with embedded energetic crystals. Examples include RDX in polystyrene, HMX in polyurethane rubber, and PETN in Sylgard®. In light of the vapor pressure dependence on temperature and the heat generation exhibited under mechanical excitation, the thermomechanics of polymer-based materials present an intriguing pathway to increased vapor pressures and improved detection capabilities.

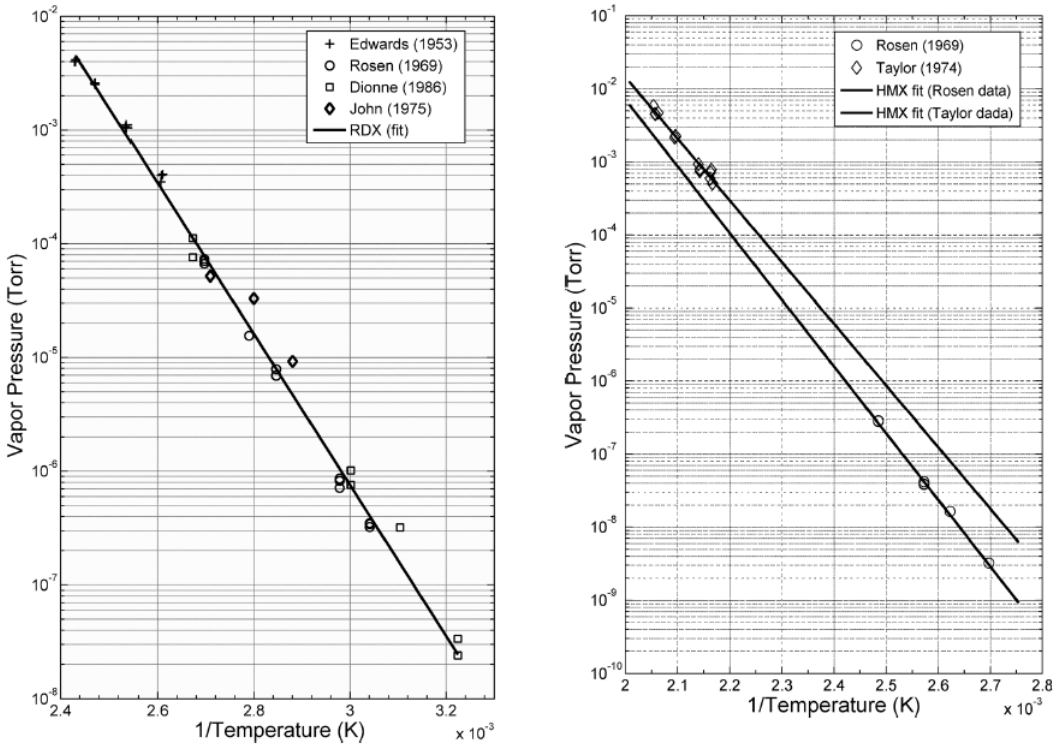

(a) (b)

Figure 1.1. The vapor pressure dependence of (a) RDX and (b) HMX as presented in the review by Östmark et al. [4].

Furthermore, such an approach, if viable, may be applied rather broadly to the large class of polymer-bonded explosives.

1.3 Thermomechanical Response to Applied Excitation

Applied mechanical and acoustical excitations were considered for the purpose of eliciting thermal responses in polymer-bonded energetic materials. Direct mechanical excitation was studied prior to standoff acoustical or ultrasonic excitation in order to isolate the thermomechanical behavior of these materials. That is, this portion of the work sought to ascertain an understanding of the induced deformations and elicited temperature distribution under a known applied dynamic stress distribution,

as distinct from the fluid–solid interface phenomena that play an important role in acoustical excitation. The purpose of this section is to give an introduction to the methods for heat generation by applied excitation, particularly through low-frequency mechanical excitation on the order of the structure's primary resonance and through high-frequency contact excitation.

Heat generation elicited by mechanical or acoustical excitation is well-documented. Thermomechanical coupling in the presence of mechanical or thermal loading, or both, is described by the thermodynamic theory of solids, which accounts for both irreversible (e.g., material damping) and reversible (e.g., thermoelastic) effects [38]. This coupling is commonly exploited for nondestructive testing in the field of vibrothermography [39–42] by applying acoustical or ultrasonic excitation to samples to elicit thermal responses. Since temperature excursions are noted near stress concentrations, thermal imaging can be used to identify defects in the structure.

Heat is also generated on a bulk scale within samples under external loading due to material damping, as energy losses caused by internal dissipation are converted to heat. Since greater heat generation is observed in areas of higher stress, the elicited temperature distributions are dependent on modal structures. For example, Dimarogonas and Syrimbeis studied the heat generated along the modal structures of vibrating metal plates [43]. In the case of polymers, the effect is even more pronounced, attributable to the large levels of internal damping and poor thermal conductivities. This was demonstrated in the seminal studies by Ratner and Korobov [34, 35], and in numerous subsequent experiments, e.g. [44].

Moreover, similar results have been observed for polymer-based composites. Katunin and Fidali, for instance, conducted experiments with glass fiber-reinforced laminate plates and observed significant heating along modal structures near resonance [45, 46]. In the context of particulate composites, the effect of the particle/binder ratio on material properties has been studied as well [47–52]. Changes in the damping properties with increasing particle/binder ratio have been attributed to mismatched thermal expansion coefficients [47] and to particle-scale interactions of the crystals [52].

For explosive materials, however, few studies have considered the heat generation as a function of the excitation parameters and material composition. The works of Loginov [53, 54], which focus on the response of explosives to mechanical vibration, shed light on the nature of the heating, but are largely phenomenological in nature and do not address frequency-selective excitation.

In the case of polymer-bonded energetic materials, the composite nature may provide a pathway to heating in addition to the bulk-scale thermal response elicited along the modal structure. In particular, the scattering of elastic waves at individual crystals, which may be induced through mechanical or acoustical excitation, may result in stress concentrations that contribute significantly to the generation of hot spots within the energetic material. This effect has recently been investigated experimentally for samples consisting of a polymer-based binder material and discrete numbers of embedded energetic crystals subjected to ultrasonic excitation [55–58]. Substantial heating was observed over short time scales in those investigations, with the response attributed to both bulk heating of the binder material and crystal-scale effects inclusive of the scattering at the crystal–binder interface. Moreover, the generation of hot spots near energetic crystals, particularly at stress concentrations due to defects or voids, has long been considered a cause for the initiation of deflagration or detonation events in composite explosives [59–62].

In considering the underlying mechanical behavior of polymer-based materials, a viscoelastic model is generally employed to obtain the stress-strain relationship [63–65]. For a linear viscoelastic model and considering only the steady-state response to harmonic loading, the stress and strain can be approximated as harmonically-varying with the same frequency as the forcing, but with the strain lagging behind the stress by a phase difference. The stress and strain time histories under this assumption are shown in the conceptual diagram in Figure 1.2 for one-dimensional loading. The associated hysteretic damping behavior can be used to approximate the heat generated per unit volume by computing the area under the hysteresis loop on the stress-strain plot, which yields the loss in the strain energy density, or the volumetric

energy generation (assuming the mechanical losses are converted to heat), per cycle [65]. This result can be extended to three-dimensional stress-strain states through the application of the generalized Hooke's law for linear viscoelastic media [66], and the net loss in the strain energy density is given by the sum of the contributions from the individual stress-strain components. Provided that the temperature varies on a much slower order than the mechanical forcing, this can be time-averaged to yield the volumetric energy generation rate [37]. The energy generation rate can then be used in conjunction with an appropriate heat transfer equation, such as the Fourier Law of Conduction, and numerical solvers to predict the temperature evolution and distribution within polymer-based samples.

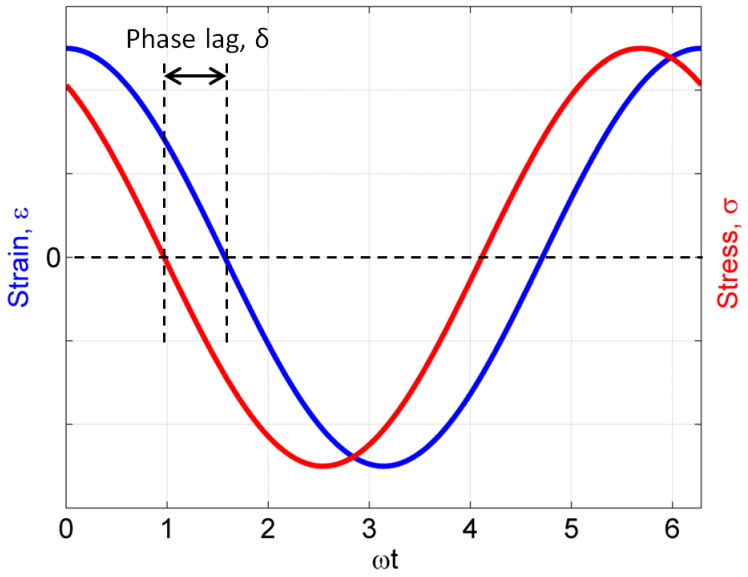

Figure 1.2. A conceptual diagram of the stress-strain phase lag in the steady-state response to one-dimensional, harmonic loading with a linear viscoelastic model. For the horizontal axis, ω denotes the angular frequency and t denotes the time variable.

In order to maximize the heat generated on the structural scale, it is clear that the excitation should be near the sample's primary resonance. At the resonance, the response amplitudes and, consequently, the stresses and elicited temperature increases are greatest. It should also be noted that the material moduli generally depend on the

frequency, which may have a sizable effect if large frequency ranges are considered [64, 65]. In the experimental investigations of heat generation in this work, a mechanical mock material intended to resemble common polymer-bonded energetic materials was used. The mixture consisted of a hydroxyl-terminated polybutadiene (HTPB) binder, commonly used in energetic composites, with embedded ammonium chloride (NH_4Cl) crystals in various volume ratios. The NH_4Cl crystals were selected to approximate the particle sizes of energetic crystals such as ammonium perchlorate (AP). Representative samples are shown in Figure 1.3. The cylindrical sample shown along with the beam and plate in Figure 1.3(a) was used by a colleague in related experiments which sought to measure the material properties of the composition [51]. Note that the samples are qualitatively similar to hard rubber- or soap-like materials in terms of their bending stiffness. Also note the rough texture of the samples, as is evident in the close-up image of the beam in Figure 1.3(b).

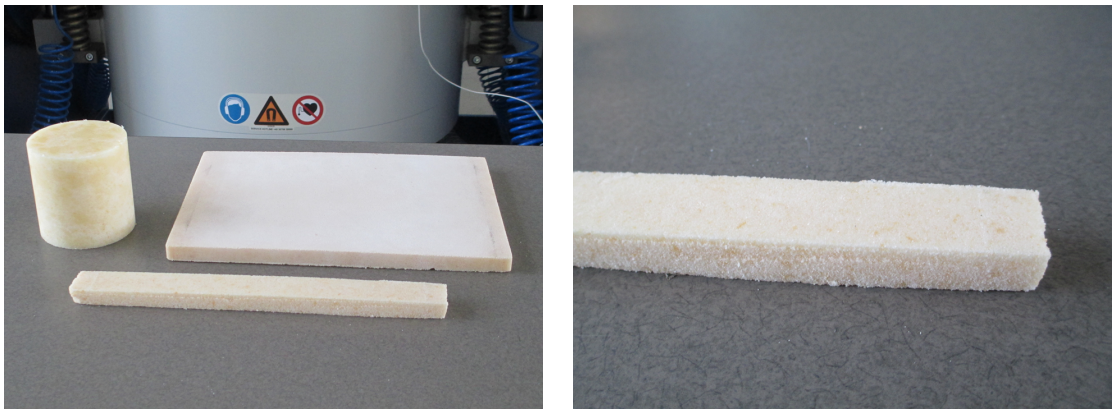

(a) (b)

Figure 1.3. Samples of the mechanical mock material presented as (a) several geometries and (b) a close-up of the beam sample. The composition consists of a hydroxyl-terminated polybutadiene (HTPB) binder with embedded ammonium chloride (NH_4Cl) crystals.

With reference to the loading which targets heating on the particle-scale, ultrasonic excitation was considered since, in the context of elastic wave propagation induced through contact transducers, greater heat generation rates can be achieved

at higher frequencies. Moreover, these greater levels of heating have facilitated experimental studies by colleagues on hot spot generation in polymer-bonded energetic materials [44, 55, 58], for which the considerations of the present work provide an analytical basis for the viscoelastic heating of the binder material, including in the presence of stress concentrations at an embedded crystal.

1.4 Methods for Acoustical Excitation

Due to the hazards associated with explosive materials, it is preferable that excitation and detection be done from a safe, standoff distance. As such, acoustical excitations were studied for the purpose of generating heat in, and increasing the vapor pressures of, polymer-bonded energetic materials. The attenuation in air increases dramatically with frequency, and also depends on factors that include the temperature, pressure, relative humidity, and carbon dioxide content [67–69]. The attenuation, or absorption, coefficient as a function of frequency and for several discrete values of the relative humidity is shown in Figure 1.4, as presented by Bass et al. [69], based on empirical formulas. In light of this dependence, low-frequency acoustical excitations up to a few kHz may be considered to allow for reasonable transmission distances in air and penetration through metal barriers. Higher-frequency wave profiles, however, may be generated remotely on solid surfaces by laser-based methods to induce elastic wave propagation, by air-coupled systems, and by other approaches [70–76], though such methods are generally severely limited by metal barriers. The purpose of this section is to give an introduction to the methods for increased energy transmission by tuning the spatial profile of incident acoustic waves, particularly with regard to air–solid interfaces.

Since most liquid and solid materials have densities and wave speeds which far exceed those of air, stress and energy transmission by acoustic waves across typical air–liquid and air–solid interfaces is limited by substantial reflection and refraction at the interface surface [77, 78]. Moreover, for homogeneous incident plane waves and in

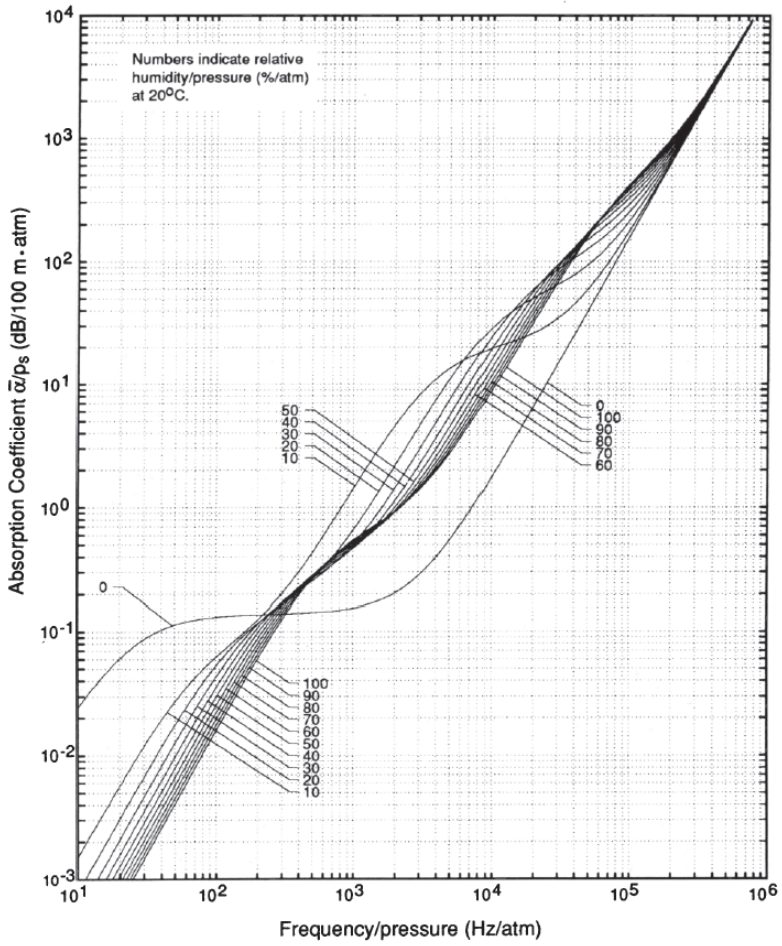

Figure 1.4. The attenuation coefficient in air as a function of frequency and relative humidity as presented by Bass et al. [69]. The curves correspond to values of the relative humidity in %, as marked. The results scale with the pressure, as indicated by the axes labels. All curves are taken at 20 °C.

the absence of material dissipation, no energy can be transmitted above the critical angle for the interface, which is rather small when there are large differences in the wave speeds among the two media. However, when inhomogeneous or evanescent plane waves are incident at such interfaces, a bulk wave is transmitted even above the critical angle, which provides a mechanism for energy propagation below the interface.

Transmission across high impedance-difference interfaces has been studied in a number of contexts, including for the possible detection of aircraft by underwater

sensors [79, 80], to assess the impact of man-made noise on marine life [81], and in evaluating the effect of sonic booms on ground pressure patterns and building structures [82–84]. Extensive studies have been conducted on the air–water interface [79, 80, 85–89], in particular, due to its significance in naval applications. For example, Urick [79, 80] presented significant contributions on underwater sound propagation and Chapman et al. [85, 86] developed a normal mode theory for transmission into water from a homogeneous atmosphere. Subsequent studies on the air–water interface have extended those results, accounting for increased complexity in the environmental conditions or in the source. In the context of both liquid and solid interfaces, Godin [90–92] and others [93, 94] have studied conditions for anomalous transparency with a source situated in the higher-impedance material (i.e., in the liquid or solid) within a wavelength of the interface, with the perfect transmission into air attributable to the interaction of the inhomogeneous wave components at the surface. However, this cannot be exploited with the source instead located in air, as the wave speed in the liquid or solid on the transmission side of the interface would exceed that on the incident side.

Inhomogeneous, or evanescent, plane waves are of particular interest for energy transmission across high impedance-difference interfaces because, as noted, bulk transmitted waves (which are also inhomogeneous) are generated even above the critical angle. In contrast, only surface waves are generated in an elastic solid (or in a lossless fluid) if the incident wave is homogeneous and above the critical angle [77, 78]. For evanescent plane waves in lossless media, the planes of constant phase are perpendicular to the planes of constant amplitude. The pressure field of a homogeneous plane wave in a lossless medium is shown conceptually in Figure 1.5(a), and an evanescent plane wave is shown in Figure 1.5(b), with an arbitrary rate of decay for the evanescent wave. Each wave propagates from left-to-right in Figure 1.5 and, for the homogeneous wave in Figure 1.5(a), the wavefronts propagate with no decay along the propagation direction nor perpendicular to that direction. In contrast, for the evanescent wave, the amplitude of the pressure decays along a line perpendicular to

the direction of propagation (i.e., along the vertical direction), as is evident in Figure 1.5(b). When material losses are included, a component of amplitude decay in the direction of propagation (i.e., due to dissipation) must also be included for both homogeneous and inhomogeneous plane waves [66, 78]. Thus, for the case of inhomogeneous waves in dissipative media, the angle of amplitude decay relative to the propagation direction, known as the "degree of inhomogeneity," always lies between 0° and 90°.

Low-frequency inhomogeneous waves of the type discussed here can be generated by various methods [95–99]. For instance, homogeneous plane waves can be passed through a triangular prism made of an absorbing material [97]. Due to the different path lengths through the absorbing prism, decay of the amplitude of the transmitted wave is achieved perpendicular to the direction of propagation. More generally, the spectral division method can be applied with phased arrays of sources to reproduce the desired propagation and decay characteristics [98]. However, for waves in the ultrasonic regime, due to the large attenuation coefficients in air at higher frequencies, alternate methods, such as laser-based phased arrays [70, 73, 76], would need to be employed for non-contact excitation at appreciable standoff distances.

The theory of the energy flux of evanescent waves was studied by Hayes [100], and energy conservation was verified by Leroy et al. [101] in the context of lossless, homogeneous, isotropic fluid–fluid and fluid–solid interfaces. The reflection and refraction phenomena occurring at these interfaces in the presence of incident evanescent plane waves have been investigated as well [97, 101]. Of particular note in these studies is the minimum of the reflection coefficient which is observed at the Rayleigh angle for air–solid interfaces. At this angle, the spatial resonance of coupled longitudinal and shear motions in the solid is excited by the incident wave. Consequently, the transmitted intensity is maximized, where energy propagates below the interface by means of the transmitted bulk longitudinal and shear waves. As adapted from Leroy et al. [101], Figure 1.6(a) shows the magnitude of the reflection coefficient for an incident homogeneous plane wave, and Figure 1.6(b) for an incident evanescent plane

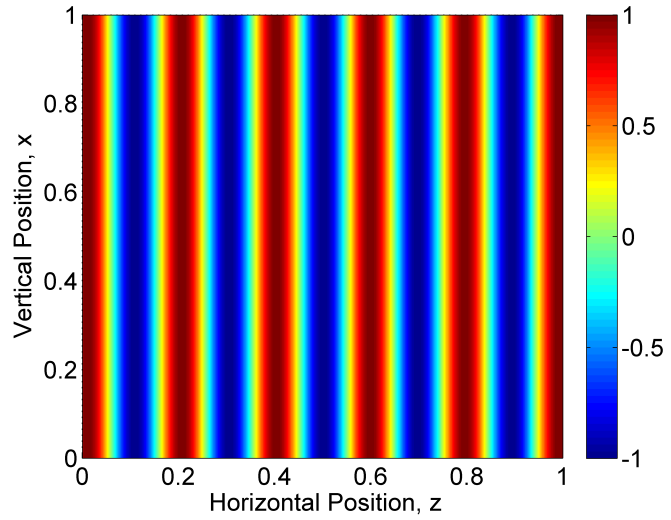

(a)

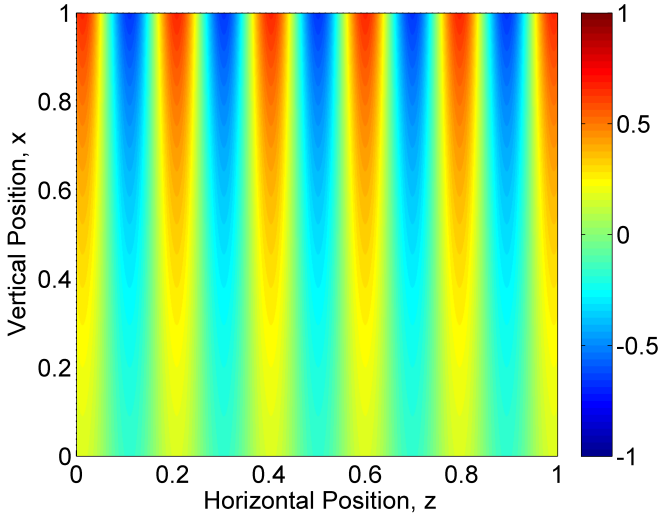

(b)

Figure 1.5. The pressure field, shown conceptually, of a plane wave propagating in a lossless medium with the wave as (a) homogeneous and (b) evanescent, or inhomogeneous. Arbitrary scalings are used for the purpose of illustration.

wave, where the "dip" in the reflection coefficient is observed. Note that, for the homogeneous incident wave in Figure 1.6(a), no distinct minimum in the reflection

coefficient is observed since, above the critical angle, the energy of the surface wave is reradiated into the fluid to yield total internal reflection.

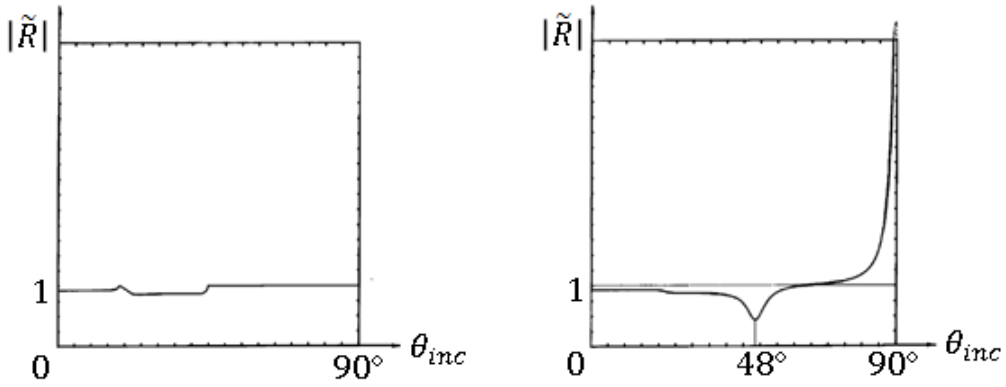

(a) (b)

Figure 1.6. The magnitude of the reflection coefficient $|\tilde{R}|$ at an air–solid interface as a function of the incidence angle θ_{inc} with the incident plane wave as (a) homogeneous and (b) evanescent, or inhomogeneous, as adapted from Leroy et al. [101]. The Rayleigh angle for the interface is approximately 48°.

The extension from the theory for lossless media to that for dissipative media is generally implemented by assuming a hysteretic damping model, as for linear viscoelastic materials [64–66]. With the material further assumed to be homogeneous and isotropic, the phase and attenuation relations, as well as the energy fluxes, of inhomogeneous plane waves (including both longitudinal and shear waves) have been described in detail by Borcherdt [66, 102, 103] and others [104, 105]. The reflection and refraction phenomena of inhomogeneous waves at material interfaces, where linear viscoelastic or fluid media occupy the two semi-infinite half-spaces, have also been described [66, 106–110]. Notably, except for the special case of equal dissipation in the two media, the transmitted waves are found to be inhomogeneous even when the incident wave is homogeneous, and transmission is likewise maximized at the Rayleigh angle, where the transmitted longitudinal and shear motions on the solid

surface are coincident [66, 111, 112]. Moreover, the fraction of the incident energy that is transmitted is again maximized when the reflection coefficient is minimized.

Though the interface phenomena for incident plane waves provide insight into the acoustic wave profiles which optimize the energy transmission into solid materials, bounded waves must be employed in practice. Transmission by bounded incident waves having a Gaussian profile, particularly the excitation of Rayleigh-type surface waves on the solid surface, has previously been considered in depth [111, 113–116]. However, broadly speaking, little attention has been given to other waveforms and to the effect of tuning the waveform to enhance the energy transmission or surface wave excitation efficiency at fluid–solid interfaces. To this end, Vanaverbeke et al. [117] considered more general incident wave profiles, termed "bounded inhomogeneous waves," where a component of exponential decay was introduced perpendicular to the propagation direction and the well-known Fourier method was applied to decompose the profile into plane wave components. Their work drew a strong connection between the reflection and transmission of the bounded incident waves at the fluid–solid interface and inhomogeneous plane wave theory, where the local reflection coefficient in the specular direction was observed to remain close to that predicted by plane wave theory, particularly for larger beamwidths. More importantly, it was shown that the surface wave excitation efficiency for the bounded inhomogeneous incident waves was considerably higher than that for Gaussian and square profiles. Though Vanaverbeke et al. [117], along with others [118, 119], have given a detailed account of the effects of the frequency, beamwidth, and steepness of the incident profiles, they have not reported tuning the decay parameter to improve the surface wave excitation efficiency.

In the present work, the previous investigations highlighted above are extended by varying the inhomogeneity of plane waves and the analogous exponential decay of bounded incident waves to uncover incident wave profiles which enhance the energy transmission into solid materials. In particular, in the context of plane waves, by tuning the incidence angle and decay rate of the incident inhomogeneous wave,

parameters can be found, for any elastic solid, which yield no reflection of the incident wave. That is, the impedance of the incident wave is matched exactly by the contributions of the transmitted longitudinal and shear waves. This condition yields substantial increases in the energy transmission, since none of the incident energy normal to the interface is reflected. Moreover, analogous results are observed for dissipative media and for bounded incident waves.

1.5 Overview of Dissertation

In Chapter 2, an analytical model for the deflection and volumetric heat generation within a polymer-based beam subjected to direct harmonic excitation is presented, where a linear viscoelastic material model is assumed. The temperature evolution and distribution is recovered through the use of numerical solvers with the analytical heat generation term. Model predictions for the beam deflection and temperature field are compared with experiments on a surrogate material, a beam composed of an HTPB binder with embedded NH_4Cl crystals (75% crystal by volume). The viscoelastic heating model is extended in Chapter 3 to general three-dimensional stress-strain states. The model is then applied to a composite system consisting of a single energetic crystal embedded in a large viscoelastic binder medium. A numerical solution method is again applied to recover the temperature solution over a finite time interval, and the effects of the excitation amplitude and frequency are discussed as well.

Chapters 4, 5, and 6 focus on acoustic wave profiles which enhance the energy transmission at fluid–solid interfaces, as compared to more commonly-studied waveforms. Chapter 4 presents the interface theory for inhomogeneous plane waves in lossless media, and the conditions for zero reflection at the interface (and consequently total transmission of the normal incident energy) are considered. Chapter 5 extends the discussion in Chapter 4 to include material dissipation, which has implications for the types of plane waves which may propagate and for the conditions of minimal reflection at the fluid–solid interface. Chapter 6 then extends the results to

bounded wave profiles, which have been effectively windowed in space and contain an exponentially decaying term corresponding to that of inhomogeneous plane waves. For the bounded profiles, results for the local reflection coefficient and surface wave excitation efficiency at the interface are analogous to the results presented for plane waves. Finally, Chapter 7 summarizes the contributions of this work and suggests several directions for subsequent research.

2. THERMOMECHANICAL RESPONSE OF A POLYMER-BASED PARTICULATE COMPOSITE BEAM SUBJECTED TO DIRECT MECHANICAL EXCITATION

2.1 Introduction

Though explosives detection capabilities may be significantly enhanced by heating the target material (due to the strong dependence of vapor pressure on temperature), the elicited thermal response under mechanical loading has not previously been studied in depth for the class of polymer-bonded energetic materials. The purpose of this chapter is thus to characterize the thermomechanical response of a polymeric particulate composite material subjected to mechanical excitation. Specifically, a viscoelastic model is applied to predict the thermomechanical behavior of an HTPB beam with embedded NH_4Cl crystals subjected to harmonic mechanical loading near the primary structural resonance to maximize the self-heating. The sample composition, as highlighted in Section 1.3, is a mock mechanical material intended to resemble common polymer-bonded energetic materials. An analytical model, based on classical Euler-Bernoulli beam theory and a homogenized linear viscoelastic material model, is presented for the volumetric heat generation and used with numerical solvers to compute the temperature distribution and evolution in the beam. The model predictions are subsequently compared to the thermal and mechanical responses of the experimental sample, which are recorded using infrared thermography and scanning laser Doppler vibrometry, respectively. Major portions of this chapter first appeared in the Proceedings of the ASME 2014 International Design Engineering Technical Conferences & Computers and Information in Engineering Conference [120], and subsequently in the Journal of Vibration and Acoustics [121]. This work was completed in conjunction with Jacob K. Miller.

2.2 Viscoelastic Behavior of Polymers Subjected to Harmonic Excitation

Polymers subjected to time-varying loading can be described by a viscoelastic model [63–65]. In general form, the one-dimensional stress-strain relationship for linear viscoelastic materials involves successive time derivatives of both stress and strain [65], according to:

$$M_0\sigma + M_1\frac{\partial\sigma}{\partial t} + M_2\frac{\partial^2\sigma}{\partial t^2} + ... = N_0\epsilon + N_1\frac{\partial\epsilon}{\partial t} + N_2\frac{\partial^2\epsilon}{\partial t^2} + ..., \tag{2.1}$$

where $\sigma(t)$ and $\epsilon(t)$ are the stress and strain histories, respectively, and the M_i and N_i are material parameters.

Though the representation as a differential equation is general, a more convenient approach is the hereditary integral method, attributed to Boltzmann [122]. According to the Boltzmann superposition principle, the stress-strain relationship can be expressed as [65]:

$$\sigma(t) = \int_{-\infty}^{t} \Upsilon(t-\tau)\frac{\partial\epsilon}{\partial\tau}\,\mathrm{d}\tau, \tag{2.2}$$

where Υ is the relaxation kernel, τ is the relaxation time, and the lower limit of negative infinity indicates that all previous events, including, for example, production processes, should be included in the stress analysis for polymer structures.

With the assumption of harmonic loading, the steady-state stress and strain can be represented as:

$$\begin{aligned} \tilde{\sigma} &= \sigma_0 e^{j\omega t + j\delta(\omega)}, \\ \tilde{\epsilon} &= \epsilon_0 e^{j\omega t}, \end{aligned} \tag{2.3}$$

where σ_0 and ϵ_0 are the stress and strain amplitudes, respectively, ω is the angular frequency, δ is the phase difference between the stress and strain, and j is the imaginary unit. The complex dynamic modulus representation for the steady-state behavior of linear viscoelastic materials [64] follows as:

$$\tilde{E}(\omega) = E'(\omega) + jE''(\omega) = |\tilde{E}(\omega)|e^{j\delta(\omega)}, \tag{2.4}$$

where $\tilde{E}$ is the complex modulus, E' is the storage modulus (associated with elastic behavior), and E'' is the loss modulus (associated with dissipative behavior). The material loss factor, η, is defined as the ratio of the loss modulus to the storage modulus: $\eta = E''/E' = \tan(\delta)$. The complex dynamic modulus is related to the relaxation kernel through the Fourier transform [65]:

$$\tilde{E}(\omega) = j\omega \int_0^\infty \Upsilon(t) e^{-j\omega t} \, \mathrm{d}t. \tag{2.5}$$

Also taking into account the temperature-dependence of the dynamic modulus [65], the steady-state stress-strain relationship is given by:

$$\tilde{\sigma}(t) = \tilde{E}(\omega, T)\tilde{\epsilon}(t), \tag{2.6}$$

where T represents the temperature of the material.

Thermomechanical coupling in polymers is due to both reversible thermoelastic effects and internal energy dissipation. Experiments show that under intensive loading, the dominant mechanism in polymers is internal dissipation [36], generally described by a viscoelastic model. During harmonic loading, the energy losses caused by out-of-phase oscillations between stress and strain generate heat [46]. Due to the poor thermal conductivity of most polymers, this leads to considerable self-heating. That is, the temperature of the polymer rises until a thermal steady state is reached, at which point the heat dispelled to the environment balances that generated from dissipation. Thermal runaway is also possible [37].

2.3 Modeling of a Thin Polymer-based Beam Subjected to Harmonic Excitation

2.3.1 Equation of Motion

The polymeric particulate composite material of interest here is modeled as a homogenized linear viscoelastic material. The utilized x-axis is defined along the beam axis at the centroid of the cross-section, and the y- and z-axes are as shown

in Figure 2.1. The exact geometry of the rectangular beam is also prescribed in the figure. The beam is subjected to harmonic excitation in the transverse, y, direction.

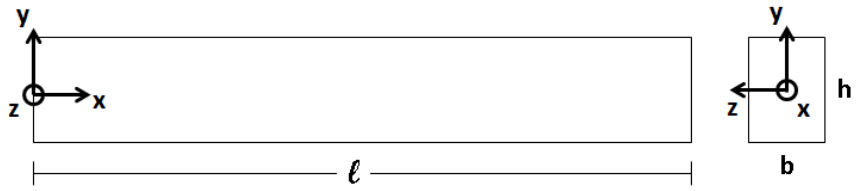

Figure 2.1. An undeformed rectangular beam.

The standard assumptions of Euler-Bernoulli beam theory are used. Namely, effects due to shear deformation and rotary inertia are neglected [123]. The equation for transverse motion is thus given by:

$$\tilde{D}(\omega,T)\frac{\partial^4\tilde{u}}{\partial x^4}+\rho h\frac{\partial^2\tilde{u}}{\partial t^2}=\tilde{f}, \tag{2.7}$$

where, using complex quantities where appropriate, $\tilde{u}$ is the transverse displacement of the neutral surface, ρ is the mass density, $\tilde{f}$ is the forcing function per unit area, and $\tilde{D}$ is the flexural rigidity, which is given by [123]:

$$\tilde{D}(\omega,T)=\frac{\tilde{E}(\omega,T)h^3}{12[1-\nu^2(\omega,T)]}, \tag{2.8}$$

where ν is Poisson's ratio. For beams with a considerable aspect ratio (b/h), the effective stiffness is increased due to the two-dimensional effect in the xz-plane, as in plate-like bending [123, 124]. Accordingly, the flexural rigidity for a thin plate is used, which accounts for the effect of Poisson's ratio on the flexural stiffness.

Considered here is the case for which the ends of the beam, $x = 0$ and $x = \ell$, are subjected to a harmonic acceleration $Ge^{j\omega t}$. The suspended beam is then under inertial excitation with the complex forcing function $\tilde{f}$ set to zero. The transverse displacement is assumed to have the form:

$$\tilde{u}(x,t)=\frac{G}{\omega^2}e^{j\omega t}+\tilde{u}_1(x,t), \tag{2.9}$$

where $\tilde{u}_1$ is the relative deflection of the beam resulting from the base excitation $\frac{G}{\omega^2}e^{j\omega t}$. The equation for transverse motion becomes:

$$\tilde{D}(\omega,T)\frac{\partial^4\tilde{u}_1}{\partial x^4}+\rho h\frac{\partial^2\tilde{u}_1}{\partial t^2}=\rho hGe^{j\omega t}. \tag{2.10}$$

For a beam clamped on both ends, the boundary conditions are given by:

$$\begin{aligned}\tilde{u}_1|_{x=0}&=\frac{\partial\tilde{u}_1}{\partial x}|_{x=0}=0,\\ \tilde{u}_1|_{x=\ell}&=\frac{\partial\tilde{u}_1}{\partial x}|_{x=\ell}=0.\end{aligned} \tag{2.11}$$

Using the normal mode approach [123], the steady-state displacement is then:

$$\tilde{u}_1(x,t)=\sum_{n=1}^{\infty}U_n(x)\frac{\rho hG\int_0^\ell U_n(x)\mathrm{d}x}{\tilde{D}(\omega,T)\zeta_n^4-\rho h\omega^2}e^{j\omega t}, \tag{2.12}$$

where the U_n are the mode shapes that satisfy the boundary conditions provided in Eq. (2.11), which are given by [123]:

$$\begin{aligned}U_n(x)=C_n\big[&\cos(\zeta_n x)-\cosh(\zeta_n x)\\ &-\frac{\cos(\zeta_n\ell)-\cosh(\zeta_n\ell)}{\sin(\zeta_n\ell)-\sinh(\zeta_n\ell)}\left(\sin(\zeta_n x)-\sinh(\zeta_n x)\right)\big];\\ &n=1,2,3,...,\end{aligned} \tag{2.13}$$

and where the constants C_n are given according to the normalization condition:

$$\int_0^\ell U_n^2\,\mathrm{d}x=1. \tag{2.14}$$

The constants ζ_n are the n^{th} positive roots of the corresponding characteristic equation [123]:

$$\cos(\zeta_n\ell)\cosh(\zeta_n\ell)-1=0. \tag{2.15}$$

2.3.2 Heat Transfer Equation

Given that the polymer composite is modeled as a homogenized linear viscoelastic material, thermal isotropy is assumed as well. In addition, the material's thermal

properties are modeled as constant and the effects of thermal expansion are neglected for the small temperature fluctuations considered. Using the Fourier Law of Conduction and considering heat diffusion in all three dimensions, the heat transfer equation is [125]:

$$\frac{\partial^2 T}{\partial x^2} + \frac{\partial^2 T}{\partial y^2} + \frac{\partial^2 T}{\partial z^2} + \frac{1}{\kappa} q = \frac{1}{\chi} \frac{\partial T}{\partial t}, \tag{2.16}$$

where κ is the thermal conductivity, χ is the thermal diffusivity, and q is the volumetric energy generation.

A Green's function approach [126] can be employed to analytically solve the transient heat transfer equation highlighted above. Specifically, the Green's function for a given geometry and set of boundary conditions can be used to construct the temperature solution in conjunction with spatially- and temporally-dependent volumetric energy generation terms. However, even one-dimensional Green's functions typically involve infinite summations, and two- and three-dimensional Green's functions for a rectangular coordinate system use the product of the one-dimensional infinite summations. In addition, spatially-dependent volumetric energy generation is difficult to incorporate analytically in a convenient way, and the aforementioned summations tend to converge slowly [126]. Alternate basis functions, including the beam's mode shapes, have been explored, but convergence issues likewise hamper the utility of these analytical approaches. As such, the volumetric energy generation is computed analytically here and used in conjunction with numerical methods to recover the predicted temperature distributions.

The mechanical energy dissipated in the beam per cycle of harmonic loading can be approximated as the area under the hysteresis loop of the stress-strain plot in the mechanical steady state [65]. Assuming that the temperature varies on a much slower order than the mechanical loading, the volumetric energy generation can be

time-averaged over one mechanical loading cycle [37]. If the energy is dissipated solely as heat, then the time-averaged volumetric energy generation is given by:

$$\begin{aligned} q &= \frac{\omega}{2\pi} \int_{t_0}^{t_0+2\pi/\omega} \sigma \frac{\partial \epsilon}{\partial t} \, \mathrm{d}t \\ &= \frac{E' \eta \omega \epsilon_0^2}{2(1-\nu^2)}, \end{aligned} \tag{2.17}$$

where t_0 is an arbitrary initial time for the steady-state cycle.

In Euler-Bernoulli beam theory, the strain magnitude depends on the transverse position y and on the curvature of the neutral surface [127], according to:

$$\epsilon_0(x, y) = -y\Gamma_0(x), \tag{2.18}$$

where $\Gamma_0(x)$ is the maximum value of the curvature, computed using the second spatial derivative:

$$\begin{aligned} \Gamma_0(x) = \max \left[\frac{\partial^2 \tilde{u}_1(x,t)}{\partial x^2} \right]; \\ t \in [t_0,\, t_0 + 2\pi/\omega]. \end{aligned} \tag{2.19}$$

For a thin beam, the volumetric energy generation can also be spatially-averaged over the thickness [43]. This gives the one-dimensional heat source:

$$q(x) = \frac{E' \eta \omega h^2}{24(1-\nu^2)} \Gamma_0^2(x). \tag{2.20}$$

If a thermal steady state is reached, the heat lost to the environment balances that generated from dissipation, though thermal runaway can occur, for example in materials with sufficiently poor thermal conductivity [37]. In this work, the transient temperature behavior is investigated in two- and three-dimensional numerical simulations using the heat source given in Eq. (2.20).

2.4 Experimental Study of a Particulate Composite Beam

Experiments were conducted using an HTPB beam with embedded NH_4Cl crystals. These ammonium chloride crystals were selected to approximate the particle

sizes of ammonium perchlorate (AP), and, as such, the sample serves as a mechanical mock material for a common propellant or polymer-bonded explosive. The thermal and mechanical responses of the sample were recorded using infrared thermography and scanning laser Doppler vibrometry, as subsequently described.

2.4.1 Sample Preparation

To create the experimental sample, powder-form HTPB was heated to 60 °C and allowed to harden using an isocyanate agent. For mixing with the NH_4Cl crystals, a wetting agent, Tepanol, was applied and a Resodyn acoustic mixer was used to ensure homogeneity. The mixture, designed to be 75% NH_4Cl by volume, was poured into a purpose-built plate mold and cured overnight, and then cut into a beam measuring 25.6 x 2.5 x 1.4 cm. The density of the beam was computed from direct length and mass measurements as 1028.2 kg/m^3. This density is significantly lower than what would be predicted by a linear mix of the densities of pure HTPB and crystalline NH_4Cl, a discrepancy likely attributable to voids in the mixture.

2.4.2 Experimental Setup

A TIRA 59335/LS AIT-440 electrodynamic shaker was used to provide mechanical excitation to the beam, allowing for band-limited white noise or single-frequency harmonic inertial excitation. A VibeLab VL-144 vibration control system was employed to control the system through direct monitoring of an accelerometer mounted on the shaker head. The beam was attached to the shaker using a custom fixture, which was machined to simulate clamped boundaries on both short ends of the beam. The final mounting yielded a 22.9 cm (9 in) unsupported length. The frequency responses and operational deflection shapes of the beam were recorded using a Polytec PSV-400 scanning laser Doppler vibrometer. The test sample and experimental apparatus are shown in Figure 2.2.

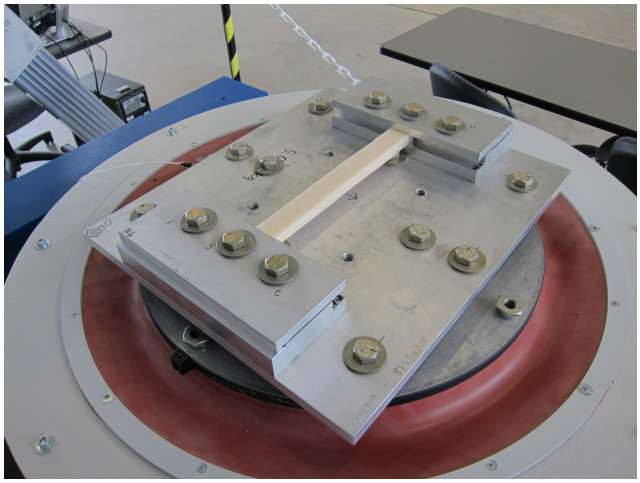

Figure 2.2. The experimental sample, an HTPB beam with embedded NH_4Cl crystals, mounted on a TIRA 59335/LS AIT-440 electrodynamic shaker.

For the purposes of mechanical analysis, broadband (10–1000 Hz) white noise excitation was applied at three forcing levels (1, 1.86, and 2.44 g RMS). The system response was estimated using the classical H1 estimator, which compares the measured cross-spectral density of the accelerometer and vibrometer readings to the measured power spectral density of the accelerometer. The H1 frequency response estimators were calculated at two distinct points, the geometric center of the top face of the beam and an offset point on the top face, for all three forcing levels. The offset point was located one quarter of the distance along the beam, on the centerline.

The transient and steady-state thermal responses of the top face were recorded using a FLIR A325 thermal camera, which has a temperature sensitivity of 0.07 °C at 30 °C and an accuracy of ±2 °C or ±2%. The infrared data was calibrated to the emissivity of the beam using a thermocouple at ambient conditions. For thermal testing, the beam was excited near first resonance for 60 min and was seen to approach thermal steady state within this time. Though no attempt was made to control the ambient temperature or flow conditions, neither was observed to change significantly for the duration of the experiment.

2.5 Numerical Simulation

To solve the heat transfer equation highlighted above, numerical methods were employed. First, an in-house Wolfram Mathematica® code was utilized to compute the mechanical response of the beam and numerically solve the two-dimensional problem of heat diffusion in the xz-plane using the heat source given in Eq. (2.20). For the mechanical portion of the simulation, the density value was specified as 1028.2 kg/m^3, as obtained from direct measurement. The Poisson's ratio was estimated as 0.39, based on perceived similarities to more common materials. The storage modulus was estimated from the resonant response of a cylindrical sample of the same HTPB composite as 83.57 MPa [128]. The material loss factor was estimated as 0.35 by using the half-power bandwidth method [129] on data taken from experimental frequency responses.

To solve the heat equation, the thermal conductivity and thermal diffusivity were measured using the transient plane source technique [130] as 0.52 W/(m-K) and 3.13×10^{-7} m^2/s, respectively. For the two-dimensional Mathematica® solution, a stiffness switching method was employed. A convective heat sink was applied to the two-dimensional surface, using a convection coefficient of 5 W/(m^2-K) in an attempt to match the transient behavior observed experimentally. This value is comparable with coefficients found in experimental investigations [131–133] and is within the range for free convection estimates presented in [125]. Insulated boundary conditions were applied on all edges. An additional three-dimensional finite element simulation, implemented in COMSOL Multiphysics®, was employed as a further point of comparison. In this simulation, the same heat source was applied to a 259-node three-dimensional mesh with insulated boundary conditions on the ends and convective conditions elsewhere. Both methods were used to generate simulations of transient behavior over 60 min, as well as top-down thermal profiles, which allow for direct comparison to the experimentally-obtained thermal images.

2.6 Results and Discussion

2.6.1 Mechanical Response

The H1 frequency response estimators for the beam in response to the three levels of band-limited white noise excitation are presented as Figure 2.3. Data at both the center and offset points on the top face are presented. The beam exhibits multiple clear resonant peaks, which decrease slightly in relative amplitude and frequency as the forcing level increases.

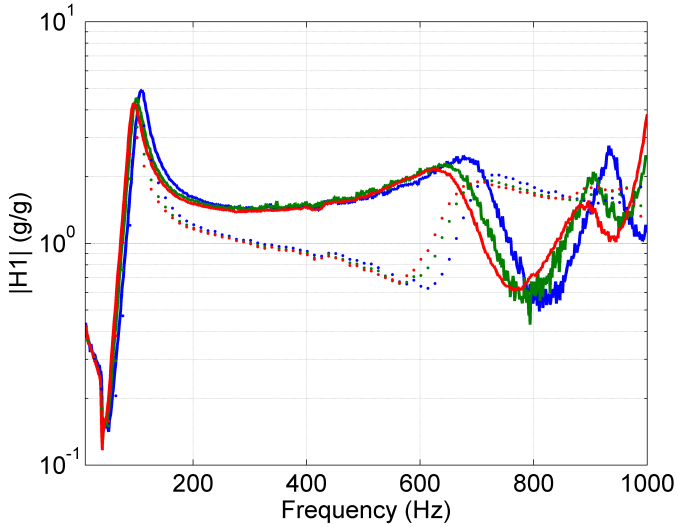

Figure 2.3. The experimental H1 mechanical frequency response estimators for three levels of excitation. The blue, green, and red curves represent responses at 1, 1.86, and 2.44 g RMS, respectively. Solid lines correspond to data from the center point and dashed lines correspond to data from the offset point.

The beam was then excited with harmonic forcing at the first resonant frequency, which was estimated from the H1 frequency response estimators for each of the respective forcing levels. A representative operational deflection shape recorded at 2g harmonic forcing is presented with the theoretically-recovered magnitude of steady-state displacement in Figure 2.4. As is evident from the figure, the system model approximates the behavior of the particulate composite to an acceptable degree. The

magnitudes of the experimentally-recorded displacements show good agreement with the theoretical predictions. For example, in the representative operational deflection shape shown in Figure 2.4, there is a 4.5% error in the measured response compared to the theoretical prediction at the center of the beam. Due to the imperfect nature of the clamping fixture, there are notable deviations at the ends, resulting in higher local predicted stresses as compared to the stresses encountered in the experiment. These deviations may also be attributable to the fact that the scanning laser Doppler vibrometer had difficulty in measuring the response near the clamping fixture.

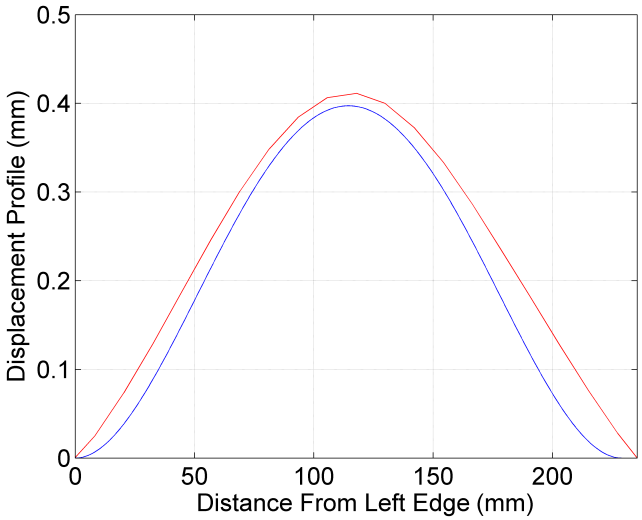

Figure 2.4. A representative operational deflection shape recorded at 2g harmonic forcing near the beam's first natural frequency (red curve) plotted with the theoretical magnitude of the steady-state displacement (blue curve).

2.6.2 Thermal Response

With the beam excited with 1g, 2g, and 3g harmonic forcing near the first natural frequency, the transient thermal response of the top surface was recorded. The recorded maximum and mean transient surface temperatures are presented as Figure 2.5. Due to the intrinsic noise in infrared temperature measurement, the data points

presented represent the average of five temporally-adjacent thermal measurements. For each of the forcing levels, the temperatures asymptotically approach steady-state values in the 60 min of recording time. In general, greater forcing levels lead to greater heating, and the maximum recorded surface temperatures increase with forcing level. The highest mean surface temperatures are for 3g forcing, though the recorded mean temperatures for 1g and 2g forcing are comparable. In addition, the largest separation between the maximum and mean temperatures was recorded for the 3g forcing.

The surface temperature distributions recorded after 60 min are presented in Figure 2.6. Maximal heating was recorded near the center of the surface for all forcing levels. The axial variation of temperature is observed to coincide with the stress and strain fields expected with a linear viscoelastic material. As noted in Eq. (2.17), the volumetric heat generation is proportional to the square of the strain magnitude. This effect is especially prominent with the 2g and 3g forcing levels, where higher local temperatures are observed in areas of high local stress near the ends of the beam. Variations in temperature through the width of the beam are attributable to the convective boundaries on each surface. Specifically, heat is dispelled to the environment at the surfaces and greater temperatures are generated at the center, farthest away from those surfaces. The effects of the stress field and convective boundaries interact in the surface temperature distributions recorded. The lesser prominence of structure for the 1g forcing level is due to the comparatively-lower temperature deviations recovered.

The numerical simulation results for the maximum and mean transient surface temperatures at all three forcing levels are presented in Figures 2.7 and 2.8 for the two- and three-dimensional simulations, respectively. Likewise, the steady-state surface temperature distributions recovered from the simulations for 3g harmonic excitation are presented in Figures 2.9 and 2.10, again for the two- and three-dimensional simulations, respectively. The steady-state surface temperatures computed for 3g harmonic excitation were also averaged over the width of the beam and the profiles are presented as a function of axial position in Figure 2.11. The experimental tempera-

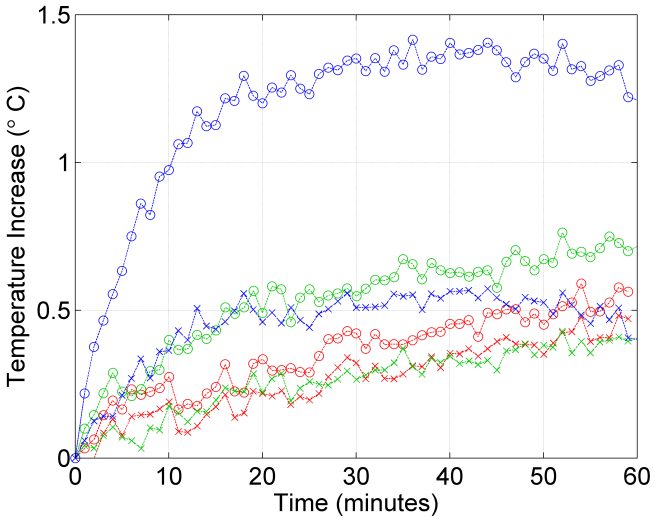

Figure 2.5. The experimental maximum and mean transient surface temperatures obtained with harmonic forcing near the first natural frequency. The red, green, and blue data points represent responses to forcing at 1g, 2g, and 3g, respectively. Circles correspond to maximum surface temperatures and ×'s correspond to mean surface temperatures.

ture recorded after 60 min at 3g harmonic forcing, likewise averaged over the width of the beam, is also shown in Figure 2.11. The temperature magnitudes recovered from the three-dimensional simulation show reasonable agreement with the recorded distributions. Temperatures in the two-dimensional simulation are seen to approach the thermal steady state more slowly than do the temperatures in the three-dimensional simulation. This is attributable to the fact that, since heat is only allowed to diffuse in two dimensions in the former case, internal diffusion and rejection of heat to the environment is less effective. This also accounts for the greater temperatures obtained in the two-dimensional simulation. The steady-state surface temperature distribution computed in the three-dimensional simulation shows a character consistent with the distribution recorded at 3g forcing. A local region of higher temperatures is generated near the center and the effect of the convective boundaries is apparent at the edges. The simulation also captures the higher relative temperatures at the ends of

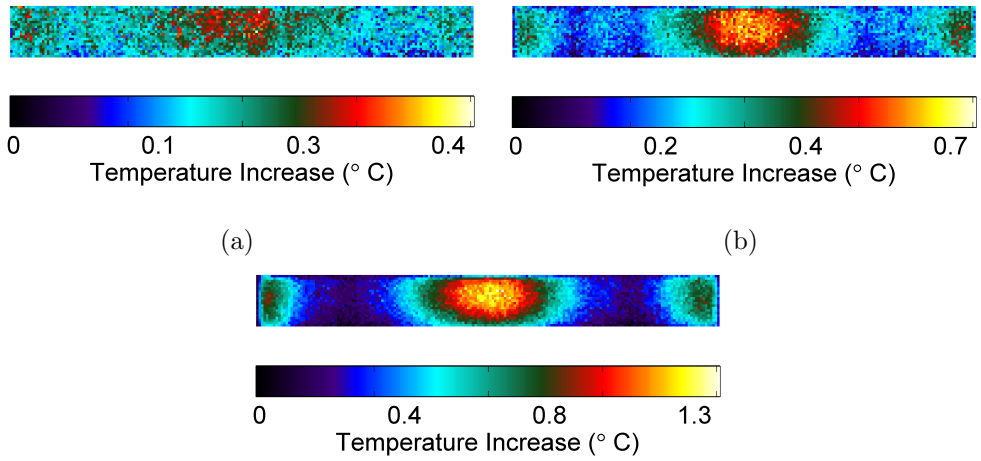

Figure 2.6. The experimental surface temperature distribution recorded after 60 min in response to harmonic forcing at (a) 1g, (b) 2g, and (c) 3g. Forcing was near the first natural frequency for each case.

the beam, but the observed effect is magnified as compared to experiments. As previously noted, this is likely due to the imperfect nature of the clamping fixture, which leads to higher predicted stresses near the ends of the beam when they are modeled as clamped boundaries.

2.7 Conclusions

In this chapter, a thermomechanical model of a polymeric particulate composite beam has been presented, wherein the composite is modeled as a homogenized linear viscoelastic material. The composition under consideration, which consists of an HTPB binder with embedded NH_4Cl crystals, is intended to resemble common polymer-bonded energetic materials. Despite the material composition as a particulate composite, classical Euler-Bernoulli beam theory, along with the complex modulus model for viscoelastic materials, yielded predictions of the thermal and mechanical responses consistent with experimental measurements. The acquired results revealed

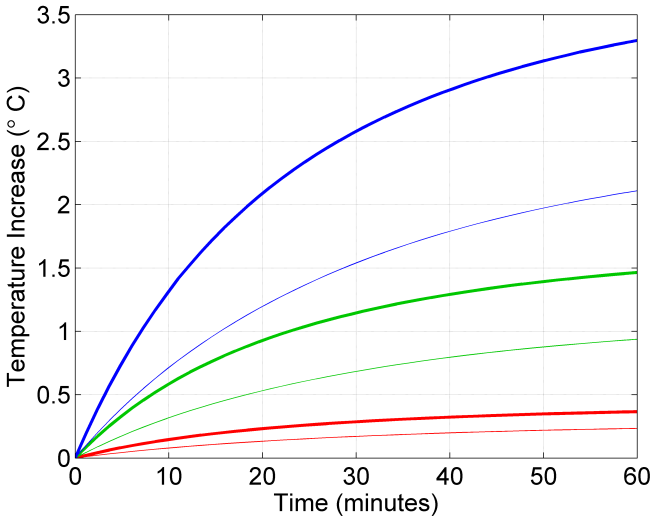

Figure 2.7. The maximum and mean transient surface temperatures obtained in the two-dimensional numerical simulation with harmonic forcing near the first natural frequency. The red, green, and blue curves represent responses to forcing at 1g, 2g, and 3g, respectively. Bold lines correspond to maximum surface temperatures and thin lines correspond to mean surface temperatures.

a strong dependence of the thermal response on the stress and strain fields produced within the beam. In addition to modal structure, convection at the surfaces was shown to impact the thermal response, and temperature excursions were noted near the center of the beam geometry.

As previously highlighted, since explosive vapor pressures exhibit a strong dependence on temperature, the capabilities of vapor-based detection systems may be enhanced significantly by heating. Heat generation in response to harmonic excitation increases, as noted in Section 2.3.2, with strain magnitude and, for a given strain level, with forcing frequency. The strain magnitude may be increased with greater forcing levels or selective boundary conditions, though obviously there is limited control over boundary conditions in many explosives detection systems. Heat generation is also intensified as the phase difference between stress and strain oscillations, quantified by the material loss factor, is increased. The phase difference depends on the

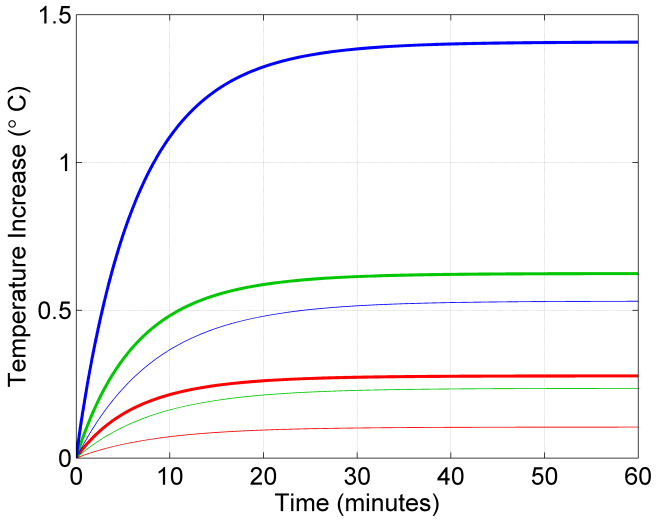

Figure 2.8. The maximum and mean transient surface temperatures obtained in the three-dimensional numerical simulation with harmonic forcing near the first natural frequency. The red, green, and blue curves represent responses to forcing at 1g, 2g, and 3g, respectively. Bold lines correspond to maximum surface temperatures and thin lines correspond to mean surface temperatures.

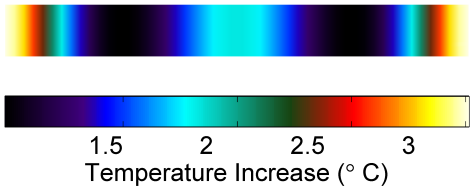

Figure 2.9. The steady-state surface temperature distribution obtained in the two-dimensional numerical simulation in response to 3g harmonic forcing near the first natural frequency.

forcing level and frequency [64], and thus may be used to enhance heating. Though heating also depends on other moduli, there is little control over material properties and sample geometry in explosives detection applications.

In addition to the structural heating considered in this chapter, microscale heating of energetic materials through laser-based or ultrasonic excitation [44, 134, 135] may also constitute a viable pathway to improved trace vapor detection capabilities.

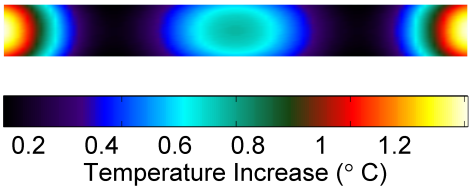

Figure 2.10. The steady-state surface temperature distribution obtained in the three-dimensional numerical simulation in response to 3g harmonic forcing near the first natural frequency.

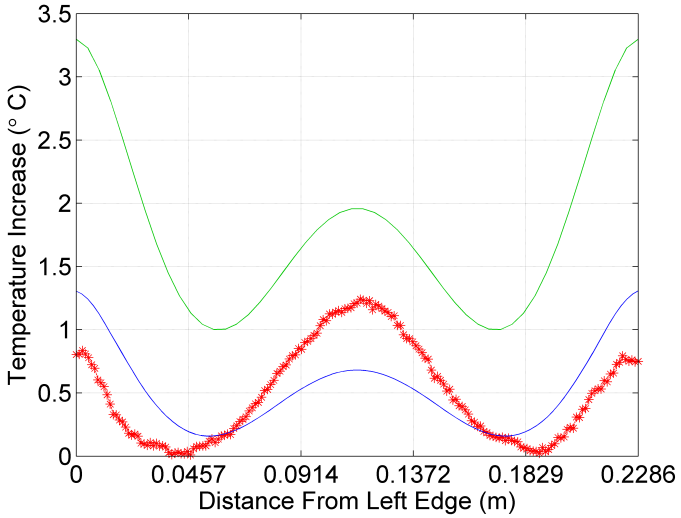

Figure 2.11. The experimental surface temperature distribution recorded after 60 min and the steady-state surface temperature distributions obtained in numerical simulations in response to 3g harmonic forcing near the first natural frequency. The red data points correspond to the experimental temperatures, and the green and blue curves correspond to the two- and three-dimensional numerical simulations, respectively. The temperatures are averaged over the beam width at the surface and presented as a function of axial position.

Targeting local hot spots in the composite structure can result in greater thermal responses, but doing so generally requires proximal access to the material's surface. In contrast, low-frequency acoustical excitations can be transmitted over large distances, and thus may be useful for standoff heating. Localized heating near a single energetic crystal under ultrasonic excitation is the subject of Chapter 3, and the waveforms

which optimize the energy transmission through acoustical or ultrasonic excitation are considered in Chapters 4, 5, and 6.

3. VISCOELASTIC HEATING OF A SPHERICAL PARTICLE EMBEDDED IN A POLYMER-BASED BINDER MATERIAL SUBJECTED TO PLANE WAVE EXCITATION

3.1 Introduction

Polymer-bonded energetic materials generally consist of a polymer-based binder material with embedded energetic crystals. When elastic waves propagate in the composite system, the scattering at the crystals may yield significant stress concentrations, which in turn may result in relatively high levels of localized heating that contribute to the formation of hot spots near the crystals. The purpose of this chapter is to investigate an idealized case specified as a single energetic crystal embedded in a viscoelastic binder medium under plane wave excitation, in order to assess the magnitude of the predicted viscoelastic heating of the binder material. An analytical solution for the stress field, available in the literature, is employed and the energetic crystal is treated as a rigid particle. The viscoelastic heating model presented in Chapter 2 is extended to general three-dimensional stress-strain states through the use of the generalized Hooke's law for linear viscoelastic media. The model for the heat generation field is then used with a numerical solution scheme to solve the Fourier Law of Conduction to predict the temperature evolution and distribution in the system. It should be noted that the generation of large temperature gradients near energetic crystals is generally modeled by assuming defects or voids near the crystal [59–62], which result in stress concentrations. The model results investigated here, however, predict significant heating near the crystal due to the viscoelastic heating of the binder alone, even if perfect bonding is maintained at the crystal–binder interface.

In relation to Chapter 2, this chapter serves to not only extend the viscoelastic heating model to three-dimensional stress-strain states, but also to examine the scale of the heating at individual energetic crystals, in contrast with the bulk-scale heating along modal structures. Though the configuration investigated here represents an idealized case, considering a single energetic crystal, the analytical model which is developed provides a physics-based approach to the prediction of initial viscoelastic heating rates near crystals under harmonic excitation, particularly with regard to informing the generation of localized hot spots in energetic systems, which may be extended in higher-fidelity simulations. Major portions of this chapter first appeared in the Proceedings of the ASME 2016 International Mechanical Engineering Congress & Exposition [136], and a manuscript on the work was subsequently submitted to the Journal of Applied Mechanics [137]. This work was completed in conjunction with Jesus O. Mares and Caroline E. Baker.

3.2 Stresses Induced in a Viscoelastic Medium with a Rigid Spherical Inclusion Subjected to Longitudinal Plane Wave Excitation

The analytical solution for the stress fields in an infinite elastic medium with a spherical inclusion subjected to harmonic longitudinal plane wave excitation has been presented for numerous cases [138–147]. The case under consideration in this work is that of a movable rigid sphere in an infinite, homogeneous, isotropic, linear viscoelastic medium. For the sake of brevity, only the equations for the wave potentials and the solutions for the stress fields and particle displacement will be given here. Detailed derivations can be found in the works of Pao and Mow [139] and Sessarego et al. [146]. Since only the steady-state response is considered, those derivations for a lossless elastic medium can be easily extended to a linear viscoelastic medium by replacing the real elastic parameters with the corresponding complex material parameters [143, 145], which accounts for the viscoelastic losses at the specified excitation frequency.

The utilized rectangular and spherical coordinate systems are shown in Figure 3.1. The surrounding viscoelastic medium, or binder, is characterized by density ρ_1, complex longitudinal wavenumber $\tilde{k}_{1L}$, and complex shear wavenumber $\tilde{k}_{1S}$. The first and second Lamé parameters, $\tilde{\lambda}_1$ and $\tilde{\mu}_1$, as well as all other material moduli, can be subsequently calculated from the relations for linear viscoelastic media [66]: $\tilde{\lambda}_1 = \rho_1\omega^2(1/\tilde{k}_{1L}^2 - 2/\tilde{k}_{1S}^2)$ and $\tilde{\mu}_1 = \rho_1\omega^2/\tilde{k}_{1S}^2$, where ω is the angular excitation frequency. The spherical particle, since it is modeled as rigid, is characterized mechanically only by the density ρ_2 and particle radius a. The incident longitudinal plane wave, as shown in Figure 3.1, travels in the positive z-direction in the surrounding medium and is characterized by its longitudinal wave potential:

$$\tilde{\Phi}_{inc} = \tilde{\Phi}_0 e^{j(\tilde{k}_{1L}z - \omega t)}, \tag{3.1}$$

where t is the time variable and $\tilde{\Phi}_0$ is the incident wave potential amplitude at $z = 0$. Since there is no transverse incident wave, the incident shear wave potential is zero.

The stresses in the viscoelastic binder medium are recovered through the application of the boundary conditions at the particle–binder interface, $r = a$, which require continuity of the displacement component normal to the interface $\tilde{u}_r$ (i.e., the radial component), the displacement component in the in-plane rotational direction $\tilde{u}_\theta$, the stress normal to the interface $\tilde{\sigma}_{rr}$, and the in-plane shear stress $\tilde{\sigma}_{r\theta}$ [139, 146]. It should be noted that, due to the symmetry about the z-axis, there is no displacement in the ϕ-direction, and the shear stresses $\tilde{\sigma}_{r\phi}$ and $\tilde{\sigma}_{\theta\phi}$ are likewise zero.

In order to apply these conditions, the incident wave potential can be expressed in spherical coordinates as a summation [139]:

$$\tilde{\Phi}_{inc} = \tilde{\Phi}_0 e^{-j\omega t} \sum_{n=0}^{\infty} (2n+1) j^n P_n(\cos\theta) J_n(\tilde{k}_{1L} r), \tag{3.2}$$

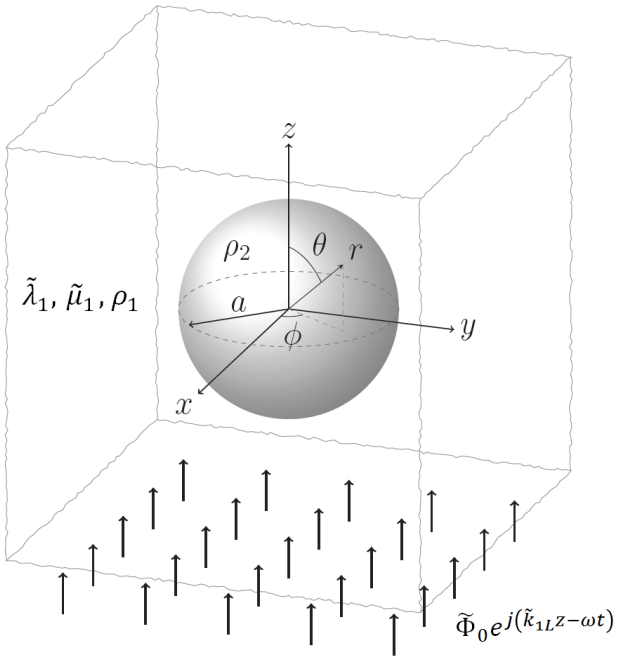

Figure 3.1. A diagram of the rectangular and spherical coordinate systems at a rigid spherical particle of radius a in an infinite linear viscoelastic medium. An incident harmonic longitudinal plane wave travels in the positive z-direction in the viscoelastic medium.

where the P_n are the Legendre polynomials and the J_n are the spherical Bessel functions of the first kind. Similarly, the wave potentials for the scattered longitudinal and shear waves in the viscoelastic medium can be written, respectively, as:

$$\begin{aligned} \tilde{\Phi}_{sctd} &= e^{-j\omega t} \sum_{n=0}^{\infty} \tilde{\mathcal{A}}_n P_n(\cos\theta) H_n(\tilde{k}_{1L} r), \\ \tilde{\Psi}_{sctd} &= e^{-j\omega t} \sum_{n=0}^{\infty} \tilde{\mathcal{B}}_n P_n(\cos\theta) H_n(\tilde{k}_{1S} r), \end{aligned} \tag{3.3}$$

where the H_n are the spherical Hankel functions of the first kind, and the $\tilde{\mathcal{A}}_n$ and $\tilde{\mathcal{B}}_n$ are the coefficients which are determined by the boundary conditions. The reader is referred to the work of Pao and Mow [139] for the expressions for the coefficients $\tilde{\mathcal{A}}_n$ and $\tilde{\mathcal{B}}_n$ (written in [139] as unscripted and without the tilde accents, A_n and B_n), as given for the case of a movable rigid inclusion. The refracted wave potentials do not need to be taken into account since the particle is modeled as rigid. Moreover, since no deformations are developed within a rigid particle, all of the strain components are identically zero in the region $r < a$, and the particle simply undergoes rigid body motion along the direction of the incident wave.

The solution for the stresses in the binder material (i.e., in the region $r \geq a$), which allows for the translational motion of the spherical inclusion, follows from the wave potentials and can be explicitly expressed, in spherical coordinates, as [139, 146]:

$$
\begin{aligned}
\tilde{\sigma}_{1,rr} &= \frac{2\tilde{\mu}_1}{r^2} e^{-j\omega t} \sum_{n=0}^{\infty} P_n(\cos\theta) \Big\{ \\
&\quad \tilde{\Phi}_0 j^n (2n+1) \Big[(n^2 - n - \tilde{k}_{1S}^2 r^2/2) J_n(\tilde{k}_{1L} r) + 2\tilde{k}_{1L} r J_{n+1}(\tilde{k}_{1L} r) \Big] \\
&\quad + \tilde{\mathcal{A}}_n \Big[(n^2 - n - \tilde{k}_{1S}^2 r^2/2) H_n(\tilde{k}_{1L} r) + 2\tilde{k}_{1L} r H_{n+1}(\tilde{k}_{1L} r) \Big] \\
&\quad - \tilde{\mathcal{B}}_n \Big[n(n+1)(n-1) H_n(\tilde{k}_{1S} r) - n(n+1) \tilde{k}_{1S} r H_{n+1}(\tilde{k}_{1S} r) \Big] \Big\}, \\
\tilde{\sigma}_{1,r\theta} &= \frac{2\tilde{\mu}_1}{r^2} e^{-j\omega t} \sum_{n=0}^{\infty} \frac{\mathrm{d}P_n(\cos\theta)}{\mathrm{d}\theta} \Big\{ \\
&\quad \tilde{\Phi}_0 j^n (2n+1) \Big[(n-1) J_n(\tilde{k}_{1L} r) - \tilde{k}_{1L} r J_{n+1}(\tilde{k}_{1L} r) \Big] \\
&\quad + \tilde{\mathcal{A}}_n \Big[(n-1) H_n(\tilde{k}_{1L} r) - \tilde{k}_{1L} r H_{n+1}(\tilde{k}_{1L} r) \Big] \\
&\quad - \tilde{\mathcal{B}}_n \Big[(n^2 - 1 - \tilde{k}_{1S}^2 r^2/2) H_n(\tilde{k}_{1S} r) + \tilde{k}_{1S} r H_{n+1}(\tilde{k}_{1S} r) \Big] \Big\}, \\
\tilde{\sigma}_{1,\theta\theta} &= \frac{2\tilde{\mu}_1}{r^2} e^{-j\omega t} \sum_{n=0}^{\infty} \Bigg(P_n(\cos\theta) \Big\{ \\
&\quad \tilde{\Phi}_0 j^n (2n+1) \Big[(n + \tilde{k}_{1L}^2 r^2 - \tilde{k}_{1S}^2 r^2/2) J_n(\tilde{k}_{1L} r) - \tilde{k}_{1L} r J_{n+1}(\tilde{k}_{1L} r) \Big] \\
&\quad + \tilde{\mathcal{A}}_n \Big[(n + \tilde{k}_{1L}^2 r^2 - \tilde{k}_{1S}^2 r^2/2) H_n(\tilde{k}_{1L} r) - \tilde{k}_{1L} r H_{n+1}(\tilde{k}_{1L} r) \Big] \\
&\quad - \tilde{\mathcal{B}}_n n(n+1) H_n(\tilde{k}_{1S} r) \Big\} \\
&\quad + \frac{\mathrm{d}^2 P_n(\cos\theta)}{\mathrm{d}\theta^2} \Big\{ \tilde{\Phi}_0 j^n (2n+1) J_n(\tilde{k}_{1L} r) + \tilde{\mathcal{A}}_n H_n(\tilde{k}_{1L} r) \\
&\quad - \tilde{\mathcal{B}}_n \Big[(n+1) H_n(\tilde{k}_{1S} r) - \tilde{k}_{1S} r H_{n+1}(\tilde{k}_{1S} r) \Big] \Big\} \Bigg), \\
\tilde{\sigma}_{1,\phi\phi} &= \frac{2\tilde{\mu}_1}{r^2} e^{-j\omega t} \sum_{n=0}^{\infty} \Bigg(P_n(\cos\theta) \Big\{ \\
&\quad \tilde{\Phi}_0 j^n (2n+1) \Big[(n + \tilde{k}_{1L}^2 r^2 - \tilde{k}_{1S}^2 r^2/2) J_n(\tilde{k}_{1L} r) - \tilde{k}_{1L} r J_{n+1}(\tilde{k}_{1L} r) \Big] \\
&\quad + \tilde{\mathcal{A}}_n \Big[(n + \tilde{k}_{1L}^2 r^2 - \tilde{k}_{1S}^2 r^2/2) H_n(\tilde{k}_{1L} r) - \tilde{k}_{1L} r H_{n+1}(\tilde{k}_{1L} r) \Big] \\
&\quad - \tilde{\mathcal{B}}_n n(n+1) H_n(\tilde{k}_{1S} r) \Big\} \\
&\quad + \cot\theta \frac{\mathrm{d}P_n(\cos\theta)}{\mathrm{d}\theta} \Big\{ \tilde{\Phi}_0 j^n (2n+1) J_n(\tilde{k}_{1L} r) + \tilde{\mathcal{A}}_n H_n(\tilde{k}_{1L} r) \\
&\quad - \tilde{\mathcal{B}}_n \Big[(n+1) H_n(\tilde{k}_{1S} r) - \tilde{k}_{1S} r H_{n+1}(\tilde{k}_{1S} r) \Big] \Big\} \Bigg).
\end{aligned}
\tag{3.4}
$$

Finally, the displacement of the rigid particle in the z-direction can then be written as [139]:

$$\tilde{u}_{2,z} = \frac{\rho_1}{\rho_2 a}\left[3j\tilde{\Phi}_0 J_1(\tilde{k}_{1L}a) + \tilde{\mathcal{A}}_1 H_1(\tilde{k}_{1L}a) - 2\tilde{\mathcal{B}}_1 H_1(\tilde{k}_{1S}a)\right] e^{-j\omega t}. \tag{3.5}$$

It should be noted here that, though the binder medium was assumed to be infinite for the purpose of developing the analytical stress solution, for the solution of the thermal response in Section 3.3.2, the binder will be treated as a large sphere, concentric with the particle, with a convective surface condition applied at the outer radius r_{outer}. This outer radius at which the thermal boundary condition is applied must be large in comparison with the incident wavelength and particle radius, so that the computation of the stresses in an infinite medium remains a valid approximation.

3.3 Viscoelastic Heating of the Surrounding Medium

3.3.1 Volumetric Heat Generation

The mechanical energy dissipated in a viscoelastic medium per unit volume can be approximated by the losses in the strain energy density over each harmonic loading cycle [37, 65, 148–151]. Under the assumption that the temperature variation is on a much slower time scale than the mechanical loading, this energy dissipated per cycle can be time-averaged to give the rate of energy dissipation. If it is further assumed that the mechanical energy is dissipated entirely as heat, then this rate is equal to the volumetric heat generation:

$$\begin{aligned} q = \frac{\omega}{2\pi}\int_{t_0}^{t_0+2\pi/\omega} \Big(&\sigma_{rr}\frac{\partial \epsilon_{rr}}{\partial t} + \sigma_{\theta\theta}\frac{\partial \epsilon_{\theta\theta}}{\partial t} + \sigma_{\phi\phi}\frac{\partial \epsilon_{\phi\phi}}{\partial t} \\ &+ 2\sigma_{r\theta}\frac{\partial \epsilon_{r\theta}}{\partial t} + 2\sigma_{r\phi}\frac{\partial \epsilon_{r\phi}}{\partial t} + 2\sigma_{\theta\phi}\frac{\partial \epsilon_{\theta\phi}}{\partial t}\Big)\,\mathrm{d}t, \end{aligned} \tag{3.6}$$

where the ϵ_{ln} are the strain components and t_0 is the initial time for the specified cycle. Note that the real parts of the stress and strain components are used in the integral computation, as the phase lags introduced by the material losses yield the net mechanical energy losses.

By using the linear viscoelastic model employed in Section 3.2, the heat generation in the binder material can be written explicitly in terms of the complex material moduli [66]. The generalized Hooke's law for isotropic media can be applied to relate the strain components to the nonzero stress components, which yields the strain magnitudes and relative phase lags. The volumetric heat generation in the binder medium for this particular loading case is then the sum of four nonzero contributions to the net change in strain energy density:

$$q_1 = \frac{\omega}{2|\tilde{E}_1|}\left(\xi_{1,rr} + \xi_{1,\theta\theta} + \xi_{1,\phi\phi} + 2\xi_{1,r\theta}\right), \tag{3.7}$$

where $\tilde{E}_1$ is the complex Young's modulus of the binder and the scaled contributions $\xi_{1,ln}$ are given by:

$$\begin{aligned}
\xi_{1,rr} &= \sin(\delta_{1,rr})\,|\tilde{\sigma}_{1,rr}|\,|\tilde{\sigma}_{1,rr} - \tilde{\nu}_1\,(\tilde{\sigma}_{1,\theta\theta} + \tilde{\sigma}_{1,\phi\phi})|\,, \\
\xi_{1,\theta\theta} &= \sin(\delta_{1,\theta\theta})\,|\tilde{\sigma}_{1,\theta\theta}|\,|\tilde{\sigma}_{1,\theta\theta} - \tilde{\nu}_1\,(\tilde{\sigma}_{1,rr} + \tilde{\sigma}_{1,\phi\phi})|\,, \\
\xi_{1,\phi\phi} &= \sin(\delta_{1,\phi\phi})\,|\tilde{\sigma}_{1,\phi\phi}|\,|\tilde{\sigma}_{1,\phi\phi} - \tilde{\nu}_1\,(\tilde{\sigma}_{1,rr} + \tilde{\sigma}_{1,\theta\theta})|\,, \\
\xi_{1,r\theta} &= \sin(\delta_{1,r\theta})\,|1 + \tilde{\nu}_1|\,|\tilde{\sigma}_{1,r\theta}|^2\,,
\end{aligned} \tag{3.8}$$

where $\tilde{\nu}_1$ is the corresponding complex Poisson's ratio and the $\delta_{1,ln}$ are the phase differences between the respective stress and strain components:

$$\begin{aligned}
\delta_{1,rr} &= \angle\tilde{E}_1 + \angle\tilde{\sigma}_{1,rr} - \angle[\tilde{\sigma}_{1,rr} - \tilde{\nu}_1\,(\tilde{\sigma}_{1,\theta\theta} + \tilde{\sigma}_{1,\phi\phi})], \\
\delta_{1,\theta\theta} &= \angle\tilde{E}_1 + \angle\tilde{\sigma}_{1,\theta\theta} - \angle[\tilde{\sigma}_{1,\theta\theta} - \tilde{\nu}_1\,(\tilde{\sigma}_{1,rr} + \tilde{\sigma}_{1,\phi\phi})], \\
\delta_{1,\phi\phi} &= \angle\tilde{E}_1 + \angle\tilde{\sigma}_{1,\phi\phi} - \angle[\tilde{\sigma}_{1,\phi\phi} - \tilde{\nu}_1\,(\tilde{\sigma}_{1,rr} + \tilde{\sigma}_{1,\theta\theta})], \\
\delta_{1,r\theta} &= \angle\tilde{E}_1 - \angle[1 + \tilde{\nu}_1].
\end{aligned} \tag{3.9}$$

The symbol $\angle$ denotes the phase of the argument. The complex Young's modulus is related to the Lamé parameters by $\tilde{E}_1 = \tilde{\mu}_1(3\tilde{\lambda}_1 + 2\tilde{\mu}_1)/(\tilde{\lambda}_1 + \tilde{\mu}_1)$, and the complex Poisson's ratio by $\tilde{\nu}_1 = \tilde{\lambda}_1/[2(\tilde{\lambda}_1 + \tilde{\mu}_1)]$ [66]. It should be noted that the stress components at any given point are, in general, not in phase with one another, which is taken into account in Eqs. (3.8) and (3.9).

The heat generation term specified by the relations in Eqs. (3.7), (3.8), and (3.9) represents the extension of loss predictions based on the hysteresis loop for one-

dimensional stress-strain states [65] (as was discussed in Chapter 2) to the three-dimensional state under consideration here. Direct application of the relations, along with the nonzero stress components, yields the volumetric heat generation induced in the binder material. Since the particle is treated as rigid, there is no viscoelastic heat generation in the spherical inclusion (i.e., $q_2 = 0$). Thus, the only bulk heating in the system due to material dissipation is the viscoelastic heating of the binder.

It should also be emphasized here that this three-dimensional heat generation model applies broadly to linear viscoelastic materials subjected to general three dimensional stress-strain states, assuming steady-state harmonic deformations. The model requires only the material properties and the stress state as specified in an orthogonal coordinate system. For a generic orthogonal system, with the axes denoted by x_1, x_2, and x_3, and in a given linear viscoelastic medium, the volumetric heat generation is then:

$$q = \frac{\omega}{2|\tilde{E}|}\left(\xi_{x_1x_1} + \xi_{x_2x_2} + \xi_{x_3x_3} + 2\xi_{x_1x_2} + 2\xi_{x_1x_3} + 2\xi_{x_2x_3}\right). \tag{3.10}$$

For the normal stress components, the scaled contributions ξ_{ln} to the heat generation take the form:

$$\xi_{x_1x_1} = \sin(\delta_{x_1x_1})\,|\tilde{\sigma}_{x_1x_1}|\,|\tilde{\sigma}_{x_1x_1} - \tilde{\nu}\,(\tilde{\sigma}_{x_2x_2} + \tilde{\sigma}_{x_3x_3})|\,, \tag{3.11}$$

where the phase difference $\delta_{x_1x_1}$ is:

$$\delta_{x_1x_1} = \angle\tilde{E} + \angle\tilde{\sigma}_{x_1x_1} - \angle[\tilde{\sigma}_{x_1x_1} - \tilde{\nu}\,(\tilde{\sigma}_{x_2x_2} + \tilde{\sigma}_{x_3x_3})]. \tag{3.12}$$

Equations analogous to Eqs. (3.11) and (3.12) can be written for $\xi_{x_2x_2}$ and $\xi_{x_3x_3}$. For the shear stress components, the scaled contributions have the form:

$$\xi_{x_1x_2} = \sin(\delta_{x_1x_2})\,|1 + \tilde{\nu}|\,|\tilde{\sigma}_{x_1x_2}|^2\,, \tag{3.13}$$

for which the phase difference is:

$$\delta_{x_1x_2} = \angle\tilde{E} - \angle[1 + \tilde{\nu}]. \tag{3.14}$$

Equations analogous to Eqs. (3.13) and (3.14) can similarly be written for $\xi_{x_1x_3}$ and $\xi_{x_2x_3}$.

3.3.2 Heat Transfer Equation

The temperature distribution and evolution in the system are modeled in this work by application of the Fourier Law of Conduction and are solved by using a finite difference approach. Thermal isotropy is assumed in both the binder and the particle. The strains due to thermal expansion and the corresponding losses due to thermoelastic damping [152–155] are neglected in the temperature predictions. This approximation is valid only in the limit of small temperature increases, or, equivalently, over a time interval sufficiently small such that only small temperature rises occur, with the result that the thermal strains are negligible in comparison to those from the applied mechanical excitation. The residual thermal stresses at the particle–binder interface, which develop due to the mismatch of the thermal expansion coefficients and would introduce a nonzero offset into the harmonic stresses, are therefore also not computed here. By the same considerations, the temperature-dependence of the material properties is also neglected. The magnitudes of the stresses in Eq. (3.4) and the time-averaged heat generation term in Eq. (3.7) are thus approximated as stationary.

Since there is no variation in the stress distribution in the ϕ-direction, and hence no variation in the heat generation in that direction, heat diffusion takes place only in the $r\theta$-plane. The Fourier Law of Conduction in spherical coordinates [125] thus simplifies, in each medium m, to:

$$\rho_m c_{p_m} \frac{\partial T}{\partial t} = \kappa_m \left[\frac{1}{r^2} \frac{\partial}{\partial r} \left(r^2 \frac{\partial T}{\partial r} \right) + \frac{1}{r^2 \sin\theta} \frac{\partial}{\partial \theta} \left(\sin\theta \frac{\partial T}{\partial \theta} \right) \right] + q_m, \tag{3.15}$$

where κ and c_p denote, respectively, the thermal conductivity and specific heat capacity at constant pressure.

The boundary conditions in the θ-coordinate, in both the particle and the binder, are specified by the requirement of zero heat flux in the θ-direction at $\theta = 0$ and $\theta = \pi$, due to the symmetry of the stresses and heat generation about the $\theta = 0$ axis. At the particle–binder boundary, $r = a$, the conductive interface requires continuity

of the temperature and heat flux. At the outer boundary of the binder, $r = r_{outer}$, the convective surface condition is applied, with convection coefficient Λ_0. Finally, the remaining boundary condition in the radial coordinate in the particle is given by continuity of the heat flux at $r = 0$. The boundary conditions in the r- and θ-coordinates can thus be summarized, respectively, as:

$$\begin{aligned}
\kappa_2 \frac{\partial T}{\partial r}(0,\theta,t) &= -\kappa_2 \frac{\partial T}{\partial r}(0,\theta+\pi,t), \\
T(a^-,\theta,t) &= T(a^+,\theta,t), \\
\kappa_2 \frac{\partial T}{\partial r}(a^-,\theta,t) &= \kappa_1 \frac{\partial T}{\partial r}(a^+,\theta,t), \\
\kappa_1 \frac{\partial T}{\partial r}(r_{outer},\theta,t) &= \Lambda_0 \left[T_0 - T(r_{outer},\theta,t)\right], \\
\kappa_m \frac{\partial T}{\partial \theta}(r,0,t) &= 0, \\
\kappa_m \frac{\partial T}{\partial \theta}(r,\pi,t) &= 0,
\end{aligned} \tag{3.16}$$

where the superscripts $-$ and $+$ denote the limits from the negative and positive radial directions, respectively, and T_0 is the constant ambient temperature. The initial condition is specified as an isothermal state at the ambient temperature:

$$T(r,\theta,0) = T_0. \tag{3.17}$$

The heat transfer equation, Eq. (3.15), was solved in this work by a finite difference method, implemented in MATLAB®. The Crank-Nicholson method [156], an implicit, second-order scheme in time, was used to solve for the evolution of the temperature. Similarly, for the spatial derivatives, a second-order central difference approximation was used for all interior mesh points, and also for the boundary condition at $r = r_{outer}$. For the boundary conditions at the particle–binder interface, $r = a$, second-order backward and forward difference approximations were used for the negative and positive limits, respectively. Due to the singularities in the analytical heat equation at $r = 0$, $\theta = 0$, and $\theta = \pi$, first-order finite difference approximations were employed for the application of the boundary conditions at those points.

Additional effects which are not taken into account in the proposed model, including interface effects (such as debonding and intermittent contact), chemical decompo-

sition or phase changes of the energetic crystal, and, as previously mentioned, thermal strains and the temperature-dependence of the material properties, are expected to play significant roles in the thermomechanics of energetic composites subjected to high-frequency excitation. However, since the thermal model presented here is valid in the limit of small temperature rises and perfect bonding of the crystal and binder, the analytical equations and temperature predictions may provide insight into the initial heating of these composite systems. Moreover, the relations provide a basis for understanding the quantitative effect of the various material and excitation parameters on the initial thermomechanics of such systems.

3.4 Numerical Results and Discussion

In order to illustrate the model predictions for a typical energetic crystal embedded in a viscoelastic medium, the case of a spherical cyclotetramethylene-tetranitramine (HMX, or octogen) crystal situated in a Sylgard® 184 binder is considered here. Sylgard® is a silicone-based elastomer, developed by the Dow Corning Corporation, and is typically employed as an encapsulant in electrical applications [157, 158]. It has, however, also been used as the binder material in polymer-based energetic composites [159, 160]. Moreover, for the purpose of the future experimental validation of model predictions, the optical transparency of Sylgard® may prove useful in providing a pathway for measurements on embedded crystals in configurations similar to that considered in this work.

The material properties of the Sylgard® 184 binder were taken as: density $\rho_1 = 1030$ kg/m^3 [158], longitudinal wave speed $v_{1L} = 1100$ m/s [161], shear wave speed $v_{1S} = 570$ m/s [161], longitudinal wave attenuation coefficient $\alpha_{1L} = 2.4$ dB/MHz/cm [162], thermal conductivity $\kappa_1 = 0.27$ W/(m-K) [158], and thermal diffusivity $\chi_1 = 1.02 \times 10^{-7}$ m^2/s [157]. The specific heat capacity is then specified by the relation $c_{p_1} = \kappa_1/(\rho_1\chi_1)$. No suitable value could be found in the literature for the shear wave attenuation coefficient in Sylgard®. In order to specify the missing material

parameter, the assumption was made that the imaginary part of the Poisson's ratio is negligible (i.e., $\mathrm{Im}[\tilde{\nu}_1] \approx 0$), an approximation that is supported by measurements on other polymers [163, 164]. All other material moduli can then be computed through the relations for linear viscoelastic media [66].

Since the crystal is modeled as a rigid particle, only the density of HMX is required to characterize its mechanical properties, which was taken as $\rho_2 = 1910$ kg/m^3 [165]. The particle radius was set as $a = 0.25$ mm, and the thermal properties were specified as $\kappa_2 = 0.4184$ W/(m-K) and $c_{p_2} = 1015$ J/(kg-K), taken at 21 °C [159]. For the heat transfer equation, the convection coefficient of the surrounding fluid was set as $\Lambda_0 = 5$ W/(m^2-K), which is within the range for the free convection of air [125], and the constant ambient (and initial) temperature T_0 was assumed to be 21 °C for consistency with the property specifications. The outer radius of the binder was specified as 20 times the particle radius: $r_{outer} = 5$ mm. Finally, except where the excitation frequency and amplitude are varied in Section 3.4.3, the incident wave frequency is given as $f = 500$ kHz ($f = \omega/[2\pi]$) and the amplitude is specified as $\Phi' = 1$ μm at the Sylgard® outer boundary $z = -r_{outer}$, $x = 0$ (thus, the wave potential amplitude at $z = 0$ is $\tilde{\Phi}_0 = \Phi' e^{j\tilde{k}_{1L} r_{outer}} / \tilde{k}_{1L}$).

3.4.1 Induced Stresses

The analytical model for the stresses induced by the harmonic ultrasonic excitation was applied to the HMX–Sylgard® system. The magnitudes of the nonzero stress components in the $r\theta$-plane are presented in Figure 3.2 for the radial and in-plane shear stresses, and in Figure 3.3 for the polar and azimuthal stresses. Note that only the stresses induced in the surrounding binder medium are computed, and the rigid crystal is shown as a null region in the figures. It should also be noted that an arbitrarily fine grid was used for the generation of these distributions, since the relations are analytical, but this grid differs from the mesh used for the finite difference method to solve the heat transfer equation, which is detailed in Section 3.4.2. As is

evident in Figure 3.2(a), the radial stress shows a maximum near the front edge of the crystal, at which point the constructive interference due to scattering is maximal, and also a local maximum in stress just behind the crystal, attributable to the harmonic motion of the crystal and binder in the z-direction. Additional stress concentrations of lower magnitudes are observed at greater distances in front of the crystal, which are caused by the constructive interference of the incident wave and the waves scattered from the crystal–binder interface.

The maxima of the magnitudes of the other stress components are lower than that of the radial stress. The shear stress in Figure 3.2(b) also shows stress concentrations near the crystal interface, but at locations offset from the front and rear of the crystal, at which points the shear wave scattering is strongest. The shear waves then propagate at the scattered angles through the lossy medium. The polar stress in Figure 3.3(a) exhibits maximum values at larger angles with respect to the incident wave's propagation direction, since the induced normal stresses in the polar direction are strongest at these angles. Lastly, in Figure 3.3(b), the variation in the azimuthal stress magnitude, as for the radial stress, shows stress concentrations at several locations of constructive interference in front of the crystal, as well as over a small region immediately behind the crystal.

3.4.2 Heat Generation and Thermal Response

The time-averaged volumetric heat generation was computed by application of Eqs. (3.7), (3.8), and (3.9) to the stresses computed in Section 3.4.1. The result is presented as Figure 3.4, where the same arbitrarily fine grid as was used for the stresses has been employed to show the analytical solution. The maximum in the heat generation is observed directly in front of the crystal, and the elevated heating induced at several additional points of constructive interference in the z-direction in front of the crystal is also evident. Though the heat generation distribution is largely dominated by the radial stress component, the effects of the in-plane shear stress and

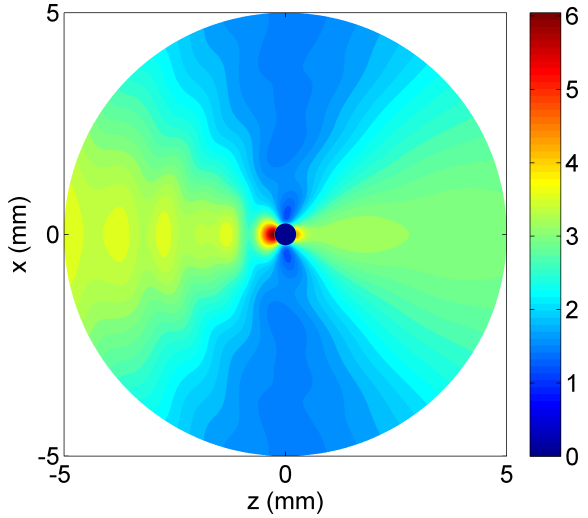

(a)

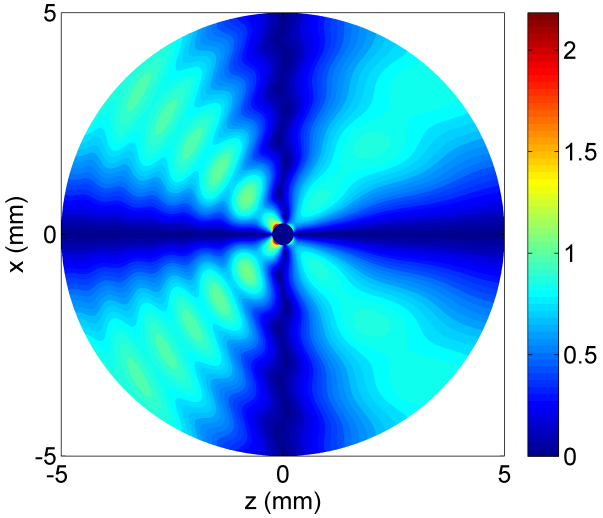

(b)

Figure 3.2. The magnitudes (in MPa) of the (a) radial stress $\tilde{\sigma}_{rr}$ and (b) shear stress $\tilde{\sigma}_{r\theta}$ induced in the HMX–Sylgard® system by a 1-μm, 500-kHz longitudinal plane wave traveling in the positive z-direction.

polar stress are readily apparent as well, with appreciable heating observed along the shear wave scattering angles and along the vertical direction near the crystal. The

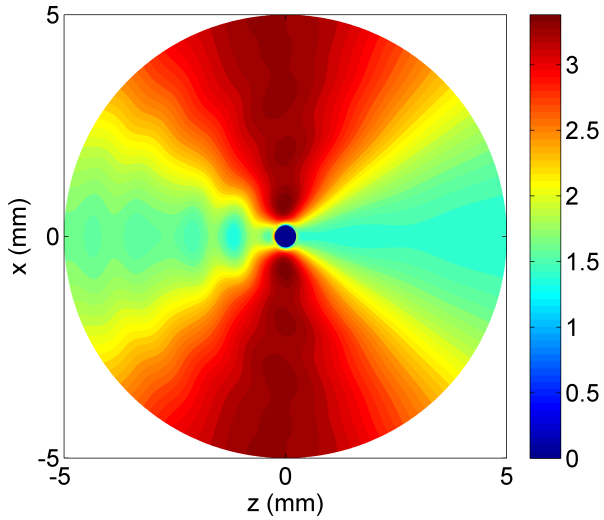

(a)

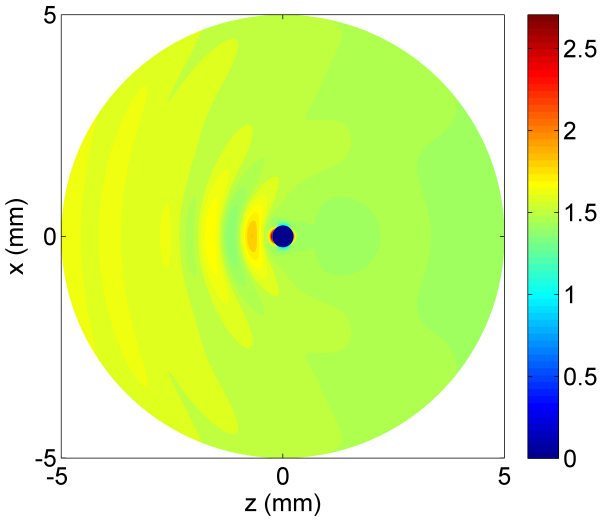

(b)

Figure 3.3. The magnitudes (in MPa) of the (a) polar stress $\tilde{\sigma}_{\theta\theta}$ and (b) azimuthal stress $\tilde{\sigma}_{\phi\phi}$ induced in the HMX–Sylgard® system by a 1-μm, 500-kHz longitudinal plane wave traveling in the positive z-direction.

effects of the azimuthal stress are less prominent, but also influence the topology of the heating distribution, particularly near the crystal–binder interface.

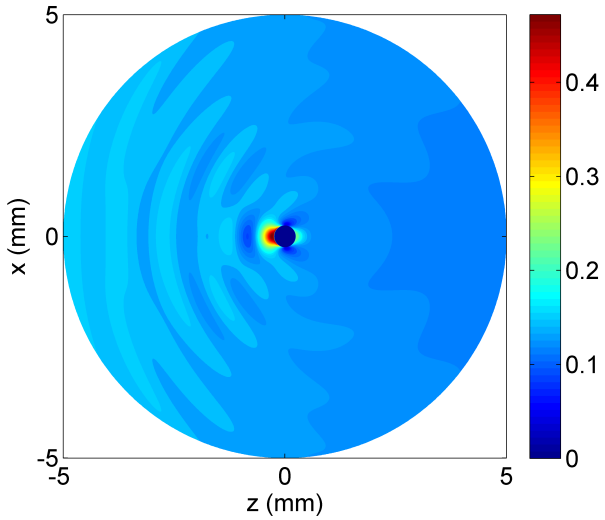

Figure 3.4. The time-averaged volumetric heat generation q (in W/mm^3) induced in the HMX–Sylgard® system by a 1-μm, 500-kHz longitudinal plane wave traveling in the positive z-direction.

The heat transfer equation was solved by the finite difference scheme described in Section 3.3.2. The spatial mesh was specified to consist of 241-points in the r-coordinate from $r = 0$ to r_{outer}, and 121-points in the θ-coordinate from $\theta = 0$ to π. The solution was then mirrored over the line of symmetry $\theta = 0$ for the purpose of plotting the full distributions. The condition of temperature continuity at the particle–binder interface was enforced by specifying $r = a$ as one of the mesh points. For the implicit Crank-Nicholson method [156], 100 time steps were used to advance the temperature solution from $t = 0$ to 0.5 s. The temperature results with respect to both the spatial and temporal mesh sizes were observed to converge to within a tolerance of 1%.

The predictions for the maximum transient temperatures of the crystal and binder are presented in Figure 3.5. Though the maximum heat generation is induced near the crystal–binder interface, noticeably larger temperature rises are observed in the binder due to its lower thermal conductivity as compared to the crystal. The location of the maximum crystal temperature is, as expected, at the nearest point on the incident

side ($x = 0$, $z = -0.25$ mm), and the location of the maximum binder temperature is a small distance along the z-direction in front of the crystal, at $x = 0$, $z \approx -0.38$ mm for this particular excitation frequency. The maximum crystal temperature rises by about 32.6 °C over the 0.5 s of excitation, and the rate of temperature increase for the crystal approaches approximately 55 °C/s.

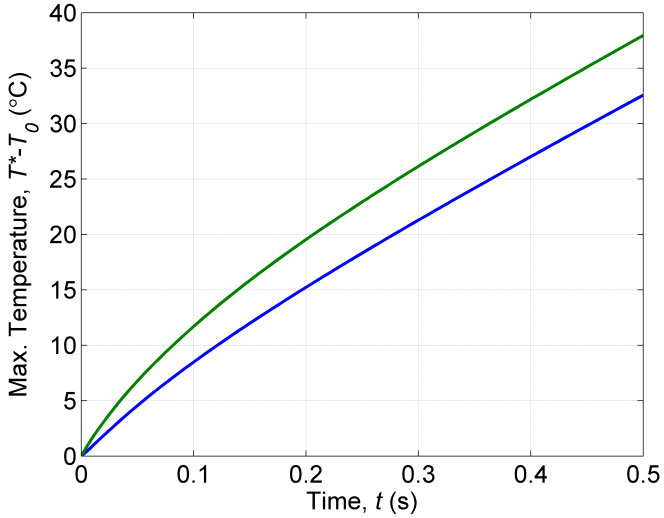

Figure 3.5. The maximum transient temperature increase in the crystal (blue curve) and binder (green curve) induced in the HMX–Sylgard® system by a 1-μm, 500-kHz longitudinal plane wave.

The computed temperature distribution at $t = 0.5$ s is shown as Figure 3.6. The point of the maximum thermal response in the binder, located close to the crystal interface, is clearly evident. The local maxima in temperature that appear at the stress concentrations along the z-direction in front of the crystal are also apparent, as are the lesser temperature rises at angles offset from the incident wave propagation direction, where the shear stress and polar stress contribute significantly to the heat generation. The minimum temperature in the system is located at a point within the back half of the crystal, where the thermal diffusion induced by the greater heat generation near the front surface of the crystal meets the diffusion induced by the lower heat generation near the back surface. The results presented here indicate

that viscoelastic heating of the binder material induced by the applied excitation is significant, particularly near the crystal, and that this heating mechanism is likely to play an important role in the formation of hot spots at the crystal–binder interface. It should be further noted that this heating is predicted in the absence of voids or debonding between the crystal and binder, but that these interface effects may also contribute substantially to the response through frictional heating.

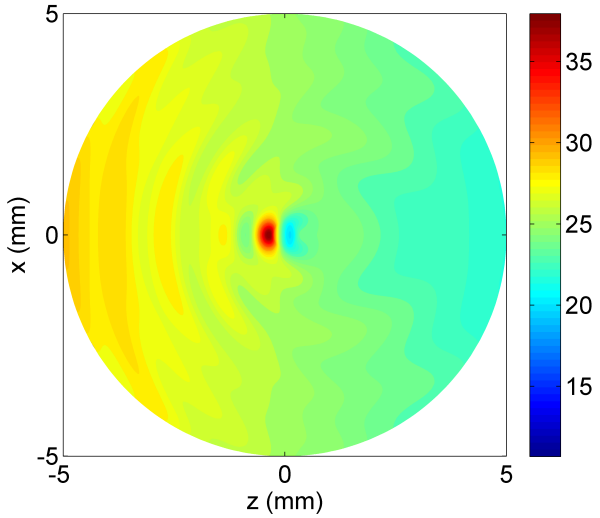

Figure 3.6. The temperature distribution (in °C above ambient T_0) at $t = 0.5$ s induced in the HMX–Sylgard® system by a 1-μm, 500-kHz longitudinal plane wave traveling in the positive z-direction.

3.4.3 Effects of Excitation Amplitude and Frequency

In the context of the cyclic loading of energetic composites, the excitation parameters, in contrast with the material properties in the system, are considered tunable to a degree, and so the quantitative effect of these parameters on the thermal response is of interest here. Specifically, the effects of varying the incident wave amplitude and frequency on the maximum crystal temperature are investigated.

Figure 3.7(a) shows the effect of varying the excitation amplitude on the maximum crystal temperature at $t = 0.5$ s and the corresponding rate of temperature increase.

The amplitude Φ' is, as before, specified at the Sylgard® outer boundary $z = -5$ mm, $x = 0$. Since the dynamic model for the stresses is linear, each of the stress components scales directly with the amplitude and, therefore, the volumetric heat generation scales with the square of the amplitude. As such, the temperature increases and the corresponding heating rates exhibit a simple quadratic variation with the incident wave amplitude, which is evident in Figure 3.7(a). Though the predicted thermal response shows large temperature increases for higher excitation amplitudes, the resulting thermal strains, changes in material properties, interface effects, and physical and chemical changes would have to be taken into account to accurately assess the temperature evolution and distribution.

The effect of varying the excitation frequency is presented in Figure 3.7(b), again considering both the maximum crystal temperature at $t = 0.5$ s and the corresponding rate of temperature increase. The variation with frequency also resembles a quadratic dependence, but the relation is more complicated due to the frequency-dependence of the Bessel and Hankel function terms in the analytical solution for the stresses. As a result, the phase differences given in Eq. (3.9) for the volumetric heat generation term also vary with frequency, in addition to the linear dependence of the heating shown in Eq. (3.7) and the variation of the stress magnitudes. It should be noted, too, that for the case of linear variation of the wave attenuation coefficients with frequency, specified in this work by the longitudinal coefficient $\alpha_{1L} = 2.4$ dB/MHz/cm and the condition $\mathrm{Im}[\tilde{\nu}_1] = 0$, the phases of the material moduli are independent of frequency. But if the frequency-dependence of the attenuation coefficients is not linear, then the changes in the phases of the material moduli would further contribute to the variation of the phase differences in Eq. (3.9). As for the amplitude variation, additional effects related to the temperature increases, as well as to the frequency levels, should be considered to accurately assess the thermal response at the higher excitation frequencies.

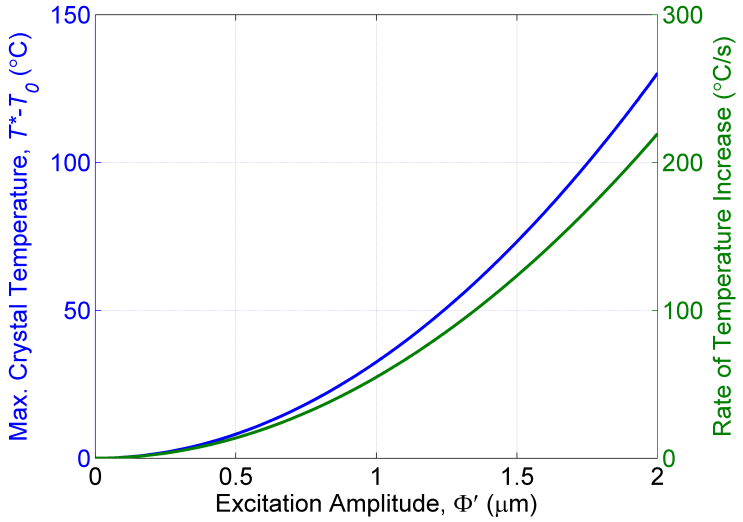

(a)

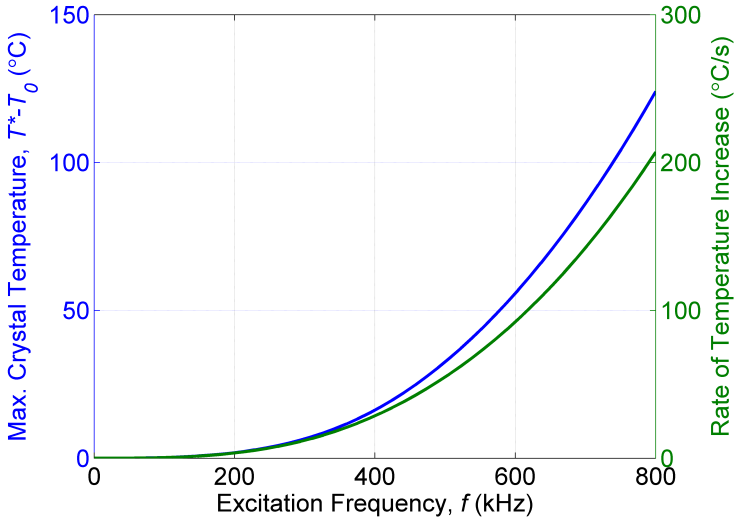

(b)

Figure 3.7. The maximum crystal temperature at $t = 0.5$ s (blue curve) and corresponding rate of temperature increase (green curve) in the HMX–Sylgard® system as a function of incident wave (a) amplitude and (b) frequency.

3.5 Conclusions

In this chapter, the thermomechanical response of a system consisting of a rigid spherical crystal embedded in a viscoelastic medium under harmonic longitudinal

plane wave excitation was considered. An analytical model for the viscoelastic heating of the binder was developed for general three-dimensional stress-strain states and was used in conjunction with a numerical solution scheme and an analytical stress solution to predict the temperature distribution and evolution in the binder and crystal. Numerical results were presented for the case of an HMX crystal embedded in a Sylgard® 184 binder, with the excitation frequency set at 500 kHz and the excitation amplitude set at 1 μm. The results reveal that significant heat generation and temperature rises are predicted near the front edge of the embedded crystal, due to the stress concentrations induced by the scattering of the incident wave. Moreover, the poor thermal conductivity of the viscoelastic binder material exacerbates the local temperature increases. Locations of elevated heat generation, though on a lower level than that near the crystal, were also predicted within the binder medium at locations of constructive interference, corresponding to lesser stress concentrations. For the nominal case considered in this chapter, viscoelastic heating of the binder resulted in a rate of temperature increase of approximately 55 °C/s for the energetic crystal, which is comparable to that estimated from an analogous set of experiments by Mares et al. [55].

The model was presented as an idealized case, with a single crystal and where perfect bonding at the crystal–binder interface was maintained, in order to isolate the effect of the viscoelastic heating of the binder material, specifically near the crystal. The substantial heating which is predicted even in the absence of defects or debonding at the interface suggests that this heating mechanism may play a significant role in the formation of hot spots near the crystal under applied excitation. Moreover, the model provides a basis for quantifying the thermal response elicited by this mechanism, which may prove useful in systems which target the heating of the composite material for enhanced trace detection capabilities. It should be noted, however, that beyond relatively short excitation times, additional mechanisms of heat generation are expected to become significant, such as thermal stresses and debonding at the crystal–binder interface, changes in material properties, and physical or

chemical changes (such as decomposition) of the energetic crystal. In addition, crystal morphology has been shown to impact the heat generation of similar systems [58], with additional stress concentrations introduced by irregular morphologies, so the results presented here for the spherical particle may represent a conservative estimate of the viscoelastic heating levels in the binder material.

In the chapters that follow, the focus of this work transitions from the prediction of the heating rates under known harmonic stress distributions to the form of incident acoustical or ultrasonic waves which may efficiently generate such stress and energy distributions in solid materials, with the incident wave specified in a fluid (such as air) and considering the interface phenomena. As such, Chapter 4 first considers idealized (lossless) material interfaces, and Chapters 5 and 6 subsequently increase the complexity of the model to include material dissipation as well as asymmetrical, bounded incident waveforms.

4. ACOUSTIC ENERGY TRANSMISSION INTO ELASTIC SOLIDS BY INHOMOGENEOUS PLANE WAVES

4.1 Introduction

In the context of the excitation of polymer-bonded energetic materials, particularly hidden explosives, remote excitation is preferable to contact excitation due to the volatile nature of the target materials. Low-frequency acoustic waves may represent an intriguing pathway to standoff excitation, given their relatively low attenuation in air and the ability to potentially transmit energy through metal barriers. Conversely, higher-frequency waves offer the benefit of greater near-field energy fluxes, but present challenges with respect to the high attenuation coefficients in air. Broadly speaking, applications which seek to excite energetic materials for the purpose of generating heat and increasing vapor pressures would require efficient transmission of the incident wave energy into the target specimen. In either frequency regime, however, acoustic energy transmission from air into typical solid materials, as well as into typical liquid media, is generally severely limited by the reflection and refraction at the interface, which are attributable to the large differences in the densities and wave speeds among the two media [77, 78, 166]. Moreover, from a theoretical point of view, in ideal or lossless media, it is well-known that homogeneous plane waves transmit no energy above the critical angle for the fluid–fluid or fluid–solid interface, an angle which is typically quite small given the large differences in wave speeds with air as the incident fluid.

However, if spatially-decaying incident plane waves are considered, termed inhomogeneous or evanescent plane waves, energy can be transmitted across the interface even above the critical angle of incidence for lossless media. By introducing a decaying component into the incident trace wavenumber, the wavenumber components of

the transmitted wave are composed of both propagating and decaying terms for all oblique angles of incidence. Consequently, the surface normal wavenumber in the second material (i.e., in the medium below the interface) has a nonzero propagating (real) part and energy thus propagates away from the interface into the second medium. The transmitted intensity then decays with distance into the second medium due to the spatial decay characteristics of the incident, and transmitted, waves.

In relation to Chapters 2 and 3, this chapter, along with Chapters 5 and 6, serves to inform the spatial distribution of the incident wave pressure (through analytical predictions) which will most efficiently transmit energy into solid materials. As such, this portion of the work represents a fundamental study of the incident wave parameters in the context of fluid–solid interfaces, particularly air–solid interfaces, for the purpose of maximizing the energy transmission into the solid. For the sake of convenience, the pressure fields in a fluid (or stress fields in a solid) of homogeneous and evanescent plane waves are shown conceptually here in Figure 4.1, as were shown previously in Figure 1.5. This investigation seeks to tune the rate of spatial amplitude decay of incident inhomogeneous waves, as is evident in Figure 4.1(b), along with the incidence angle, in the context of the energy transmission.

The purpose of this chapter, in particular, is thus to characterize the energy transmission across idealized material interfaces for incident inhomogeneous plane waves, in order to uncover incident wave parameters which maximize the transmission. To this end, a model of evanescent plane waves and their transmission across lossless fluid–fluid and fluid–solid interfaces is developed based on the theory presented by Brekhovskikh [77], and numerical results are presented for an air–water interface and for typical air–solid interfaces. Of particular interest is the result for the air–solid interface (or, generically, a given fluid–solid interface) that, with incidence near the Rayleigh angle, a unique value for the decay rate of the incident wave can be found such that no reflected wave is generated at the interface, which is attributable to the exact matching of the incident impedance by the sum of the impedance contributions from the transmitted longitudinal and transverse, or shear, waves. Moreover, in the

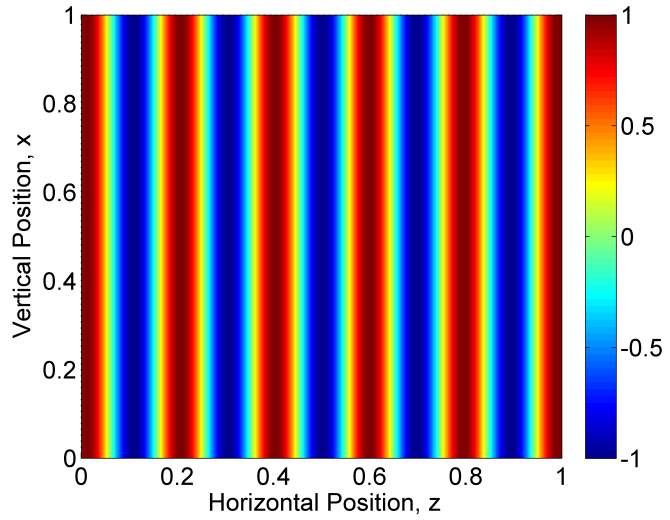

(a)

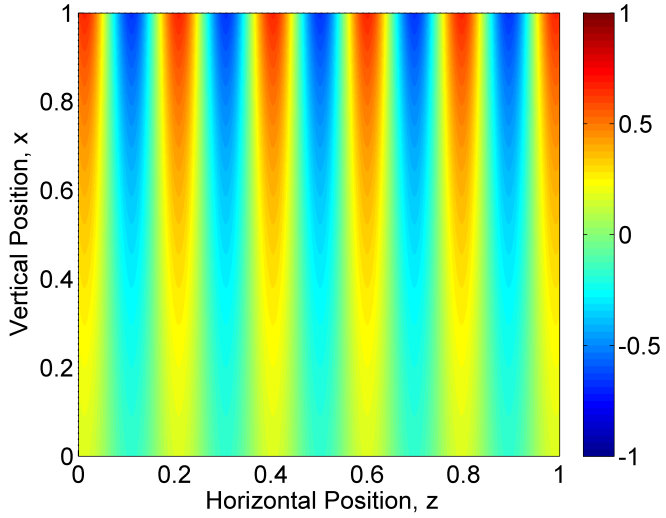

(b)

Figure 4.1. The pressure field, shown conceptually, of a plane wave propagating in a lossless medium with the wave as (a) homogeneous and (b) evanescent, or inhomogeneous. Arbitrary scalings are used for the purpose of illustration.

region near the zero of the reflection coefficient, the energy transmitted across the interface can be increased substantially, compared to homogeneous plane waves below

the critical angle. Major portions of this chapter first appeared in the Journal of the Acoustical Society of America [167].

4.2 Representation of Evanescent Plane Waves in Lossless Media

For a harmonic plane wave traveling in a homogeneous, isotropic fluid of constant speed of sound (longitudinal wave speed) v_L and away from material interfaces (i.e., in free space), the complex acoustic pressure $\tilde{p}$ can be represented as [78]:

$$\tilde{p} = \tilde{p}_0 e^{j(\omega t - \vec{K}\cdot\vec{r})}, \tag{4.1}$$

where $\tilde{p}_0$ is the complex amplitude, ω is the angular frequency, t is the time variable, $\vec{K}$ is the wavevector, and $\vec{r}$ is the position vector. When utilizing a Cartesian coordinate system, the position vector can be expressed in terms of the respective unit vectors: $\vec{r} = x\hat{e}_x + y\hat{e}_y + z\hat{e}_z$. The wavevector can likewise be expressed, for an arbitrary direction of propagation, as:

$$\vec{K} = k_x\hat{e}_x + k_y\hat{e}_y + k_z\hat{e}_z, \tag{4.2}$$

where the k_n are the wavevector components in the respective directions. For plane longitudinal waves propagating in a linear, inviscid fluid, the wavevector and the wavevector components satisfy the relation [78]:

$$\vec{K}\cdot\vec{K} = k_x^2 + k_y^2 + k_z^2 = \left(\frac{\omega}{v_L}\right)^2. \tag{4.3}$$

The scalar quantity $k = \omega/v_L$ is known as the material wavenumber. Since no shear waves are sustained in an inviscid fluid, the wavenumber k can be written here, omitting the subscript L for longitudinal waves, without ambiguity.

Homogeneous plane waves exhibit a constant pressure amplitude and phase on any plane perpendicular to the propagation direction. That is, in the absence of material dissipation, the pressure does not decay in any dimension for the harmonic wave. Such homogeneous plane waves are thus represented by real components k_n in the wavevector, which together give the direction of propagation.

In contrast, evanescent waves are disturbances which show an exponential decay in one or more dimensions. Examples include surface waves, such as Rayleigh, Lamb, and Stoneley waves, as well as bulk evanescent waves [77, 97, 101]. In general, such inhomogeneous waves may simultaneously decay and propagate in arbitrary directions. Each of the wavevector components is represented as a complex quantity, where the real part represents propagation and the imaginary part represents exponential decay of the wave, in the respective dimensions: $\tilde{k}_x = k_{x,\Re} - jk_{x,\Im}$, $\tilde{k}_y = k_{y,\Re} - jk_{y,\Im}$, and $\tilde{k}_z = k_{z,\Re} - jk_{z,\Im}$. Substitution of the complex components into Eq. (4.1) yields:

$$\tilde{p} = \tilde{p}_0 e^{-k_{x,\Im}x - k_{y,\Im}y - k_{z,\Im}z} e^{j(\omega t - k_{x,\Re}x - k_{y,\Re}y - k_{z,\Re}z)}. \tag{4.4}$$

Note that the real parts of the wavevector components give the direction of phase propagation, $\vec{P} = k_{x,\Re}\hat{e}_x + k_{y,\Re}\hat{e}_y + k_{z,\Re}\hat{e}_z$, and the imaginary parts give the direction of amplitude attenuation, $\vec{A} = k_{x,\Im}\hat{e}_x + k_{y,\Im}\hat{e}_y + k_{z,\Im}\hat{e}_z$. The complex wavevector can thus be written as: $\tilde{\vec{K}} = \vec{P} - j\vec{A}$.

In non-dissipative media, evanescent waves decay along a vector perpendicular to the direction of propagation, and the propagation and decay characteristics can be represented by complex angles of propagation. By using this representation, the angles can be integrated directly into the theory for homogeneous waves, including interactions at material interfaces. In the case of two-dimensional propagation, one of the wavevector components is zero, and the wave characteristics can be represented by a single complex angle.

Figure 4.2 shows a two-dimensional (i.e., $\tilde{k}_y = 0$) plane wave propagating in free space. Using the complex angle $\tilde{\theta} = \theta_\Re + j\theta_\Im$ (in radians), the wavevector components $\tilde{k}_x$ and $\tilde{k}_z$ are determined, as for a real angle, by using the sine and cosine functions:

$$\begin{aligned}
\tilde{k}_x &= k\sin(\theta_\Re + j\theta_\Im) \\
&= k\sin(\theta_\Re)\cosh(\theta_\Im) + jk\cos(\theta_\Re)\sinh(\theta_\Im), \\
\tilde{k}_z &= k\cos(\theta_\Re + j\theta_\Im) \\
&= k\cos(\theta_\Re)\cosh(\theta_\Im) - jk\sin(\theta_\Re)\sinh(\theta_\Im).
\end{aligned} \tag{4.5}$$

In this formulation, the imaginary part of the complex angle prescribes the rate of exponential decay. The wave decays as $e^{-\beta\Delta}$, where Δ is the position measured perpendicular to the propagation direction, and the decay parameter β is given by:

$$\beta = k\sinh(\theta_{\Im}). \tag{4.6}$$

Substitution of Eq. (4.5) into Eq. (4.1) yields:

$$\tilde{p} = \tilde{p}_0 e^{-\beta[-\cos(\theta_{\Re})x+\sin(\theta_{\Re})z]} e^{j[\omega t - k\sin(\theta_{\Re})\cosh(\theta_{\Im})x - k\cos(\theta_{\Re})\cosh(\theta_{\Im})z]}. \tag{4.7}$$

The real component $\theta_{\Re}$ of the complex angle thus gives the physical direction of propagation, and the imaginary part $\theta_{\Im}$ controls the decay rate and the effect of the decay on phase propagation. Note also that the phase is constant on any plane perpendicular to the propagation direction, but the amplitude is not.

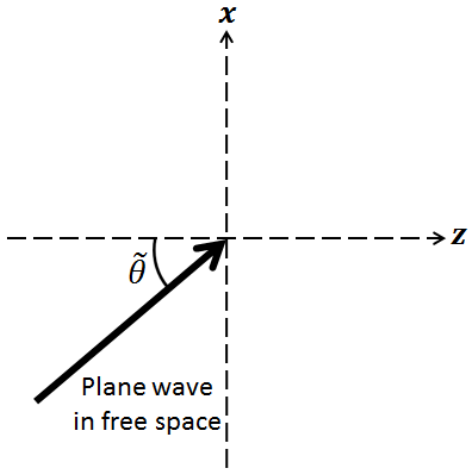

Figure 4.2. A diagram of a two-dimensional plane wave propagating in free space.

The sense of decay along the line perpendicular to the propagation direction is determined by the sign of the imaginary part $\theta_{\Im}$. If the decay parameter β is prescribed, then the value of $\theta_{\Im}$ which represents the corresponding rate of decay can be obtained by inverting Eq. (4.6):

$$\theta_{\Im} = \pm\ln\left(\frac{|\beta|}{k} + \left[\left(\frac{\beta}{k}\right)^2 + 1\right]^{1/2}\right), \tag{4.8}$$

where the sign of $\theta_{\Im}$ coincides with that of β.

Evanescent plane waves of the type discussed here are spatially-distributed disturbances of infinite extent. An analogy can be made with spatially-distributed waves that exhibit concentrated peaks in amplitude, such as Gaussian beams. However, in the case of evanescent plane waves, the unidirectional spatial decay characteristics perpendicular to the direction of propagation imply growth without bound in the opposite direction, which is clearly not possible. That being said, like homogeneous plane waves, the representation can be a reasonable approximation over a given region of space, where the pressure phase is approximately constant on any perpendicular plane and where the pressure amplitude varies exponentially [95, 98].

4.3 Evanescent Wave Transmission across Material Interfaces

For acoustic waves traveling in air, or in other low-density fluids, energy transmission into liquid or solid media is generally limited by the large impedance-difference, which causes significant reflection at the interface [77, 78, 166]. In addition, liquid and solid media typically have wave speeds much greater than the speed of sound in air, which causes significant refraction beyond the interface in the liquid or solid medium. It is well-known that for incident homogeneous plane waves, no energy can be transmitted across an elastic interface above the critical angle, and an exponentially decaying pressure field is generated in the second medium. In terms of the wavevector, the transmitted wave propagates along ("clings to") the interface, and the surface normal wavevector component is purely imaginary. Thus, no energy propagates away from the interface and into the second medium.

However, for incident evanescent plane waves which simultaneously propagate and decay, energy can be transmitted at physical angles above the critical angle. Through the introduction of a decaying component in the incident trace wavenumber, the transmitted trace wavenumber (e.g., $\tilde{k}_x$) is given both propagating and decaying components for all oblique incidence angles, which in turn also yields propagating and decaying terms in the transmitted normal wavenumber (e.g., $\tilde{k}_z$) to satisfy Eq. (4.3).

Therefore, the transmitted wave travels at a physical angle below the interface line, with a nonzero real part of the normal wavenumber, and energy can propagate away from the interface into the second material.

Evanescent wave transmission is investigated here for a single material interface, where homogeneous, isotropic, linear, lossless media occupy the two acoustic half-spaces on either side of the interface. The incident medium is assumed to be a fluid, and both fluid and solid media are considered for the second medium. As was previously discussed, the fluid media under consideration support longitudinal waves, but cannot sustain shear waves. The fluids on the incident and transmission sides of the interface are thus characterized by densities ρ_1 and ρ_2, respectively, and longitudinal wave speeds v_{1L} and v_{2L}, respectively. In solids, transverse waves can also propagate, and the solid medium is additionally characterized by the shear wave speed v_{2S}. For homogeneous wave incidence, $\theta_{cr} = \arcsin(v_{1L}/v_{2L})$ gives the critical angle for longitudinal waves and, in the case of the solid medium, $\theta_{crS} = \arcsin(v_{1L}/v_{2S})$ gives the critical angle for shear waves. For small ratios v_{1L}/v_{2L} and v_{1L}/v_{2S}, the critical angles are close to zero, or normal incidence, which prevents energy transmission for most angles. However, as alluded to above, the use of incident evanescent waves effectively eliminates the critical angle criterion.

4.3.1 Fluid–Fluid Interface

A diagram of the fluid–fluid interface is shown in Figure 4.3 for two-dimensional propagation in the xz-plane, where a right-handed rectangular coordinate system is assumed. In general, reflected and transmitted longitudinal waves are generated at the interface. The incident wave is assumed to decay perpendicular to the direction of propagation, and is represented by the complex angle $\tilde{\theta}_1 = \theta_{1,\Re} + j\theta_{1,\Im}$. The reflected angle matches that of the incident wave, and the transmitted angle is denoted as $\tilde{\theta}_{2L} = \theta_{2L,\Re} + j\theta_{2L,\Im}$, where the subscript L is included to indicate the transmitted wave as longitudinal, as distinct from the transmitted shear wave that will be included

in the next section with a solid material as the second medium. The details of the computation of the transmitted angle, and transmitted wavevector, are given in Section 4.3.5. Since both fluid media are considered linear and inviscid, no shear waves propagate on either side of the interface.

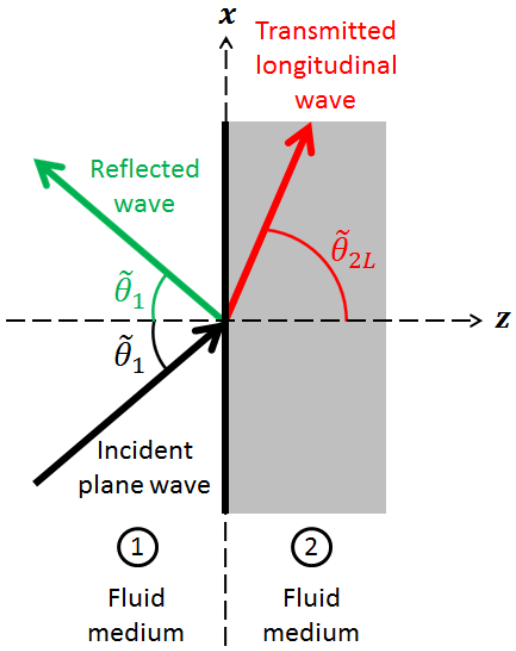

Figure 4.3. A diagram of the incident, reflected, and transmitted waves at the fluid–fluid interface.

The pressure and particle velocity associated with the transmitted wave can be derived by using the longitudinal wave potentials [77]. The displacement potential on the incident side of the interface is the sum of the potentials associated with the incident and reflected waves:

$$\tilde{\Phi}_1 = \tilde{\Phi}_0 e^{j\left[\omega t - k_1 \sin(\tilde{\theta}_1)x\right]} \left[e^{-jk_1 \cos(\tilde{\theta}_1)z} + \tilde{R} e^{jk_1 \cos(\tilde{\theta}_1)z}\right], \tag{4.9}$$

where $\tilde{\Phi}_0$ is the potential amplitude of the incident wave, $\tilde{R}$ is the reflection coefficient, and $k_1 = \omega/v_{1L}$ is the material wavenumber in the incident fluid. On the transmission

side, the only disturbance is the transmitted longitudinal wave, whose potential, using the associated transmission coefficient $\tilde{\mathcal{T}}_L$, is given as:

$$\tilde{\Phi}_2 = \tilde{\Phi}_0 \tilde{\mathcal{T}}_L e^{j\left[\omega t - k_{2L}\sin(\tilde{\theta}_{2L})x - k_{2L}\cos(\tilde{\theta}_{2L})z\right]}, \tag{4.10}$$

where $k_{2L} = \omega/v_{2L}$ is the material wavenumber of the second fluid. (Note the use of the scripted letter $\mathcal{T}$ here for the transmission coefficient, to distinguish it from the temperature T defined in Chapters 2 and 3.)

The boundary conditions at the interface (i.e., at $z = 0$) require continuity of the normal component of the particle displacement and continuity of the normal stress [77]. The displacement vector in either medium m is calculated as the gradient of the wave potential: $\vec{\tilde{u}}_m = \nabla\tilde{\Phi}_m$. The normal displacements in the fluids on the incident and transmission sides of the interface are thus computed as $\tilde{u}_{1,z} = \partial\tilde{\Phi}_1/\partial z$ and $\tilde{u}_{2,z} = \partial\tilde{\Phi}_2/\partial z$, respectively. The corresponding particle velocities are simply the time derivatives of the displacements: $\partial\tilde{u}_{m,z}/\partial t = j\omega\tilde{u}_{m,z}$. Continuity of the trace wavenumber $\tilde{k}_x$ across the interface, also known as generalized Snell's law, follows from the normal displacement condition:

$$k_1\sin(\tilde{\theta}_1) = k_{2L}\sin(\tilde{\theta}_{2L}). \tag{4.11}$$

The normal stresses in the first and second media are given by $\tilde{\sigma}_{1,zz} = \rho_1 v_{1L}^2 \nabla^2\tilde{\Phi}_1$ and $\tilde{\sigma}_{2,zz} = \rho_2 v_{2L}^2 \nabla^2\tilde{\Phi}_2$, respectively.

The solution of the two boundary conditions at the interface yields the expressions for the coefficients $\tilde{R}$ and $\tilde{\mathcal{T}}_L$ [77]:

$$\begin{aligned} \tilde{R} &= \frac{\tilde{Z}_{2L} - \tilde{Z}_{1L}}{\tilde{Z}_{2L} + \tilde{Z}_{1L}}, \\ \tilde{\mathcal{T}}_L &= \frac{\rho_1}{\rho_2}\left(\frac{2\tilde{Z}_{2L}}{\tilde{Z}_{2L} + \tilde{Z}_{1L}}\right), \end{aligned} \tag{4.12}$$

where $\tilde{Z}_{1L} = \rho_1 v_{1L}/\cos(\tilde{\theta}_1)$ and $\tilde{Z}_{2L} = \rho_2 v_{2L}/\cos(\tilde{\theta}_{2L})$ are the surface normal impedances for longitudinal waves in the first and second fluids, respectively.

In the first and second media, the pressures can be deduced, respectively, as $\tilde{p}_1 = \rho_1\omega^2\tilde{\Phi}_1$ and $\tilde{p}_2 = \rho_2\omega^2\tilde{\Phi}_2$. It can be observed that the pressure amplitude $\tilde{p}_0$ of the incident wave is related to the amplitude $\tilde{\Phi}_0$ of its wave potential by $\tilde{p}_0 = \rho_1\omega^2\tilde{\Phi}_0$.

The normal particle velocities on each side of the interface can be calculated directly from the wave potentials by using the expressions given above. In the first and second fluids, the normal velocities can be expressed, respectively, as:

$$\begin{aligned} \frac{\partial \tilde{u}_{1,z}}{\partial t} &= \frac{\tilde{p}_0}{\tilde{Z}_{1L}} e^{j\left[\omega t - k_1 \sin(\tilde{\theta}_1)x\right]} \left[e^{-jk_1\cos(\tilde{\theta}_1)z} - \tilde{R}e^{jk_1\cos(\tilde{\theta}_1)z}\right], \\ \frac{\partial \tilde{u}_{2,z}}{\partial t} &= \frac{\rho_2}{\rho_1}\left(\frac{\tilde{p}_0\tilde{\mathcal{T}}_L}{\tilde{Z}_{2L}}\right) e^{j\left[\omega t - k_{2L}\sin(\tilde{\theta}_{2L})x - k_{2L}\cos(\tilde{\theta}_{2L})z\right]}. \end{aligned} \tag{4.13}$$

4.3.2 Fluid–Solid Interface

The analysis presented in the previous section is extended here to the case of a solid medium on the transmission side of the interface. Solid materials support shear stresses, so transmitted shear waves are also generated by the interaction at the interface. Figure 4.4 shows a diagram of the fluid–solid interface, where a right-handed rectangular coordinate system is again assumed. The shear wave propagates at the transmitted shear angle, $\tilde{\theta}_{2S} = \theta_{2S,\Re} + j\theta_{2S,\Im}$, and with the shear wave speed v_{2S} in the solid medium. The details of the computation of the transmitted shear angle and wavevector are likewise given in Section 4.3.5.

Of particular note for the fluid–solid interface is the phenomena which occur near the Rayleigh angle. Rayleigh waves constitute a particular surface wave solution to the wave equation whereby the longitudinal and shear waves travel at a common velocity along the interface of the solid half-space, which may be bordered by vacuum or, for generalized Rayleigh waves, by an ambient fluid [77, 168, 169]. If a homogeneous plane wave in the ambient fluid is incident at the elastic interface above the critical angle, a Rayleigh-type surface wave is generated whose energy, in the absence of material dissipation, is reemitted into the fluid to yield total reflection, and no bulk wave is transmitted. In contrast, if an evanescent plane wave is incident on the

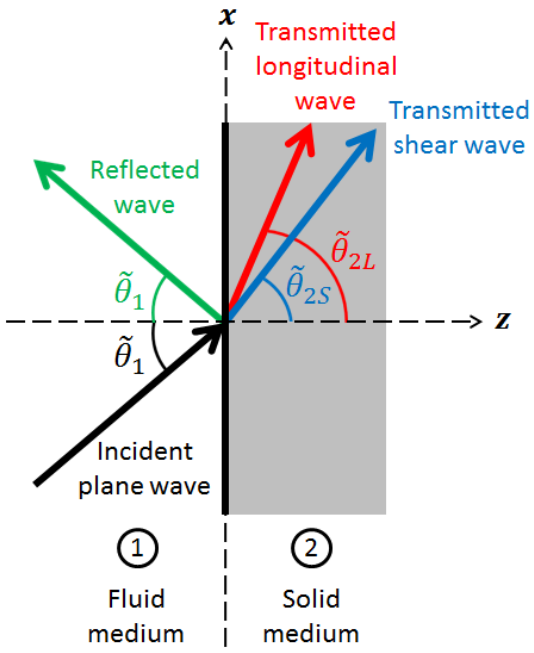

Figure 4.4. A diagram of the incident, reflected, and transmitted waves at the fluid–solid interface.

solid, bulk evanescent waves (both longitudinal and shear) are transmitted, and the amplitudes are greatest at the Rayleigh angle. A minimum in the reflection coefficient is observed at this angle [97, 101], owing to the resonance phenomenon (and increased transmission) that occurs when the excitation is coincident with the free wave solution. Thus, the use of an incident evanescent wave, in generating the transmitted bulk waves, provides a mechanism for energy to propagate below the interface, which is maximized at the Rayleigh angle.

The Rayleigh wave speed v_{Ray} for an elastic half-space is computed from the characteristic equation [77, 168]:

$$\left(\frac{v_{Ray}}{v_{2S}}\right)^6 - 8\left(\frac{v_{Ray}}{v_{2S}}\right)^4 + \left[24 - 16\left(\frac{v_{2S}}{v_{2L}}\right)^2\right]\left(\frac{v_{Ray}}{v_{2S}}\right)^2 - 16\left[1 - \left(\frac{v_{2S}}{v_{2L}}\right)^2\right] = 0, \tag{4.14}$$

which has a unique positive real root such that $v_{Ray} < v_{2S}$. The Rayleigh angle can be subsequently computed as $\theta_{Ray} = \arcsin(v_{1L}/v_{Ray})$.

The derivation for the fluid–solid interface parallels that of the fluid–fluid interface, except that, in general, transverse waves also exist in the solid medium [77]. The longitudinal potential is as given in Eq. (4.10), and the shear wave potential is given by:

$$\tilde{\Psi}_2 = \tilde{\Phi}_0 \tilde{\mathcal{T}}_S e^{j\left[\omega t - k_{2S}\sin(\tilde{\theta}_{2S})x - k_{2S}\cos(\tilde{\theta}_{2S})z\right]}, \tag{4.15}$$

where $\tilde{\mathcal{T}}_S$ is the transmission coefficient for the shear wave potential and $k_{2S} = \omega/v_{2S}$ is the material shear wavenumber in the solid material.

The boundary conditions at the interface require, as before, continuity of the normal particle displacement and continuity of the normal stress. In addition, the shear stress must also be continuous across the interface, which necessitates that the shear stress in the solid be zero at the interface, since the incident fluid medium is assumed to be inviscid, and so cannot sustain shear waves [77]. The displacement vector in the solid medium is computed as the sum of the gradient of the longitudinal potential and the curl of the shear potential's associated vector field $\vec{\tilde{\Psi}}_2$: $\vec{\tilde{u}}_2 = \nabla\tilde{\Phi}_2 + \nabla\times\vec{\tilde{\Psi}}_2$. For the case of two-dimensional propagation, the shear potential field is simply $\vec{\tilde{\Psi}}_2 = \tilde{\Psi}_2\hat{e}_y$, and the normal displacement in the solid reduces to $\tilde{u}_{2,z} = \partial\tilde{\Phi}_2/\partial z + \partial\tilde{\Psi}_2/\partial x$. The normal velocity is again simply the associated time derivative. Continuity of the trace wavenumber, which also includes the shear trace wavenumber $\tilde{k}_{2S,x} = k_{2S}\sin(\tilde{\theta}_{2S})$, again follows from the normal displacement condition:

$$k_1\sin(\tilde{\theta}_1) = k_{2L}\sin(\tilde{\theta}_{2L}) = k_{2S}\sin(\tilde{\theta}_{2S}). \tag{4.16}$$

The normal stress in the solid medium also includes contributions from the shear wave potential, and is given as [77]:

$$\tilde{\sigma}_{2,zz} = \rho_2 v_{2L}^2 \nabla^2\tilde{\Phi}_2 + 2\rho_2 v_{2S}^2\left(\frac{\partial^2\tilde{\Psi}_2}{\partial x\partial z} - \frac{\partial^2\tilde{\Phi}_2}{\partial x^2}\right). \tag{4.17}$$

Similarly, the shear stress in the solid, which must be zero at the interface, is expressed as [77]:

$$\tilde{\sigma}_{2,xz} = \rho_2 v_{2S}^2\left(2\frac{\partial^2\tilde{\Phi}_2}{\partial x\partial z} + \frac{\partial^2\tilde{\Psi}_2}{\partial x^2} - \frac{\partial^2\tilde{\Psi}_2}{\partial z^2}\right). \tag{4.18}$$

Solving for the three boundary conditions at the interface yields the expressions for the coefficients $\tilde{R}$, $\tilde{\mathcal{T}}_L$, and $\tilde{\mathcal{T}}_S$. Brekhovskikh [77] gives the solution in terms of the transmitted shear angle $\tilde{\theta}_{2S}$:

$$\begin{aligned}
\tilde{R} &= \frac{\tilde{Z}_{2L}\cos^2(2\tilde{\theta}_{2S}) + \tilde{Z}_{2S}\sin^2(2\tilde{\theta}_{2S}) - \tilde{Z}_{1L}}{\tilde{Z}_{2L}\cos^2(2\tilde{\theta}_{2S}) + \tilde{Z}_{2S}\sin^2(2\tilde{\theta}_{2S}) + \tilde{Z}_{1L}}, \\
\tilde{\mathcal{T}}_L &= \frac{\rho_1}{\rho_2}\left[\frac{2\tilde{Z}_{2L}\cos(2\tilde{\theta}_{2S})}{\tilde{Z}_{2L}\cos^2(2\tilde{\theta}_{2S}) + \tilde{Z}_{2S}\sin^2(2\tilde{\theta}_{2S}) + \tilde{Z}_{1L}}\right], \\
\tilde{\mathcal{T}}_S &= \frac{\rho_1}{\rho_2}\left[\frac{2\tilde{Z}_{2S}\sin(2\tilde{\theta}_{2S})}{\tilde{Z}_{2L}\cos^2(2\tilde{\theta}_{2S}) + \tilde{Z}_{2S}\sin^2(2\tilde{\theta}_{2S}) + \tilde{Z}_{1L}}\right],
\end{aligned} \tag{4.19}$$

where $\tilde{Z}_{2S} = \rho_2 v_{2S}/\cos(\tilde{\theta}_{2S})$ is the surface normal impedance for shear waves in the solid medium.

The pressure in the incident fluid is again given by $\tilde{p}_1 = \rho_1\omega^2\tilde{\Phi}_1$. In the solid, the transmitted normal and shear stresses can be expanded and written, respectively, in terms of the pressure amplitude $\tilde{p}_0$ of the incident wave as:

$$\begin{aligned}
\tilde{\sigma}_{2,zz} = \frac{\rho_2\tilde{p}_0}{\rho_1}\Bigg\{ & \tilde{\mathcal{T}}_L\left[2\left(\frac{v_{2S}}{v_{2L}}\right)^2\sin^2(\tilde{\theta}_{2L}) - 1\right]e^{j\left[\omega t - k_{2L}\sin(\tilde{\theta}_{2L})x - k_{2L}\cos(\tilde{\theta}_{2L})z\right]} \\
& - \tilde{\mathcal{T}}_S\sin(2\tilde{\theta}_{2S})e^{j\left[\omega t - k_{2S}\sin(\tilde{\theta}_{2S})x - k_{2S}\cos(\tilde{\theta}_{2S})z\right]}\Bigg\}, \\
\tilde{\sigma}_{2,xz} = \frac{\rho_2\tilde{p}_0}{\rho_1}\Bigg\{ & \tilde{\mathcal{T}}_S\cos(2\tilde{\theta}_{2S})e^{j\left[\omega t - k_{2S}\sin(\tilde{\theta}_{2S})x - k_{2S}\cos(\tilde{\theta}_{2S})z\right]} \\
& - \tilde{\mathcal{T}}_L\left(\frac{v_{2S}}{v_{2L}}\right)^2\sin(2\tilde{\theta}_{2L})e^{j\left[\omega t - k_{2L}\sin(\tilde{\theta}_{2L})x - k_{2L}\cos(\tilde{\theta}_{2L})z\right]}\Bigg\}.
\end{aligned} \tag{4.20}$$

Finally, the particle velocities in the solid medium can be computed from the wave potentials using the expression given above. For the normal and tangential components of the velocity, this yields, respectively:

$$\begin{aligned}
\frac{\partial \tilde{u}_{2,z}}{\partial t} &= \frac{\rho_2 \tilde{p}_0}{\rho_1}\left\{ \frac{\tilde{\mathcal{T}}_L}{\tilde{Z}_{2L}} e^{j\left[\omega t - k_{2L}\sin(\tilde{\theta}_{2L})x - k_{2L}\cos(\tilde{\theta}_{2L})z\right]} \right. \\
&\qquad \left. + \frac{\tilde{\mathcal{T}}_S \sin(\tilde{\theta}_{2S})}{\rho_2 v_{2S}} e^{j\left[\omega t - k_{2S}\sin(\tilde{\theta}_{2S})x - k_{2S}\cos(\tilde{\theta}_{2S})z\right]} \right\}, \\
\frac{\partial \tilde{u}_{2,x}}{\partial t} &= \frac{\rho_2 \tilde{p}_0}{\rho_1}\left\{ \frac{\tilde{\mathcal{T}}_L \sin(\tilde{\theta}_{2L})}{\rho_2 v_{2L}} e^{j\left[\omega t - k_{2L}\sin(\tilde{\theta}_{2L})x - k_{2L}\cos(\tilde{\theta}_{2L})z\right]} \right. \\
&\qquad \left. - \frac{\tilde{\mathcal{T}}_S}{\tilde{Z}_{2S}} e^{j\left[\omega t - k_{2S}\sin(\tilde{\theta}_{2S})x - k_{2S}\cos(\tilde{\theta}_{2S})z\right]} \right\}.
\end{aligned} \tag{4.21}$$

4.3.3 Intensity Transmission

In non-dissipative media, the instantaneous intensity of a given wave is the rate of energy transmission per unit area in the direction of propagation [78, 166]. For harmonic waves, the instantaneous intensity can be time-averaged to give what is known as the "acoustic intensity," or simply the intensity. The intensity is represented as a vector $\vec{I}$, where the components correspond to the acoustic intensities in the respective directions. For stress tensor $\tilde{\sigma}_{ln}$ and velocity vector $\partial \tilde{u}_l / \partial t$, the components of the instantaneous energy flux vector (per unit area) are expressed as [100, 101, 170]:

$$\mathcal{E}_n(t) = -\sum_{l=1}^{3} \mathrm{Re}\left[\tilde{\sigma}_{ln}\right] \mathrm{Re}\left[\frac{\partial \tilde{u}_l}{\partial t}\right], \tag{4.22}$$

where Re denotes the real part of the argument and the subscripts 1, 2, and 3 correspond to the x, y, and z directions, respectively. The intensity is computed by time-averaging the energy flux over one period:

$$I_n = \frac{\omega}{2\pi} \int_{t_0}^{t_0 + 2\pi/\omega} \mathcal{E}_n(t)\, \mathrm{d}t, \tag{4.23}$$

where t_0 is an arbitrary time.

An inviscid fluid cannot support shear stresses, so by using the pressure ($\tilde{p} = -\tilde{\sigma}_{xx} = -\tilde{\sigma}_{zz}$), the tangential and normal intensities can be computed conveniently

as $I_x = \mathrm{Re}[\tilde{p}\ \partial\tilde{u}_x^*/\partial t]/2$ and $I_z = \mathrm{Re}[\tilde{p}\ \partial\tilde{u}_z^*/\partial t]/2$, where the asterisk denotes the complex conjugate. In the solid, however, these expressions cannot be used, as the contributions of the shear stresses to the energy flux must be taken into account [100, 170]. The longitudinal and transverse waves propagate with different wavenumbers along the respective dimensions and the phase difference must be incorporated by time-averaging according to Eq. (4.23), where the instantaneous intensities are $\mathcal{E}_x = -(\mathrm{Re}[\tilde{\sigma}_{xx}]\mathrm{Re}[\partial\tilde{u}_x/\partial t] + \mathrm{Re}[\tilde{\sigma}_{xz}]\mathrm{Re}[\partial\tilde{u}_z/\partial t])$ and $\mathcal{E}_z = -(\mathrm{Re}[\tilde{\sigma}_{zz}]\mathrm{Re}[\partial\tilde{u}_z/\partial t] + \mathrm{Re}[\tilde{\sigma}_{xz}]\mathrm{Re}[\partial\tilde{u}_x/\partial t])$.

For the incident evanescent waves under consideration, the transmitted normal wavenumbers (i.e., $\tilde{k}_{2L,z}$ and, in the case of the solid, $\tilde{k}_{2S,z}$) have both propagating and decaying components, corresponding to their real and imaginary parts, respectively. Energy thus propagates away from the interface and into the second material. In terms of the normal intensity expression, the normal particle velocity is related to the wave pressure, or stress, by the normal wavenumber. When the real part is taken in computing the intensity, the real (propagating) component of the normal wavenumber yields nonzero intensity transmission across the material interface. Conversely, for the case of homogeneous waves incident beyond the critical angle, the transmitted normal wavenumber is purely imaginary and no energy is transmitted; all of the energy is reflected back into the incident medium.

4.3.4 Energy Conservation in the System

If energy is to be conserved, the energy fluxes approaching and leaving the interface, which are given by the normal intensities I_z in the two media taken at $z = 0$, must balance. Since the boundary conditions at the interface require continuity of the normal particle velocity and continuity of the stress tensor, it can be readily observed from Eq. (4.22) that the normal intensities are equal at $z = 0$, and energy is conserved at the interface.

Moreover, energy conservation within the media in the presence of the evanescent disturbances can also be demonstrated. It can be shown that, in the absence of material dissipation, there is no net energy flux through any closed control surface $\mathcal{S}$, which may be constructed in either medium or which may stretch across the interface, since the energy flux is continuous through the interface plane [100, 101]. The net energy flux through the closed surface is thus given by the surface integral:

$$\oiint_{\mathcal{S}} \vec{I}_m \cdot \mathrm{d}\vec{\mathcal{S}} = 0, \tag{4.24}$$

where $\mathrm{d}\vec{\mathcal{S}}$ is the differential area element on the control surface, oriented along the outward normal vector to the surface, and m denotes the appropriate medium for the given differential element of $\mathcal{S}$. For the case of two-dimensional propagation in the xz-plane, there is no variation in the y-direction, and the control surface can be replaced by a closed curve $\mathcal{C}$ in the xz-plane. The surface integral is therefore replaced by a line integral to give the net energy flux per unit width:

$$\oint_{\mathcal{C}} \vec{I}_m \cdot \mathrm{d}\vec{\mathcal{C}} = 0, \tag{4.25}$$

where $\mathrm{d}\vec{\mathcal{C}}$ is the differential line element of the curve, oriented along the outward normal vector.

4.3.5 Calculation of Transmitted Wavevectors

For two-dimensional propagation in the xz-plane, the transmitted wavevector can be computed using the condition for trace wavenumber continuity, $\tilde{k}_{1,x} = \tilde{k}_{2L,x}$, and the condition for the material wavenumber, Eq. (4.3). The transmitted trace wavenumber $\tilde{k}_{2L,x}$ is simply that of the incident wave. By using the material wavenumber of the second medium k_{2L} and Eq. (4.3), the transmitted normal wavenumber is:

$$\tilde{k}_{2L,z} = \pm \left(k_{2L}^2 - \tilde{k}_{2L,x}^2 \right)^{1/2}, \tag{4.26}$$

where the sign should be chosen to yield a negative imaginary part, which represents decay with distance into the second medium. This is equivalent to using the principal square root [66].

In the case of the solid medium on the transmission side of the interface, the shear wavevector must also be computed. Again using the condition for trace wavenumber continuity, the transmitted shear trace wavenumber $\tilde{k}_{2S,x}$ is also that of the incident wave: $\tilde{k}_{2S,x} = \tilde{k}_{1,x}$. And with the material shear wavenumber k_{2S}, the transmitted shear normal component can likewise be computed as:

$$\tilde{k}_{2S,z} = \pm \left(k_{2S}^2 - \tilde{k}_{2S,x}^2 \right)^{1/2}, \tag{4.27}$$

with the sign again chosen to yield a negative imaginary part.

For evanescent waves which decay along the line perpendicular to the direction of propagation, the transmitted angles can be computed directly, which can in turn be used to calculate the normal wavenumbers: $\tilde{k}_{2L,z} = k_{2L}\cos(\tilde{\theta}_{2L})$ and, for the solid, $\tilde{k}_{2S,z} = k_{2S}\cos(\tilde{\theta}_{2S})$. By writing the material wavenumbers in the trace wavenumber continuity equation, Eq. (4.16), in terms of the frequency and wave speeds, the frequency-dependence in the relation can be eliminated. Also, by expanding the sine terms, as in Eq. (4.5), and equating the real and imaginary parts, one obtains:

$$\begin{aligned} \sin(\theta_{2L,\Re}) &= \frac{v_{2L}}{v_{1L}} \left[\frac{\cosh(\theta_{1,\Im})}{\cosh(\theta_{2L,\Im})} \right] \sin(\theta_{1,\Re}), \\ \cos(\theta_{2L,\Re}) &= \frac{v_{2L}}{v_{1L}} \left[\frac{\sinh(\theta_{1,\Im})}{\sinh(\theta_{2L,\Im})} \right] \cos(\theta_{1,\Re}). \end{aligned} \tag{4.28}$$

It is assumed here that the real part $\theta_{1,\Re}$ of the incidence angle is positive and, thus, the imaginary part $\theta_{1,\Im}$ must also be positive to yield decay in the direction of the second medium. If the real part $\theta_{1,\Re}$ were negative, then $\theta_{1,\Im}$ would also be negative. In that case, the negative root in the transmitted angle component $\theta_{2L,\Im}$ would be chosen as the physical solution, again to yield decay with distance into the second material, but otherwise the computations are the same as those presented here.

The real part $\theta_{2L,\Re}$ of the transmitted angle satisfies the trigonometric identity:

$$\sin^2(\theta_{2L,\Re}) + \cos^2(\theta_{2L,\Re}) = 1, \tag{4.29}$$

and the substitution of the expressions from Eq. (4.28) yields:

$$\left[\frac{\cosh(\theta_{1,\Im})}{\cosh(\theta_{2L,\Im})}\right]^2 \sin^2(\theta_{1,\Re}) + \left[\frac{\sinh(\theta_{1,\Im})}{\sinh(\theta_{2L,\Im})}\right]^2 \cos^2(\theta_{1,\Re}) = \left(\frac{v_{1L}}{v_{2L}}\right)^2. \tag{4.30}$$

Since the incidence angle $\tilde{\theta}_1 = \theta_{1,\Re} + j\theta_{1,\Im}$ is known, $\theta_{2L,\Im}$ is the only unknown quantity in Eq. (4.30). The equation can be solved for any values of the wave speed ratio and incidence angle. Note first that the solution for $\theta_{2L,\Im}$ must be real, owing to the expanded form of the transmitted angle, $\tilde{\theta}_{2L} = \theta_{2L,\Re} + j\theta_{2L,\Im}$. At $\theta_{2L,\Im} = 0$, the value of the left-hand side of Eq. (4.30) is infinite. As $\theta_{2L,\Im}$ is increased from zero, the values of $\cosh(\theta_{2L,\Im})$ and $\sinh(\theta_{2L,\Im})$ increase monotonically, so the left-hand side decreases monotonically. Therefore, $\theta_{2L,\Im}$ can be increased until the value of the left-hand side matches the finite, positive value of the right-hand side, $(v_{1L}/v_{2L})^2$, to yield the unique solution $\theta^\star_{2L,\Im}$. The equation has even symmetry in $\theta_{2L,\Im}$, as each term in Eq. (4.30) is squared. However, the physical solution is the positive root in $\theta_{2L,\Im}$, which yields decay of the wave with distance into the second medium. Eq. (4.30) can thus be solved numerically for the unique positive real root to yield the solution $\theta^\star_{2L,\Im}$, which was the approach taken here. (Note, however, that Eq. (4.30) can alternatively be expressed in terms of exponentials by using the definitions of the hyperbolic functions. The resulting equation is eighth-order in $\theta_{2L,\Im}$, with even symmetry, which can be solved in closed form to yield up to eight distinct roots, of which the physical solution is the unique positive real root.)

To solve for the real part of the transmitted angle $\theta_{2L,\Re}$, either of the expressions in Eq. (4.28) can be inverted. By using the sine expression, the solution $\theta^\star_{2L,\Re}$ is given by:

$$\theta^\star_{2L,\Re} = \arcsin\left[\frac{v_{2L}\cosh(\theta_{1,\Im})\sin(\theta_{1,\Re})}{v_{1L}\cosh(\theta^\star_{2L,\Im})}\right]. \tag{4.31}$$

For the solid medium, the transmitted shear angle, $\tilde{\theta}_{2S} = \theta_{2S,\Re} + j\theta_{2S,\Im}$, can be computed by the same method. The quantities $\theta_{2L,\Re}$, $\theta_{2L,\Im}$, and v_{2L} should be replaced by $\theta_{2S,\Re}$, $\theta_{2S,\Im}$, and v_{2S}, respectively, in Eqs. (4.28)–(4.31).

4.4 Numerical Results and Discussion

The transmitted intensities were investigated for an air–water interface, and for various parameters which characterize typical air–solid interfaces. For the air–water interface, the pressure and normal particle velocity distributions in the water medium were also considered. For the air–solid interfaces, the normal stress distributions in the solid were considered, along with the normal particle velocity and intensity distributions. In the case of the solid media, conditions for zero reflection at the interface, and consequently total transmission of the incident normal intensity, were additionally explored.

It should be noted here that the boundary conditions at the interface were verified for each parameter variation considered. In addition, continuity of the energy flux within the two media was also verified, and computations of the flux passing through a sample control volume will be presented for both the air–water and the air–solid interface.

4.4.1 Air–Water Interface

Methods of energy transmission from the incident air medium into water may be of interest in numerous applications, but are limited for homogeneous plane waves by the critical angle criterion. Considered here is the case of air at 20 °C and 1 atm ($\rho_1 = 1.21$ kg/m^3, $v_{1L} = 343$ m/s), and fresh water under the same conditions ($\rho_2 = 998$ kg/m^3, $v_{2L} = 1481$ m/s) [78]. The critical angle for the interface is $\theta_{cr} \approx 13.4°$. The incident evanescent plane wave is given a pressure amplitude of $\tilde{p}_0 = 1$ Pa (i.e., as prescribed at the point $x = z = 0$) and a frequency of $f = 1000$ Hz ($f = \omega/[2\pi]$). The transmitted (and incident) pressures and velocities scale with the incident pressure magnitude $|\tilde{p}_0|$, and the intensities scale with $|\tilde{p}_0|^2$.

The transmitted normal intensity at the interface (i.e., at $z = 0$) and at the tangential position $x = 0$ was first considered as a function of the incidence angle component $\theta_{1,\Re}$, which gives the physical angle of propagation according to Eq. (4.7).

Figure 4.5 shows the transmitted normal intensity (at $x = z = 0$) as a function of the angle $\theta_{1,\Re}$ for several values of the decay parameter: $\beta = 0$, 0.001, 0.01, and 0.02 rad/m, where the case of a homogeneous plane wave ($\beta = 0$) is included to allow for direct comparison. It should be noted that the intensities of the evanescent waves vary with x and z according to the equations highlighted above. Below the critical angle, the evanescent wave intensities are close to those of homogeneous plane waves at the same incidence angles, with little variation with β. Above the critical angle, however, the intensity transmission from evanescent waves remains nonzero and increases with β, though larger values of β also yield more rapid decay with distance into the second medium. The transmitted intensities monotonically decrease with increasing incidence angles beyond the critical angle.

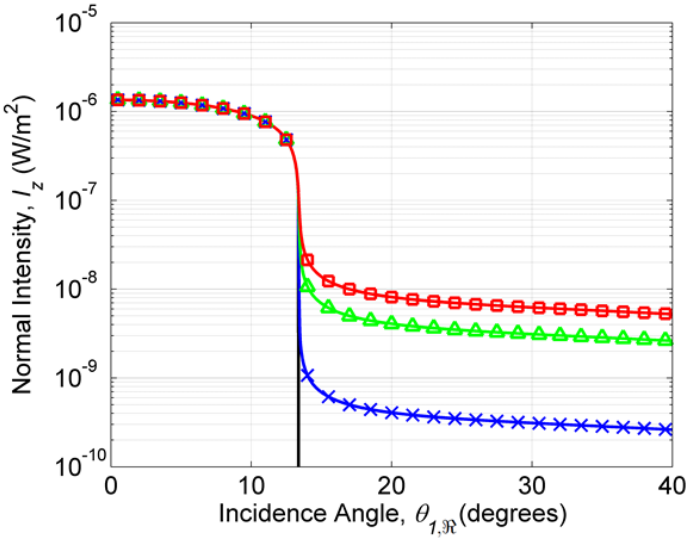

Figure 4.5. The transmitted normal intensity, at the interface and at tangential position $x = 0$, as a function of the incidence angle $\theta_{1,\Re}$ for the air–water interface. The markers as $\times$'s, triangles, and squares on the curves correspond to values of the decay parameter of $\beta = 0.001$, 0.01, and 0.02 rad/m, respectively. The unmarked curve corresponds to a homogeneous plane wave ($\beta = 0$). Note that a logarithmic scale has been used for the vertical axis.

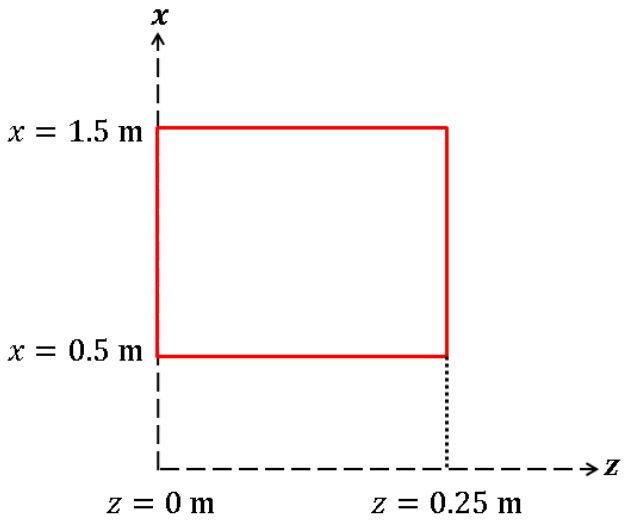

Figure 4.6. A sample closed curve constructed in the xz-plane in the second medium.

Energy conservation in the second medium is verified here by using an arbitrary sample control volume. Since there is no variation in the y-direction, a closed curve $\mathcal{C}$ was constructed and the net energy fluxes were given per unit width. The sample curve utilized here took the form of a rectangle in the xz-plane, stretching from $x = 0.5$ to 1.5 m and from $z = 0$ to 0.25 m, as shown in Figure 4.6. Using Eq. (4.25), the intensity vector in the second medium $\vec{I}_2(x, z)$, and the unit vectors along the respective coordinate axes ($\hat{e}_x$ and $\hat{e}_z$), the net energy fluxes in units of W/m entering and leaving the planar region (Q_I and Q_{II}, respectively) are given, with the sign convention, as:

$$\begin{aligned} Q_I &= \int_0^{0.25} \vec{I}_2(0.5, z) \cdot \hat{e}_x \, \mathrm{d}z + \int_{0.5}^{1.5} \vec{I}_2(x, 0) \cdot \hat{e}_z \, \mathrm{d}x \\ &= \int_0^{0.25} I_{2,x}(0.5, z) \, \mathrm{d}z + \int_{0.5}^{1.5} I_{2,z}(x, 0) \, \mathrm{d}x, \\ Q_{II} &= \int_0^{0.25} \vec{I}_2(1.5, z) \cdot \hat{e}_x \, \mathrm{d}z + \int_{0.5}^{1.5} \vec{I}_2(x, 0.25) \cdot \hat{e}_z \, \mathrm{d}x \\ &= \int_0^{0.25} I_{2,x}(1.5, z) \, \mathrm{d}z + \int_{0.5}^{1.5} I_{2,z}(x, 0.25) \, \mathrm{d}x, \end{aligned} \tag{4.32}$$

where the position values are given in m. The results of the computation are presented in Figure 4.7 as a function of the incidence angle, with the decay parameter set at a nominal value of $\beta = 0.01$ rad/m. It can be readily observed that the energy flux entering the volume matches the flux exiting the volume, so energy conservation is verified.

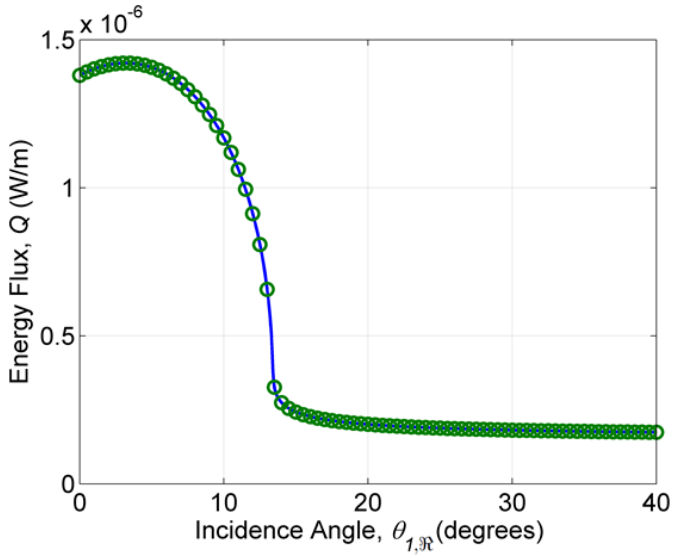

Figure 4.7. The net energy flux per unit width entering and leaving the sample control volume in water. The solid line and the markers as circles represent the net energy fluxes entering and leaving the volume, respectively. For visual clarity, the energy flux leaving the volume is shown with data points only at 0.5° increments.

The transmitted pressure, normal particle velocity, and normal intensity distributions were also investigated for subcritical and supercritical angles, with the decay parameter set at the nominal value of $\beta = 0.01$ rad/m. Figures 4.8 and 4.9 give the pressure, velocity, and intensity distributions in the second medium (water) at a subcritical angle of $\theta_{1,\Re} = 5°$. The dark bold line indicates the position of the interface ($z = 0$). The transmitted pressure wave propagates at an angle of approximately 22.1°. It can be observed that the normal particle velocity distribution is similar to that of the pressure, with a small phase difference introduced by the decay of the incident wave. The spatial dependence of the incident wave intensity can be

conceptualized as lines of constant intensity along the direction of propagation, which are refracted at the interface to yield the transmitted intensity distribution shown in Figure 4.9. The normal intensity of the transmitted wave is thus constant along the direction of propagation, but decays perpendicular to that direction. It should be noted that the spatial decay of the intensity, like the decay of the incident wave pressure, is a characteristic of the disturbance itself, and that no dissipation is included in the second medium. At a given tangential position x, the intensity decays with distance into the second material, and the rate of decay is relatively small for the large area shown.

The transmitted pressure, normal velocity, and normal intensity distributions are likewise presented in Figures 4.10 and 4.11 for the supercritical angle $\theta_{1,\Re} = 15°$. The decay parameter was again set at $\beta = 0.01$ rad/m. In this case, the transmitted wave propagates at an angle of approximately 89.7°. The angle is close to, but slightly less than, 90° (i.e., along the interface), so nonzero energy transmission occurs above the critical angle. The pressure and velocity distributions are out-of-phase with each other, and show the transmitted wave propagating at the slight angle with respect to the interface plane. The amplitudes peak at the interface and decay along a vector nearly aligned with the normal distance into the second medium. The refracted lines of constant intensity again lie along the direction of propagation, and as a result are slightly offset from the interface, as shown in Figure 4.11. Note that the angle of propagation, though still barely evident as deviating from the tangential axis, is exaggerated in the intensity plot since the horizontal position range is narrower than that of the vertical position. Like the pressure and velocity, the normal intensity distribution decays approximately normal to the interface but, since the pressure and velocity are out-of-phase, it does not show the same spatial variation near the interface. The intensity transmission for most supercritical angles is considerably less than that for the subcritical angles, but remains finite.

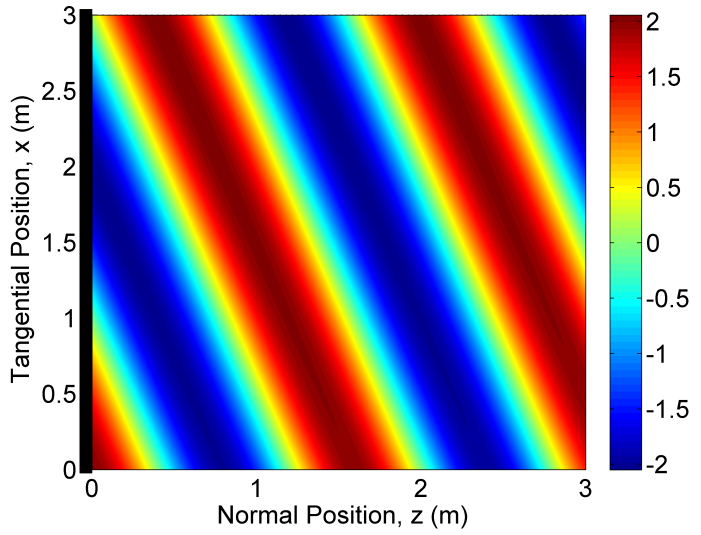

(a)

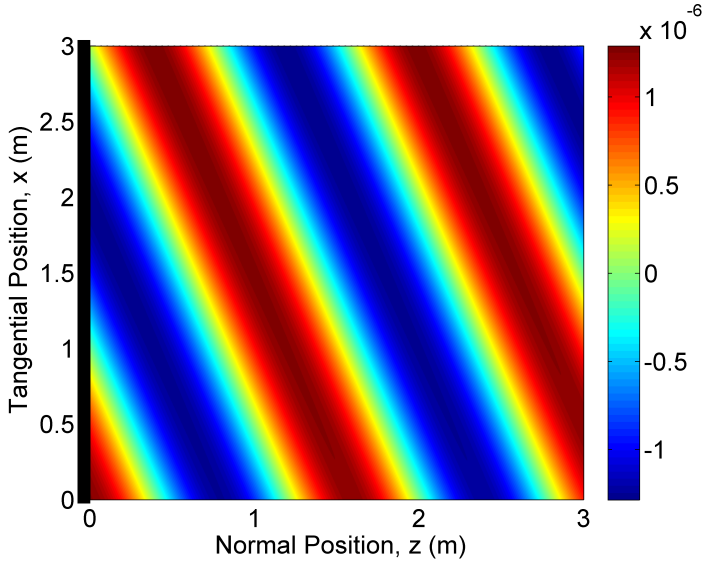

(b)

Figure 4.8. The subcritical transmitted distributions of (a) pressure (in Pa) and (b) normal velocity (in m/s) for the air–water interface. The subcritical angle is $\theta_{1,\Re} = 5^\circ$ and the decay parameter is $\beta = 0.01$ rad/m.

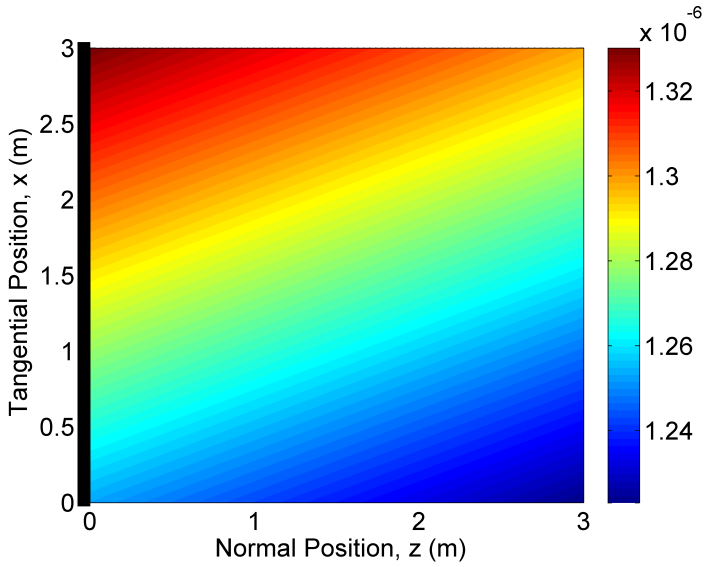

Figure 4.9. The subcritical transmitted normal intensity distribution (in W/m^2) for the air–water interface. The subcritical angle is $\theta_{1,\Re} = 5^\circ$ and the decay parameter is $\beta = 0.01$ rad/m.

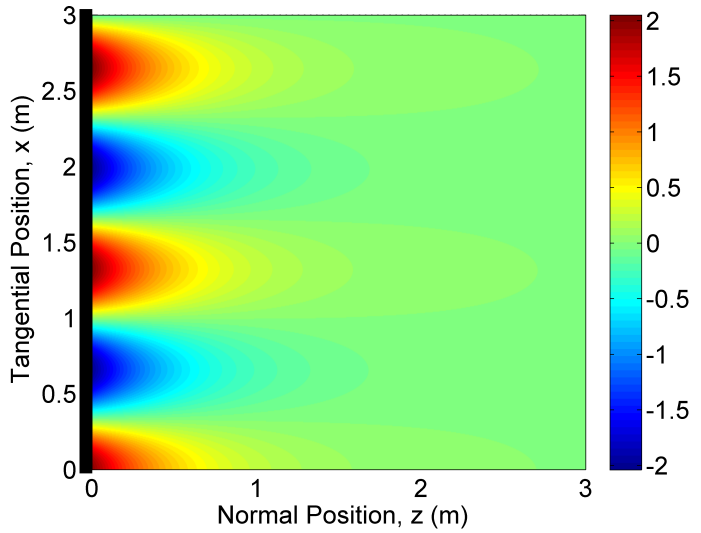

(a)

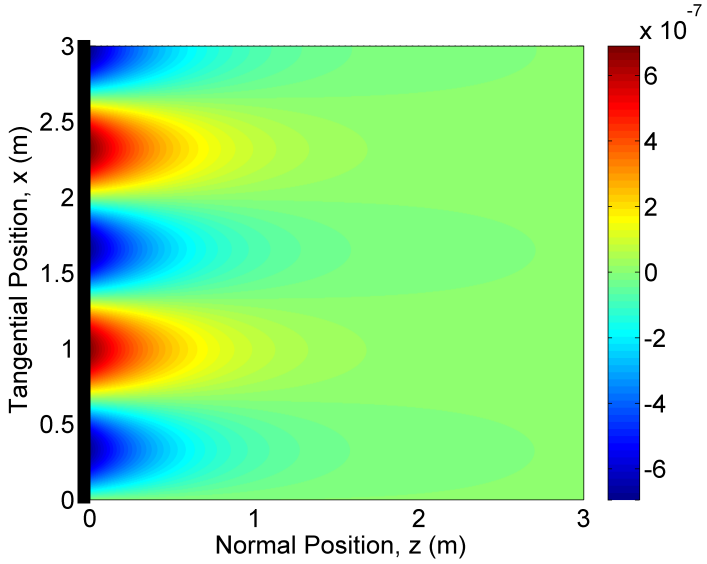

(b)

Figure 4.10. The supercritical transmitted distributions of (a) pressure (in Pa) and (b) normal velocity (in m/s) for the air–water interface. The supercritical angle is $\theta_{1,\Re} = 15^\circ$ and the decay parameter is $\beta = 0.01$ rad/m.

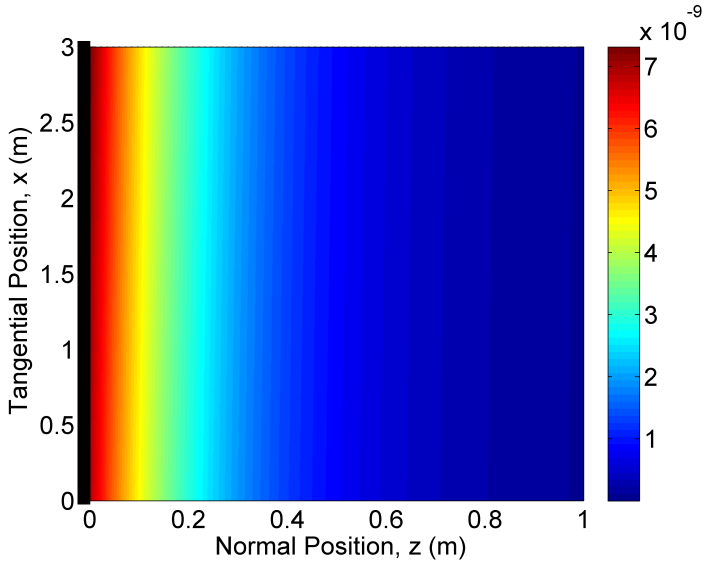

Figure 4.11. The supercritical transmitted normal intensity distribution (in $\mathrm{W/m^2}$) for the air–water interface. The supercritical angle is $\theta_{1,\Re} = 15°$ and the decay parameter is $\beta = 0.01$ rad/m. Note that the horizontal axis shows the decay over only the first 1 m away from the interface.

4.4.2 Air–Solid Interface

Though the air–water interface, as a typical fluid–fluid interface, demonstrates interesting results with respect to the energy transmission by incident evanescent waves, fluid–solid interfaces (particularly air–solid interfaces) are of primary interest for the application in this work. As such, an exemplary air–solid interface is considered in this section. The incident air medium is again taken at 20 °C and 1 atm ($\rho_1 = 1.21$ kg/m^3, $v_{1L} = 343$ m/s). Solid materials typically have densities at least 1000 times that of air, and longitudinal wave speeds at least 10 times the speed of sound in air. The density and longitudinal wave speed in the solid medium were thus set at $\rho_2 = 1210$ kg/m^3 ($\rho_2/\rho_1 = 1000$) and $v_{2L} = 3430$ m/s ($v_{2L}/v_{1L} = 10$), respectively. The shear wave speed in the solid was taken as $v_{2S} = 2400$ m/s ($v_{2S}/v_{1L} = 7$). The critical angles for the interface are $\theta_{cr} \approx 5.7°$ for transmitted longitudinal waves, and $\theta_{crS} \approx 8.2°$ for transmitted shear waves. The incident wave was again given a pressure amplitude of $\tilde{p}_0 = 1$ Pa and a frequency of $f = 1000$ Hz.

As for the air–water interface, the transmitted normal intensity, taken at the interface (i.e., at $z = 0$) and at the tangential position $x = 0$, was investigated as a function of the incidence angle component $\theta_{1,\Re}$. The normal intensity is shown in Figure 4.12 for decay parameter values of $\beta = 0$, 0.001, 0.01, and 0.02 rad/m, where the case of a homogeneous plane wave ($\beta = 0$) is again included for comparison. The evanescent wave intensities are again close to those of homogeneous plane waves for incidence below the critical angles, with negligible variation with β. Between the critical angles, $\theta_{cr} \approx 5.7°$ and $\theta_{crS} \approx 8.2°$, the intensities remain close to those of homogeneous plane waves, since the transmitted transverse waves dominate in this regime. However, whereas the transmission from homogeneous waves goes to zero above the critical angle for shear waves, the intensities from evanescent waves drop significantly slightly above that angle before climbing to a peak near 9.4°, which is the Rayleigh angle as predicted by the wave speed in Eq. (4.14). At this angle, the incident wave is coincident with the resonance phenomenon of coupled longitudinal

and shear waves in the solid half-space. This condition corresponds to a minimum in the reflection coefficient, and consequently maximum normal intensity transmission, which is discussed in depth in Section 4.4.4 below. Above the supercritical peak, the transmitted intensities monotonically decrease with further increasing incidence angles.

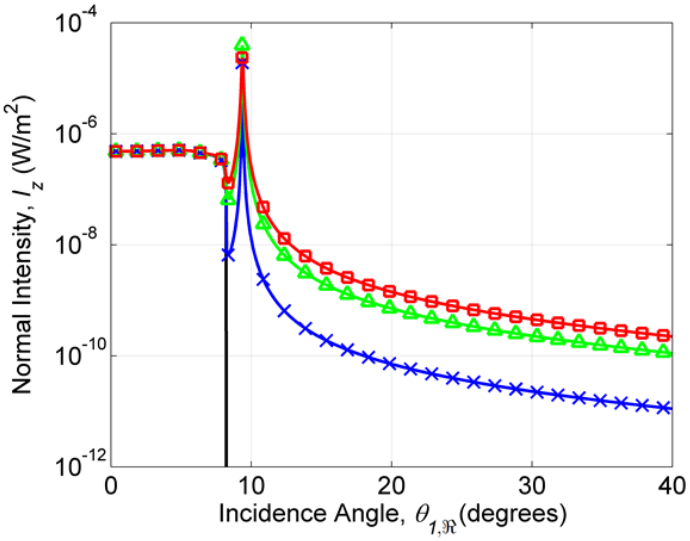

Figure 4.12. The transmitted normal intensity, at the interface and at tangential position $x = 0$, as a function of the incidence angle $\theta_{1,\Re}$ for the air–solid interface. The markers as $\times$'s, triangles, and squares on the curves correspond to values of the decay parameter of $\beta = 0.001$, 0.01, and 0.02 rad/m, respectively. The unmarked curve corresponds to a homogeneous plane wave ($\beta = 0$). Note that a logarithmic scale has been used for the vertical axis.

Energy conservation in the solid medium is verified here, again using the sample control curve shown in Figure 4.6. The intensity vector in the solid $\vec{I}_2(x, z)$ is computed with Eq. (4.23), and the net energy fluxes entering and leaving the planar region are again given by Eq. (4.32). The results of the computation are shown in Figure 4.13 as a function of the incidence angle, where the decay parameter is set at $\beta = 0.01$ rad/m. A large increase in energy flux is observed at the Rayleigh angle, attributable to the minimum in the reflection coefficient and the increased intensity

transmission. As with the fluid medium considered above, it can be readily observed that the energy flux entering the control volume matches the flux exiting, so energy conservation in the solid is verified as well.

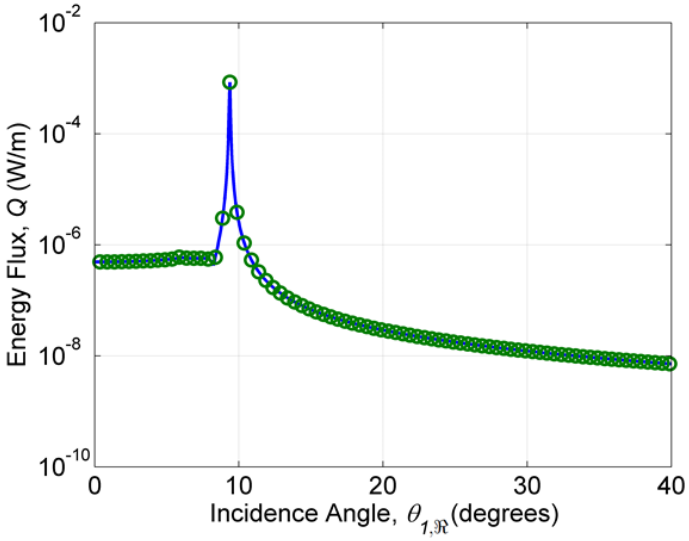

Figure 4.13. The net energy flux per unit width entering and leaving the sample control volume in the solid. The solid line and the markers as circles represent the net energy fluxes entering and leaving the volume, respectively. For visual clarity, the energy flux leaving the volume is shown with data points only at 0.5° increments. Note that a logarithmic scale has been used for the vertical axis.

Figures 4.14 and 4.15 depict the transmitted normal stress, normal particle velocity, and normal intensity distributions for a supercritical angle of $\theta_{1,\Re} = 15°$, with a decay parameter of $\beta = 0.01$ rad/m. The transmitted longitudinal wave propagates at an angle of approximately 89.87°, and the transmitted shear wave propagates at approximately 89.86°, each less than 90°, so permitting energy transmission into the solid medium. The transmitted shear angle is always less than the transmitted longitudinal angle, provided the longitudinal wave speed in the solid is greater than the shear wave speed, and both angles asymptotically approach 90° as the incidence angle is increased towards grazing. Due to the interaction of the transmitted longitudinal and shear waves, the transmitted normal stress peaks at a small distance

(i.e., a fraction of a wavelength) beneath the interface surface. As with the air–water interface, the normal velocity is out-of-phase with the stress, which is evident in the intensity distribution. The lines of constant intensity in the incident wave can again be conceptualized as refracted in the second medium, but due to the contributions from the transmitted shear wave, the interaction in the solid is more complex. The intensity, however, likewise decays with distance into the second medium, at a slight angle with respect to the interface plane, with the angle again exaggerated in Figure 4.15 since the horizontal position range is narrower than the vertical range. Also, as with the air–water case, no dissipation was incorporated in the fluid or solid medium and the spatial decay of the normal intensity is solely a consequence of using incident waves with spatially-dependent pressure amplitudes.

4.4.3 Effects of Frequency, Decay Rate, and Material Properties

The effects of the frequency, incident wave decay rate, and density and wave speed ratios for the air–solid interface were considered as well. For these investigations, the incident wave in air ($\rho_1 = 1.21$ kg/m^3, $v_{1L} = 343$ m/s) is again given a pressure amplitude of $\tilde{p}_0 = 1$ Pa. In addition, except where the parameters are varied, the nominal values are taken as follows: frequency $f = 1000$ Hz, decay parameter $\beta = 0.01$ rad/m, density ratio $\rho_2/\rho_1 = 1000$, longitudinal wave speed ratio $v_{2L}/v_{1L} = 10$, and shear wave speed ratio $v_{2S}/v_{1L} = 7$. For each parameter, three values of the incidence angle were used: $\theta_{1,\Re} = 5°$, $15°$, and $30°$. For all cases, the transmitted normal intensity is presented at the interface (i.e., at $z = 0$) and at the tangential position $x = 0$.

The frequency was varied in the range from $f = 100$ to 1500 Hz. The normal intensity as a function of frequency is presented in Figure 4.16(a). For the subcritical angle of $5°$, the frequency has a negligible effect on the intensity at the interface, with only a slight decrease with increasing frequency, attributable to the decaying component of the incident evanescent wave. However, for all angles, the frequency

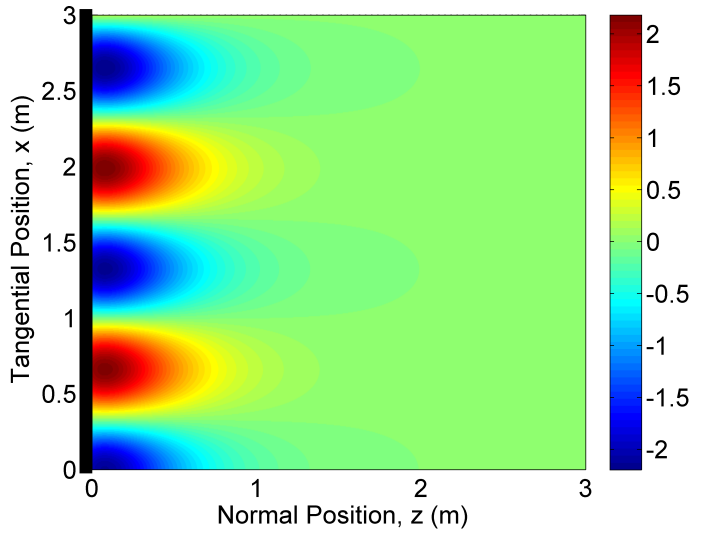

(a)

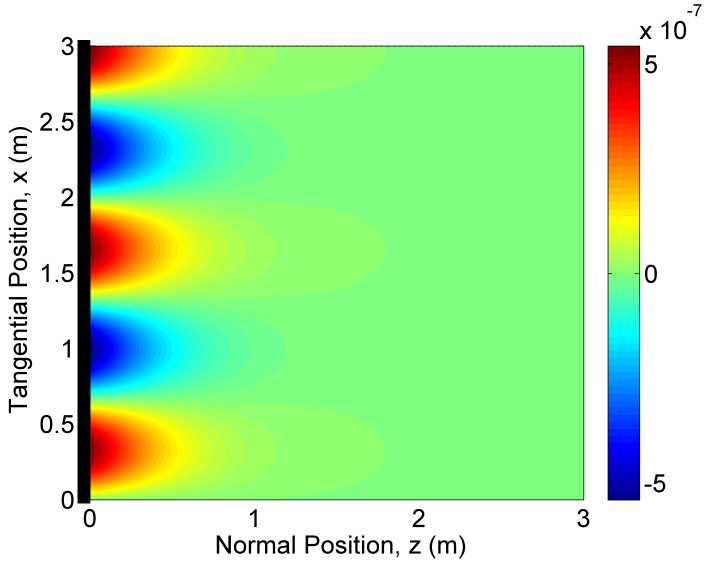

(b)

Figure 4.14. The transmitted distributions of (a) normal stress (in Pa) and (b) normal velocity (in m/s) for the air–solid interface at a supercritical angle of $\theta_{1,\Re} = 15°$. The decay parameter is set to $\beta = 0.01$ rad/m.

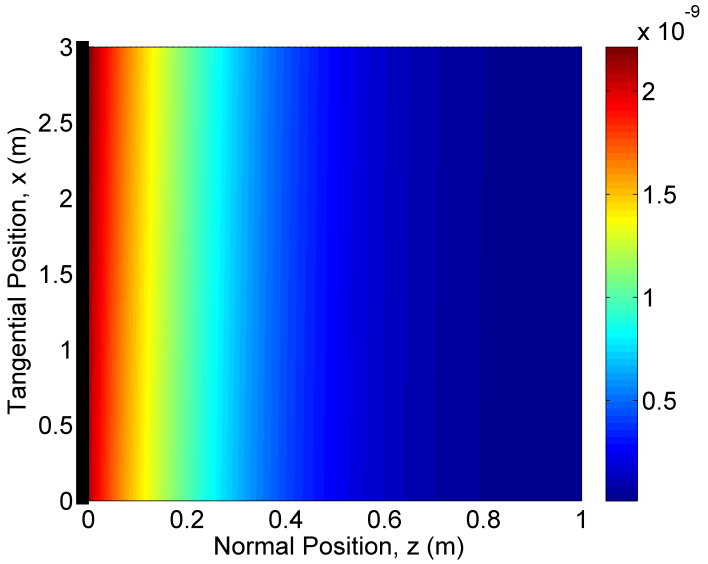

Figure 4.15. The transmitted normal intensity distribution (in W/m^2) for the air–solid interface at a supercritical angle of $\theta_{1,\Re} = 15°$. The decay parameter is set to $\beta = 0.01$ rad/m. Note that the horizontal axis shows the decay over only the first 1 m away from the interface.

significantly impacts the spatial variation in the second medium (with shorter variations and more rapid decay observed at higher frequencies), and affects the incident wave potential amplitude $\tilde{\Phi}_0$, according to its relation with the pressure amplitude ($\tilde{p}_0 = \rho_1 \omega^2 \tilde{\Phi}_0$). For the supercritical angles, the normal intensities can be observed to monotonically decrease with increasing frequencies (since β is held constant and not increased proportionally with the frequency), and to also decrease for increasing incidence angles (since the pressure amplitude is similarly held constant in the variation).

To explore the effect of the decay rate, the decay parameter was chosen to remain small and was varied in the range of $\beta = 10^{-5}$ to 10^{-1} rad/m. The normal intensity as a function of the decay parameter is given in Figure 4.16(b). In a similar way to the frequency, the decay rate has a negligible impact on the intensity at the interface for the subcritical angle, with slight increases for increasing decay rates. At supercritical angles, a larger effect is evident, with dramatic increases in intensity with increasing decay rates, and with intensities again lower for larger incidence angles as the pressure amplitude is held constant. However, when increasing the decay rate of the incident wave, the transmitted waves will decay at a greater rate with distance into the second medium. The transmitted energy is thus increasingly concentrated near the surface for increasing decay rates.

Finally, the effects of the density and wave speed ratios of the interface materials were investigated. The density ratio was varied from $\rho_2/\rho_1 = 10$ to 10^4 to represent a range of typical solid materials, including some high-density solids. Steel and lead, for example, have density ratios of around 6400 and 9300, respectively [78]. By similar considerations, the longitudinal wave speed ratio was varied from $v_{2L}/v_{1L} = 10$ to 20, and the shear wave speed ratio from $v_{2S}/v_{1L} = 5$ to 10, to not exceed the longitudinal ratio. The normal intensities as functions of the density ratio, longitudinal wave speed ratio, and shear wave speed ratio are presented in Figures 4.17, 4.18(a), and 4.18(b), respectively. As the density ratio is increased, the difference in the surface normal impedances of the two media also increases and, therefore, more

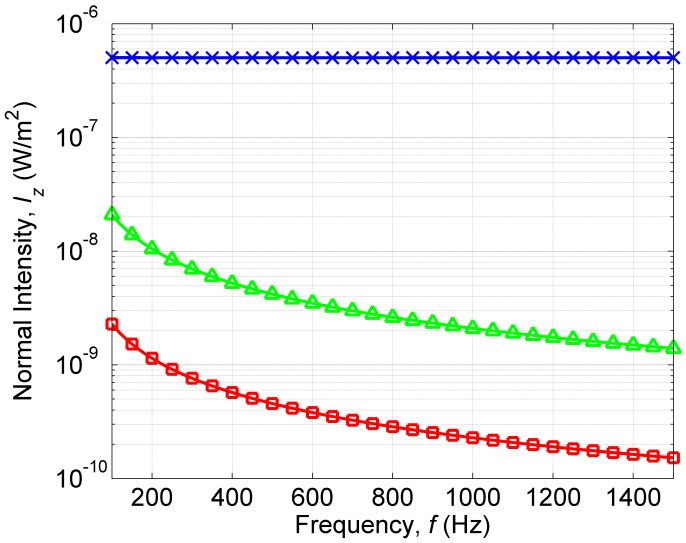

(a)

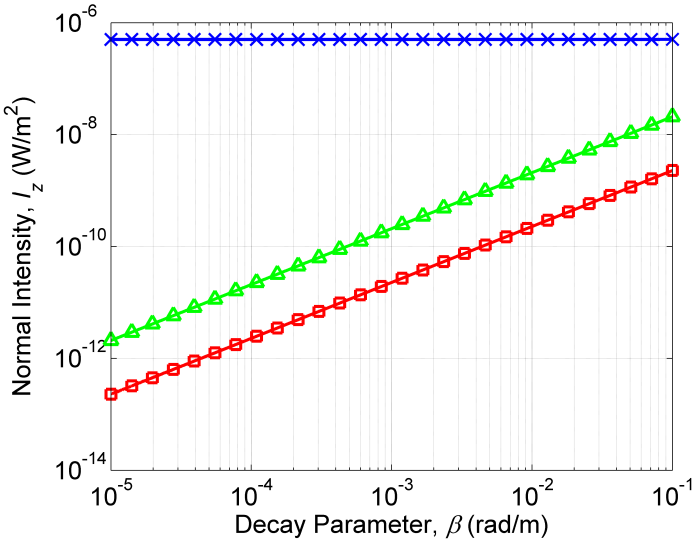

(b)

Figure 4.16. The transmitted normal intensity, at the interface and at tangential position $x = 0$, as a function of the (a) frequency f and (b) decay parameter β. The markers as $\times$'s, triangles, and squares on the curves correspond to values of the incidence angle of $\theta_{1,\Re} = 5°$, 15°, and 30°, respectively. Note that a logarithmic scale has been used for the vertical axes, and for the horizontal axis in (b).

of the intensity is reflected back into the incident medium and less is transmitted. As such, the transmitted normal intensity decreases with increasing density ratio, which is evident in Figure 4.17. Similarly, increasing the longitudinal wave speed ratio yields greater reflection of the incident intensity, and also greater refraction of the transmitted longitudinal waves, which can be observed for the supercritical angles in Figure 4.18(a). In the case of the $\theta_{1,\Re} = 5°$ curve in Figure 4.18(a), the incidence angle is initially subcritical at $v_{2L}/v_{1L} = 10$, but as the wave speed ratio is increased, the angle becomes coincident with the longitudinal critical angle at $v_{2L}/v_{1L} \approx 11.4$ (which corresponds to the local decrease in the curve). Above that value, the angle becomes supercritical for longitudinal waves, but remains subcritical for transverse waves. Consequently, above the coincident value, shear waves dominate in the second medium and the normal intensity increases with further increasing longitudinal wave speed ratios. With respect to the shear wave speed ratio effect in Figure 4.18(b), the variation in the normal intensity is due to the change in the longitudinal wave–shear wave interaction with changes in the shear ratio. The variation for the subcritical angle mirrors that of the supercritical angles, but on a much larger scale. Note that the supercritical angles remain supercritical for both longitudinal and shear waves for all of the shear wave speed values shown. The peaks that are evident for the supercritical angles are due to the minima in the reflection coefficient for the respective incidence angles. The minimum in the reflection coefficient is discussed in the next section.

4.4.4 Conditions for Zero Reflection

In the case of the fluid–solid interface, for a prescribed value of the incident wave decay rate, a minimum in the reflection coefficient can be located at a supercritical angle of incidence. The minimum corresponds to the resonance phenomenon of the coupled longitudinal and shear motions in the solid half-space, which occurs at the Rayleigh angle [97, 101]. In terms of the impedances, the local minimum is the point

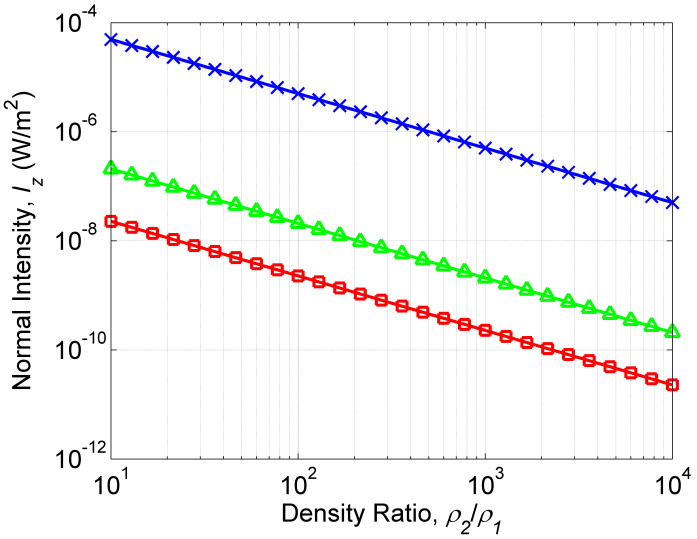

Figure 4.17. The transmitted normal intensity, at the interface and at tangential position $x = 0$, as a function of the density ratio ρ_2/ρ_1. The markers as $\times$'s, triangles, and squares on the curves correspond to values of the incidence angle of $\theta_{1,\Re} = 5°$, $15°$, and $30°$, respectively. Note that a logarithmic scale has been used for the horizontal and vertical axes.

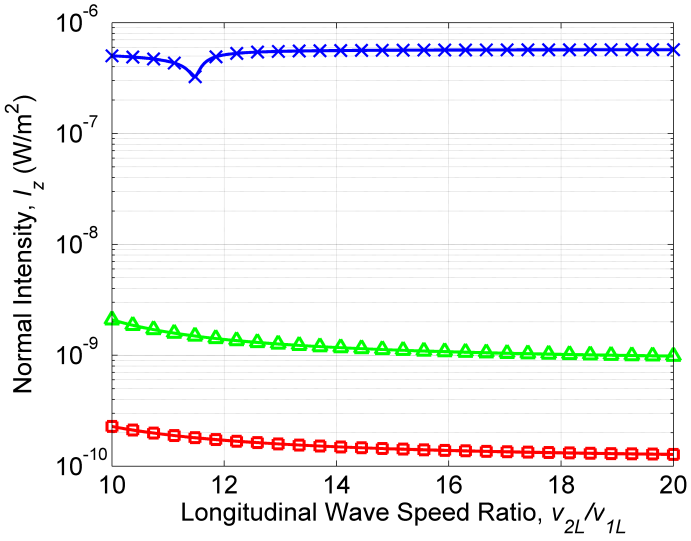

(a)

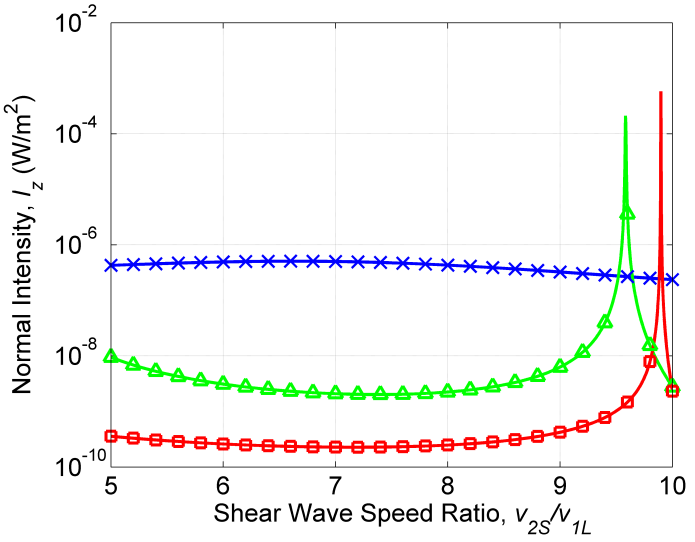

(b)

Figure 4.18. The transmitted normal intensity, at the interface and at tangential position $x = 0$, as a function of the (a) longitudinal wave speed ratio v_{2L}/v_{1L} and (b) shear wave speed ratio v_{2S}/v_{1L}. The markers as $\times$'s, triangles, and squares on the curves correspond to values of the incidence angle of $\theta_{1,\Re} = 5°$, $15°$, and $30°$, respectively. Note that a logarithmic scale has been used for the vertical axes.

at which the surface normal impedance of the incident wave is closely matched by the sum of the impedance contributions from the transmitted longitudinal and shear waves, and, as such, the effect is not observed for the fluid–fluid interface. In fact, for the fluid–solid interface, the decay rate and incidence angle can be varied to locate a set of values for which the reflection coefficient goes to zero (i.e., exact matching of the incident impedance), which depend on the material properties that characterize the two media. The corresponding decay rate and incidence angle values consequently yield total transmission of the incident normal intensity, since none of the incident energy is reflected.

This phenomenon is shown here for the example of the air–solid interface considered in Section 4.4.2. The properties of air are thus again specified as: density $\rho_1 = 1.21$ kg/m^3 and longitudinal wave speed $v_{1L} = 343$ m/s. The properties of the solid medium are likewise again set as: density $\rho_2 = 1210$ kg/m^3 ($\rho_2/\rho_1 = 1000$), longitudinal wave speed $v_{2L} = 3430$ m/s ($v_{2L}/v_{1L} = 10$), and shear wave speed $v_{2S} = 2400$ m/s ($v_{2S}/v_{1L} = 7$). As before, the pressure amplitude of the incident wave is $\tilde{p}_0 = 1$ Pa and the frequency is $f = 1000$ Hz.

The location of the zero in the reflection coefficient $\tilde{R}$ was found numerically through variation of the decay parameter β and the incidence angle $\theta_{1,\Re}$. The values at which the zero occurs are, approximately: $\beta^\star \approx 1.07 \times 10^{-4}$ rad/m and $\theta^\star_{1,\Re} \approx 9.3657°$. The value of the incidence angle is in agreement with the Rayleigh angle, as predicted by Eq. (4.14). The topology of the magnitude of the reflection coefficient in the immediate locale of the zero point is shown in Figure 4.19. It can be observed that the magnitude increases steeply away from the local minimum, as the ranges shown of the input parameters are narrow. However, the reduction of the reflection coefficient across much wider ranges of the angle and decay rate yields significant increases in the intensity transmission in those wider domains, as is evidenced by the region near the peaks in Figure 4.12. Note that, in Figure 4.12, dramatic increases in the intensity are observed even for decay rates that far exceed the value of $\beta^\star$. In addition, sources

creating a band of incidence angles and decay rate components may be used in practice to exploit the phenomenon around the zero point for increased energy transmission.

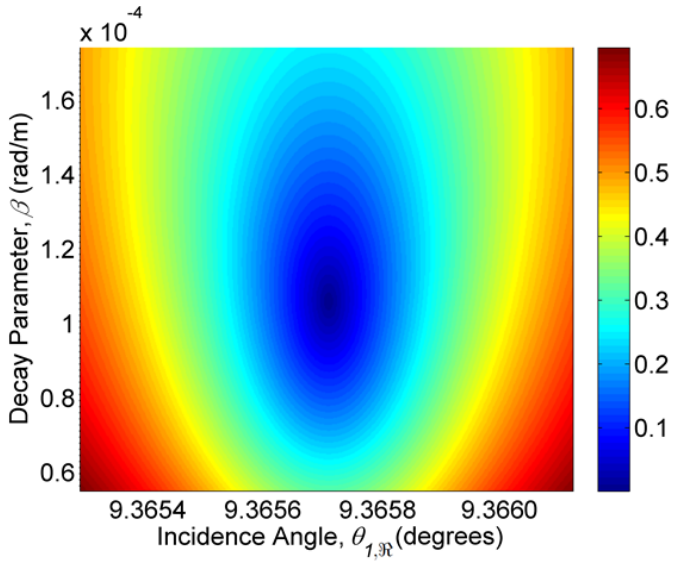

Figure 4.19. The magnitude of the reflection coefficient near the zero point as a function of the incidence angle $\theta_{1,\Re}$ and decay parameter β for the air–solid interface.

Much greater values of the transmitted normal stress, as well as the normal intensity, can be achieved for incidence angles and decay rates near the zero of the reflection coefficient. With reference to Eq. (4.19), at the minimum, the impedance contributions from the transmitted longitudinal and shear waves cancel that of the incident wave to yield a zero in the numerator of $\tilde{R}$. Consequently, the denominator of the transmission coefficients (excluding the density ratio) is $2\tilde{Z}_{1L}$, and the transmitted normal stress terms in Eq. (4.20) are proportional to $\tilde{Z}_{2L}/\tilde{Z}_{1L}$ and $\tilde{Z}_{2S}/\tilde{Z}_{1L}$, which are large ratios for the high impedance-difference. (Note that the density ratio in the coefficient equations cancels with that in the stress equation, and enters in the coefficient equations as a consequence of converting the stress to the wave potential.) The transmitted normal stress, normal particle velocity, and normal intensity distributions are presented in Figures 4.20 and 4.21 for those parameters corresponding to the approximate zero point. In addition to the much greater amplitudes, the peak in

the transmitted stress is shifted a greater distance beneath the interface surface for the case of zero reflection. The transmitted normal intensity near the interface is on the order of 10^{-3} W/m^2, more than 1500 times that transmitted at subcritical angles by homogeneous waves. The zero point corresponds to total intensity transmission, as no reflected wave is generated. Values of the decay rate and incidence angle away from the zero point, as expected, yield less intensity transmission. But, again referring to the peaks observed in Figure 4.12, compared to homogeneous waves, the intensity transmission is increased dramatically across reasonable ranges of the input parameters. In the case of the incident evanescent waves, however, the intensity decays normal to the surface at a rate which increases with the decay parameter β.

4.5 Conclusions

In this chapter, a model for the transmission of evanescent plane waves across idealized fluid–fluid and fluid–solid material interfaces has been presented. For both interfaces, nonzero energy transmission was shown to occur for all oblique angles of incidence, owing to the introduction of a decaying component in the incident wave, which yields a nonzero propagating (real) part of the transmitted normal wavenumber even above the critical angle. Numerical results were presented which demonstrate the phenomena for an air–water interface and for typical air–solid interfaces. The transmitted intensities decay with distance into the media below the interface, attributable to the spatial decay characteristics of the incident and transmitted waves, but the intensities remain nonzero for all such angles of incidence. The rate of decay in the second medium depends on the frequency, angle, and decay rate of the incident wave, as well as on the interface material properties. For the fluid–solid interface, an incidence angle and decay rate could be found for which the reflection coefficient is zero and intensity transmission is maximized, to yield energy transmission on the order of 1500 times that from homogeneous waves at subcritical incidence for the particular interface under consideration. This phenomenon at the Rayleigh angle is

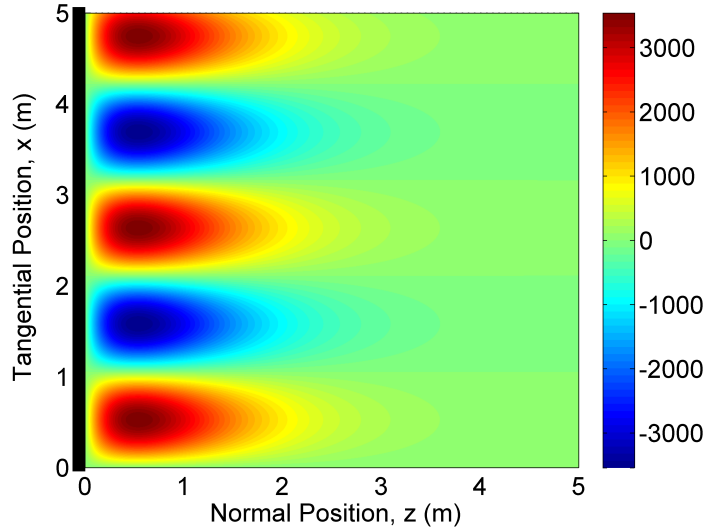

(a)

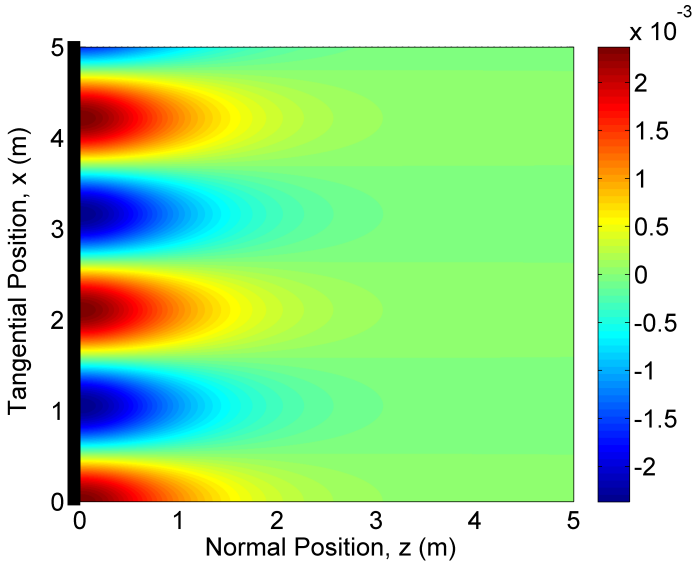

(b)

Figure 4.20. The transmitted distributions of (a) normal stress (in Pa) and (b) normal velocity (in m/s) near the reflection coefficient zero point for the air–solid interface.

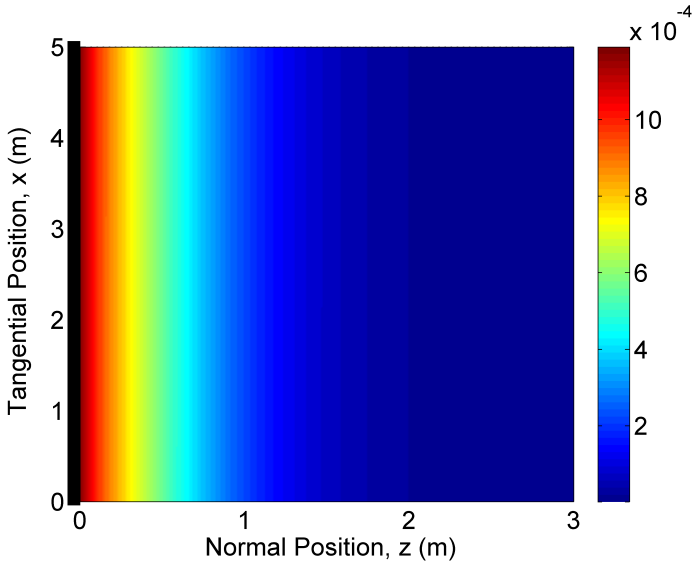

Figure 4.21. The transmitted normal intensity distribution (in W/m^2) near the reflection coefficient zero point for the air–solid interface. Note that the horizontal axis shows the decay over only the first 3 m away from the interface.

attributable to the spatial resonance that occurs when the excitation is coincident with the coupled free wave solution, and the transmitted bulk evanescent waves provide a mechanism for energy propagation beyond the material interface.

The results for the air–solid interface, particularly the zero in the reflection coefficient, suggest that the transmission of incident acoustic energy into target materials for enhanced vapor-based detection capabilities may be significantly improved by tuning the spatial form of the excitation. Moreover, as previously noted, this phenomenon can be exploited for significant transmission increases not only at the zero point, but also in the surrounding neighborhood of incidence angles and decay rates. However, the investigations presented in this chapter for plane waves incident at lossless material interfaces are largely theoretical in nature, as a number of factors are not taken into account which must be considered in practice, including material dissipation and the bounded form of the incident wave. Thus, to provide further insight into the phenomena for real fluid–solid interfaces, Chapter 5 considers the effect of material dissipation, and Chapter 6 considers bounded incident waves.

5. ACOUSTIC ENERGY TRANSMISSION INTO DISSIPATIVE SOLIDS BY INHOMOGENEOUS PLANE WAVES

5.1 Introduction

This chapter extends the discussion in Chapter 4 of incident inhomogeneous plane waves at lossless fluid–solid interfaces to real, or dissipative, fluid–solid interfaces. The incorporation of material dissipation is particularly important in the context of polymer-bonded energetic materials, which generally exhibit appreciable levels of material damping. The aim of this chapter is to uncover the incident plane wave parameters which minimize the reflection coefficient, and consequently maximize the energy transmission, in the presence of material losses, and also to investigate the effect of varying solid dissipation levels. In a similar investigation, for dissipative media and with incident homogeneous plane waves, Becker and Richardson [171, 172] considered arbitrary variation of the shear attenuation coefficient for a water–stainless steel interface, including the variation with frequency, and found that significantly lower values of the reflection coefficient were predicted for certain values of the shear attenuation. In this chapter, rather than varying the frequency, the degree of inhomogeneity of the incident wave will be tuned for the purpose of minimizing the reflection coefficient.

The types of inhomogeneous plane waves which may propagate in dissipative media differ from those which may propagate in lossless media. In analog with Figure 4.1 for lossless media, Figure 5.1 shows conceptually the pressure fields (or stress fields in a solid) of homogeneous and inhomogeneous plane waves in a linear viscoelastic medium. For the homogeneous plane wave in Figure 5.1(a), there is a nonzero component of amplitude decay along the direction of propagation (left-to-right in Figure 5.1), due to the presence of material dissipation. For the inhomogeneous plane wave

in Figure 5.1(b), there are components of decay both along that propagation direction (due to material damping) and perpendicular to that direction (due to the nonzero degree of inhomogeneity). Similar to the investigation in Chapter 4, tuning the incident wave parameters to maximize the energy transmission into solid media in this case thus requires varying the degree of inhomogeneity, which is further discussed below.

In order to incorporate the material losses in the incident wave parameter variation, an interface model which allows for both inhomogeneous and homogeneous incident plane waves and arbitrary levels of material dissipation is developed in this chapter, which is based on the theory presented by Borcherdt [66] for linear viscoelastic media. It should be noted that this viscoelastic model, also used in Chapter 6, is the same as that which was employed in Chapters 2 and 3 in relation to the heat generation. This portion of the work thus serves to inform the optimal incident waveform for excitation under the same material assumptions. Specifically, numerical results for the reflection coefficient with inhomogeneous incident waves are presented in this chapter for a low-loss solid interface, and also with the solid dissipation level varied. The results reveal that near-zero values of the reflection coefficient can be achieved near the Rayleigh angle by varying the degree of inhomogeneity, provided the losses in the solid are sufficiently small, a result analogous to that for lossless media. However, above a certain threshold of the solid dissipation level, no local minimum in reflection can be found and homogeneous plane waves yield lower reflection values than inhomogeneous waves. Analytical conditions related to this critical level of dissipation are derived by using approximations for low-loss media. Major portions of this chapter first appeared in the Proceedings of the 12th International Conference on Recent Advances in Structural Dynamics [173], and were subsequently published in the Journal of Physics: Conference Series [174].

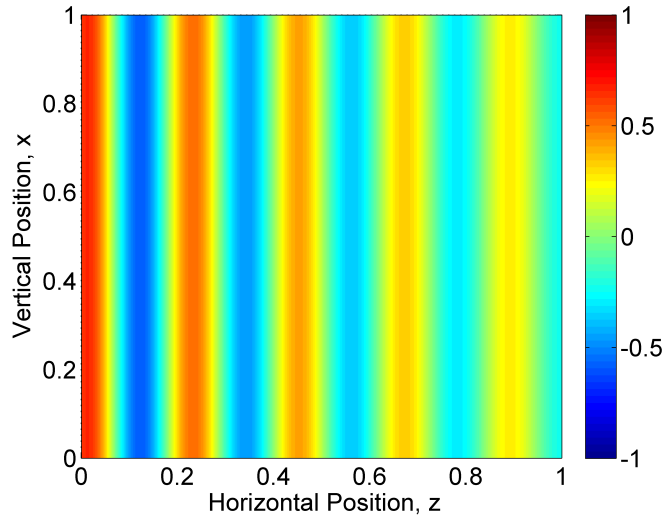

(a)

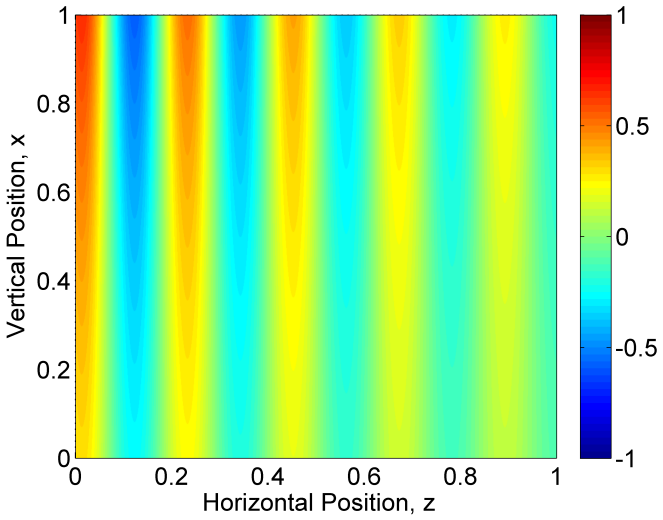

(b)

Figure 5.1. The pressure field, shown conceptually, of a plane wave propagating in a dissipative (linear viscoelastic) medium with the wave as (a) homogeneous and (b) inhomogeneous. Arbitrary scalings are used for the purpose of illustration.

5.2 Representation of Inhomogeneous Plane Waves in Dissipative Media

When assuming a hysteretic damping (i.e., viscoelastic) model, monochromatic wave propagation in homogeneous, isotropic, linear media may be characterized by the complex material wavenumbers for longitudinal and shear waves, $\tilde{k}_L$ and $\tilde{k}_S$, respectively:

$$\begin{aligned} \tilde{k}_L &= \frac{\omega}{v_L} - j\alpha_L, \\ \tilde{k}_S &= \frac{\omega}{v_S} - j\alpha_S, \end{aligned} \tag{5.1}$$

where ω is the frequency of the wave, v_L and v_S are the respective wave speeds for homogeneous waves, α_L and α_S are the respective attenuation coefficients, and the time dependence is assumed to be $e^{j\omega t}$. With a knowledge of the complex wavenumbers and the density ρ, the material is completely characterized through the relations for linear viscoelastic media [66]. If the complex Lamé parameters are used as the two material moduli, then the first parameter is given by $\tilde{\lambda} = \rho\omega^2(1/\tilde{k}_L^2 - 2/\tilde{k}_S^2)$, and the second parameter by $\tilde{\mu} = \rho\omega^2/\tilde{k}_S^2$. For the frequency-dependence of the wavenumbers, a power law is generally assumed for the attenuation coefficients, which is dependent on the material under consideration, and the variation of the wave speeds is typically much weaker [175].

For homogeneous plane waves, only the frequency, amplitude, and propagation angle with respect to a given coordinate system must be specified to characterize the wave, since the directions of phase propagation and amplitude attenuation are aligned. However, for inhomogeneous plane waves, the degree of inhomogeneity must be additionally specified. Figure 5.2(a) shows a generic diagram of the propagation vector $\vec{P}_i$, attenuation vector $\vec{A}_i$, and degree of inhomogeneity γ_i for an inhomogeneous plane wave propagating in the xz-plane, where, for the sake of generality, the subscript $i = L, S$ indicates the wave type as longitudinal or shear. It follows from the Helmholtz equation that the complex wavevector for either type of wave, $\tilde{\vec{K}}_i = \vec{P}_i - j\vec{A}_i$, must satisfy the material wavenumber condition [66]:

$$\tilde{\vec{K}}_i \cdot \tilde{\vec{K}}_i = \tilde{k}_i^2. \tag{5.2}$$

In turn, it follows from this relation that when $\alpha_i \neq 0$, the degree of inhomogeneity ($0^\circ \leq \gamma_i < 90^\circ$) is related to the magnitudes of the propagation and attenuation vectors according to:

$$\begin{aligned} |\vec{P}_i|^2 &= \frac{1}{2}\left(\mathrm{Re}[\tilde{k}_i^2] + \sqrt{(\mathrm{Re}[\tilde{k}_i^2])^2 + \frac{(\mathrm{Im}[\tilde{k}_i^2])^2}{\cos^2(\gamma_i)}}\right), \\ |\vec{A}_i|^2 &= \frac{1}{2}\left(-\mathrm{Re}[\tilde{k}_i^2] + \sqrt{(\mathrm{Re}[\tilde{k}_i^2])^2 + \frac{(\mathrm{Im}[\tilde{k}_i^2])^2}{\cos^2(\gamma_i)}}\right), \end{aligned} \tag{5.3}$$

where Re denotes the real part of the argument and Im the imaginary part. It should be emphasized here that the degree of inhomogeneity, if nonzero, thus impacts both the effective phase speed $\omega/|\vec{P}_i|$, which is lower than that for homogeneous waves v_i, and the effective attenuation $|\vec{A}_i|$, which exceeds that for homogeneous waves α_i.

Finally, the wave potentials also follow from the solution to the Helmholtz equation which, for longitudinal and shear waves, respectively, are given by [66]:

$$\begin{aligned} \tilde{\Phi} &= \tilde{\Phi}_0 \exp[-\vec{A}_L \cdot \vec{r}] \exp[j(\omega t - \vec{P}_L \cdot \vec{r})], \\ \tilde{\vec{\Psi}} &= \tilde{\vec{\Psi}}_0 \exp[-\vec{A}_S \cdot \vec{r}] \exp[j(\omega t - \vec{P}_S \cdot \vec{r})], \end{aligned} \tag{5.4}$$

where $\vec{r}$ is the position vector, and $\tilde{\Phi}_0$ and $\tilde{\vec{\Psi}}_0$ are the amplitudes of the potentials. It should also be noted here that, in the case of lossless media (i.e., $\alpha_i = 0$), the degree of inhomogeneity γ_i must be either 0° (for a homogeneous plane wave) or 90° (for an inhomogeneous plane wave), since there is never a component of decay along the propagation direction (see Chapter 4). In contrast, for dissipative media as investigated in this chapter, there is always a component of decay along the propagation direction due to material losses, which results in the condition $0^\circ \leq \gamma_i < 90^\circ$.

5.3 Fluid–Solid Interface

The reflection and transmission coefficients, as well as the stresses and energy fluxes, are developed here for a semi-infinite material interface between fluid and solid media. As in the preceding section, both media are assumed to be homogeneous,

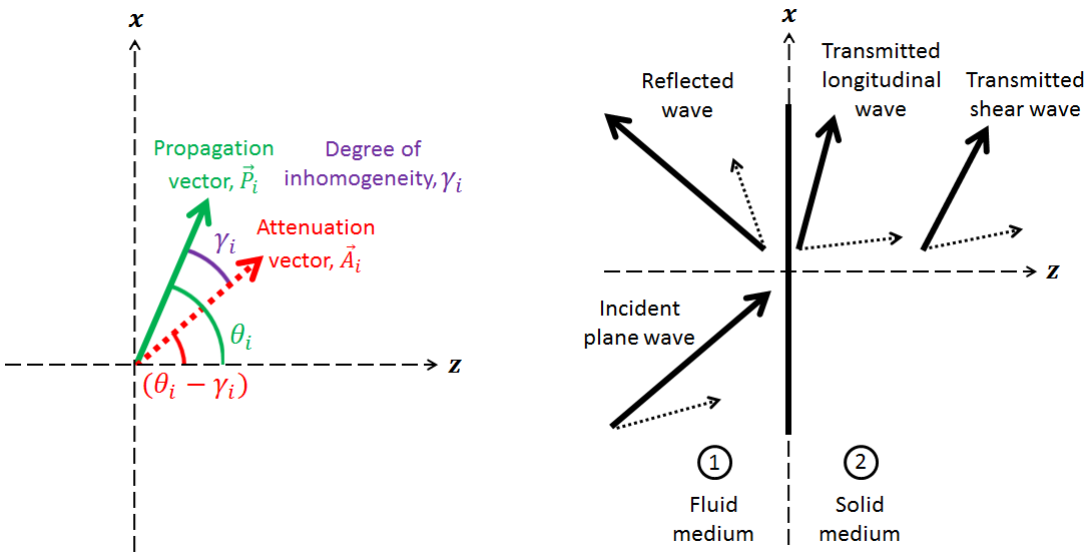

(a) (b)

Figure 5.2. A diagram showing (a) the propagation and attenuation vectors for an inhomogeneous plane wave propagating in the xz-plane (where the subscript $i = L, S$ indicates the wave type as longitudinal or shear), and (b) the reflected and transmitted waves at the fluid–solid interface for an incident inhomogeneous plane wave. Propagation vectors are shown as solid lines, and attenuation vectors as dotted lines.

isotropic, and linear, and to have an associated hysteretic damping model. The incident wave is taken to be a longitudinal plane wave in the fluid, which may be either homogeneous or inhomogeneous. The interface is shown conceptually in Figure 5.2(b), where a right-handed, rectangular coordinate system is assumed. As in Chapter 4, to denote whether quantities apply in the fluid or solid medium, a preceding subscript 1 will be used for the fluid medium, and a subscript 2 will be used for the solid (e.g., $\tilde{k}_{1L}$ will denote the material wavenumber for longitudinal waves in the fluid, and $\tilde{k}_{2L}$ will denote that in the solid).

The boundary conditions at the interface (i.e., at $z = 0$) require continuity of the stress and particle displacement normal to the interface, and also continuity of the shear stress [66, 77]. It is straightforward to compute the particle displacement in

either medium m from the wave potentials: $\tilde{\vec{u}}_m = \nabla\tilde{\Phi}_m + \nabla \times \tilde{\vec{\Psi}}_m$. For propagation in the xz-plane, the normal and in-plane shear stresses can be computed, respectively, in either medium as:

$$\begin{aligned} \tilde{\sigma}_{m,zz} &= \tilde{\lambda}_m \left(\frac{\partial \tilde{u}_{m,x}}{\partial x} + \frac{\partial \tilde{u}_{m,z}}{\partial z} \right) + 2\tilde{\mu}_m \left(\frac{\partial \tilde{u}_{m,z}}{\partial z} \right), \\ \tilde{\sigma}_{m,xz} &= \tilde{\mu}_m \left(\frac{\partial \tilde{u}_{m,x}}{\partial z} + \frac{\partial \tilde{u}_{m,z}}{\partial x} \right), \end{aligned} \tag{5.5}$$

where the subscript on the right-hand side after the comma again denotes the component of the vector. It is assumed here that the fluid medium does not sustain shear waves (i.e., $\tilde{\mu}_1 = 0$, $\tilde{\vec{\Psi}}_1 = 0$), so the displacement and stress equations simplify considerably in the fluid. As a consequence of the shear stress continuity, the shear stress at the surface of the solid is thus equal to zero in this case.

The reflection and transmission coefficients are computed by application of the aforementioned boundary conditions. Trace wavenumber continuity, or the generalized Snell's law, subsequently follows: $\tilde{k}_{1L,x} = \tilde{k}_{2L,x} = \tilde{k}_{2S,x}$. Therefore, $\tilde{k}_x$ can be simply written here without ambiguity. The z-components of the transmitted wavevectors are then computed from the material wavenumber condition, Eq. (5.2), by using the principal value of the square root [66]: $\tilde{k}_{2L,z} = (\tilde{k}_{2L}^2 - \tilde{k}_x^2)^{1/2}$ and $\tilde{k}_{2S,z} = (\tilde{k}_{2S}^2 - \tilde{k}_x^2)^{1/2}$. Finally, the three boundary conditions yield the linear system that can be solved for the reflection and transmission coefficients:

$$\begin{bmatrix} \tilde{k}_{1L,z} & \tilde{k}_{2L,z} & \tilde{k}_x \\ -\tilde{\lambda}_1\tilde{k}_{1L}^2 & \tilde{\lambda}_2\tilde{k}_{2L}^2 + 2\tilde{\mu}_2\tilde{k}_{2L,z}^2 & 2\tilde{\mu}_2\tilde{k}_x\tilde{k}_{2S,z} \\ 0 & 2\tilde{\mu}_2\tilde{k}_x\tilde{k}_{2L,z} & \tilde{\mu}_2(\tilde{k}_x^2 - \tilde{k}_{2S,z}^2) \end{bmatrix} \begin{bmatrix} \tilde{R} \\ \tilde{\mathcal{T}}_L \\ \tilde{\mathcal{T}}_S \end{bmatrix} = \begin{bmatrix} \tilde{k}_{1L,z} \\ \tilde{\lambda}_1\tilde{k}_{1L}^2 \\ 0 \end{bmatrix}, \tag{5.6}$$

where $\tilde{R}$ is the (longitudinal) reflection coefficient, and $\tilde{\mathcal{T}}_L$ and $\tilde{\mathcal{T}}_S$ are the transmission coefficients for the transmitted longitudinal and shear waves, respectively, in terms of the wave potentials.

It is then straightforward to compute the stresses in either medium by using Eq. (5.5). The instantaneous energy flux vector in the dissipative media [66, 102, 170]

can be written, like the expression given for the lossless media in Chapter 4, in terms of the stress tensor $\tilde{\sigma}_{m,ln}$ and particle velocity vector $\partial\tilde{\vec{u}}_m/\partial t$:

$$\mathcal{E}_n(t) = -\left(\mathrm{Re}\left[\tilde{\sigma}_{m,xn}\right]\mathrm{Re}\left[\frac{\partial\tilde{u}_{m,x}}{\partial t}\right] + \mathrm{Re}\left[\tilde{\sigma}_{m,zn}\right]\mathrm{Re}\left[\frac{\partial\tilde{u}_{m,z}}{\partial t}\right]\right), \tag{5.7}$$

for $n = x, z$. The average energy flux, or intensity, is then computed by time-averaging the instantaneous flux over one period, as in Eq. (4.23).

5.3.1 Minimization of the Reflection Coefficient

In order to maximize the energy transmitted across the fluid–solid interface, the reflection coefficient should be minimized. Provided that the density and Rayleigh wave speed in the solid exceed the density and longitudinal wave speed, respectively, in the fluid, it is well-known that transmission is optimized when incidence is at the Rayleigh angle for the interface, at which point the incident wave is coincident with the free wave solution of resonant longitudinal and shear motions on the solid surface [111, 112, 169]. The degree of inhomogeneity of the incident wave also affects the energy transmission, and the optimal value of the inhomogeneity depends on the dissipation levels in the solid, as well as on the other parameters which characterize the interface.

The wavenumber $\tilde{k}_{Ray}$ for the Rayleigh-type surface wave on a linear viscoelastic half-space can be numerically computed as for a lossless elastic half-space, but with the complex values for the longitudinal and shear material wavenumbers inserted into the characteristic equation [66]:

$$\left(\frac{\tilde{k}_{2S}^2}{\tilde{k}_{Ray}^2}\right)^3 - 8\left(\frac{\tilde{k}_{2S}^2}{\tilde{k}_{Ray}^2}\right)^2 + \left(24 - 16\frac{\tilde{k}_{2L}^2}{\tilde{k}_{2S}^2}\right)\left(\frac{\tilde{k}_{2S}^2}{\tilde{k}_{Ray}^2}\right) - 16\left(1 - \frac{\tilde{k}_{2L}^2}{\tilde{k}_{2S}^2}\right) = 0, \tag{5.8}$$

where the solution is the root such that $|\tilde{k}_{2S}^2/\tilde{k}_{Ray}^2| < 1$. The complex wave speed $\tilde{v}_{Ray}$ of the Rayleigh-type wave is then $\tilde{v}_{Ray} = \omega/\tilde{k}_{Ray}$, and the Rayleigh angle for the fluid–solid interface is $\theta_{Ray} = \arcsin(v_{1L}/\mathrm{Re}[\tilde{v}_{Ray}])$, where v_{1L} is the wave speed for homogeneous longitudinal waves in the fluid medium. For low-loss solids, the effect

of material dissipation on the Rayleigh wave speed is negligible, and the wave speed can be approximated as: $\tilde{v}_{Ray} \approx \mathrm{Re}[\tilde{v}_{Ray}] \equiv v_{Ray}$.

With respect to the degree of inhomogeneity γ_{1L} of the incident wave which minimizes the reflection coefficient, analysis reveals a strong dependence on the dissipation levels in the solid medium. For the lossless fluid–solid interface, it was shown that, with incidence at the Rayleigh angle, a unique value of the inhomogeneity yields a zero of the reflection coefficient magnitude (see Chapter 4). For the dissipative fluid–solid interface under consideration here, a unique value for the degree of inhomogeneity can likewise be found which yields a local minimum of the reflection coefficient if the dissipation levels in the solid are sufficiently small. The value of the reflection coefficient magnitude there is typically near-zero, but remains nonzero due to the material dissipation in the system.

However, above a critical level of dissipation in the solid, homogeneous incident waves yield lower values of the reflection coefficient at the Rayleigh angle than do inhomogeneous incident waves, regardless of the value of the degree of inhomogeneity. This is due to the fact that, with sufficient dissipation levels in the solid, the transmitted waves inherently have a high degree of inhomogeneity, even for homogeneous incident waves, and so there is no benefit to introducing an additional level of inhomogeneity through an inhomogeneous incident wave. Therefore, the reflection coefficient is minimized for a homogeneous incident wave, but the value is neither a local minimum nor typically near-zero (see also Section 5.4.2).

An approximation for the critical value of solid dissipation below which inhomogeneous incident waves improve energy transmission can be derived by assuming small losses in the solid and negligible losses in the fluid. The derivation is given in Section 5.3.2. The ratio of the longitudinal attenuation coefficient in the solid to the shear attenuation coefficient was held constant in the variation: $\alpha_{ratio} = \alpha_{2L}/\alpha_{2S} = \text{constant}$. The result for the approximation, in terms of the shear attenuation coefficient, is:

$$\alpha_{2S}^{\star} \approx \frac{1}{4}\left(\frac{\rho_1 v_{1L}}{\rho_2 v_{2S}}\right)\left(\frac{v_{Ray}}{\sqrt{v_{Ray}^2 - v_{1L}^2}}\right)\frac{\omega}{V}, \tag{5.9}$$

where the quantity V is a function of only the wave speeds and attenuation ratio in the solid and is given by Eq. (5.15). The first term in parentheses is the ratio of the longitudinal wave impedance in the fluid to the shear wave impedance in the solid, and the second term accounts for the effect of the incident medium (fluid) on the transmitted waves when incidence is at the Rayleigh angle. If a power law is assumed for the frequency variation of the attenuation coefficient, $\alpha_{2S} = a_\alpha \omega^{b_\alpha}$, then the condition can instead be framed in terms of the frequency:

$$\omega^\star \approx \left[\frac{1}{4 a_\alpha V} \left(\frac{\rho_1 v_{1L}}{\rho_2 v_{2S}} \right) \left(\frac{v_{Ray}}{\sqrt{v_{Ray}^2 - v_{1L}^2}} \right) \right]^{1/(b_\alpha - 1)} . \tag{5.10}$$

Thus, for a homogeneous incident wave and set material parameters (except for the frequency-dependence of the attenuation), a frequency can be found which yields a minimum of the reflection coefficient, a conclusion which is supported by the investigations of Becker and Richardson [171, 172]. However, since the present work is focused on the extension to inhomogeneous incident waves, the frequency will be held constant.

5.3.2 Derivation of the Critical Value of Solid Dissipation below which Inhomogeneous Waves Minimize Reflection

An approximation for the critical value of the shear attenuation coefficient below which inhomogeneous incident plane waves improve the energy transmission at the Rayleigh angle is derived here. Since the degree of inhomogeneity of the incident wave which minimizes the reflection coefficient magnitude is zero in the right-hand limit at the critical value of attenuation (see also Section 5.4.2), the system in Eq. (5.6) can be analyzed to minimize $\tilde{R}$ for a homogeneous incident wave.

In order to simplify the system, the losses in the fluid are assumed to be negligible compared to the real part of the incident wavevector and compared to the losses in the solid: $\alpha_{1L} \ll \omega/v_{Ray}$ and $\alpha_{1L} \ll \alpha_{2L}, \alpha_{2S}$. These conditions yield, for the fluid:

$$\tilde{\lambda}_1 \approx \rho_1 v_{1L}^2, \quad \tilde{k}_x \approx \frac{\omega}{v_{Ray}}, \quad \tilde{k}_{1L,z} \approx \frac{\omega\sqrt{v_{Ray}^2 - v_{1L}^2}}{v_{Ray} v_{1L}}. \tag{5.11}$$

In the solid, the losses are assumed to be small in the sense that the squares of the attenuation coefficients are negligible in comparison to those of the real parts of the material wavenumbers: $\alpha_{2L}^2, \alpha_{2S}^2 \ll (\omega/v_{2L})^2, (\omega/v_{2S})^2$. Thus, the imaginary part of the complex Rayleigh-type wave speed can be neglected and the real part v_{Ray} is sufficient. The imaginary part of the first Lamé parameter is also neglected here for the purpose of stress computations, since the effects of the longitudinal and shear attenuation coefficients partially offset each other for the first Lamé parameter. Consequently, for the solid:

$$\tilde{\lambda}_2 \approx \rho_2 \left(v_{2L}^2 - 2v_{2S}^2\right), \quad \tilde{\mu}_2 \approx \rho_2 v_{2S}^2 \left(1 + \frac{2j v_{2S}\alpha_{2S}}{\omega}\right). \tag{5.12}$$

The z-components of the transmitted wavevectors are computed by using the principal value of the square root, and must also be approximated here. This approximation can be made by using the assumptions listed above, the material wavenumber condition in Eq. (5.2), and the observation that the magnitudes of the real part of the z-components are small for supercritical incidence at the Rayleigh angle (i.e., $|\mathrm{Re}[\tilde{k}_{2L,z}]| \ll |\mathrm{Im}[\tilde{k}_{2L,z}]|$ and $|\mathrm{Re}[\tilde{k}_{2S,z}]| \ll |\mathrm{Im}[\tilde{k}_{2S,z}]|$). The real and imaginary parts of the resulting equation then yield the approximations for the real and imaginary parts of the z-components of the transmitted wavevectors:

$$\begin{aligned} \tilde{k}_{2L,z} &\approx \frac{\alpha_{2L}}{v_{2L}\sqrt{v_{Ray}^{-2} - v_{2L}^{-2}}} - j\omega\sqrt{v_{Ray}^{-2} - v_{2L}^{-2}}, \\ \tilde{k}_{2S,z} &\approx \frac{\alpha_{2S}}{v_{2S}\sqrt{v_{Ray}^{-2} - v_{2S}^{-2}}} - j\omega\sqrt{v_{Ray}^{-2} - v_{2S}^{-2}}. \end{aligned} \tag{5.13}$$

The substitution of the above approximations into Eq. (5.6) yields an approximation to the system in terms of only the frequency ω and the material parameters

sufficient to characterize the two media under the assumptions used (ρ_1, ρ_2, v_{1L}, v_{2L}, v_{2S}, α_{2L}, α_{2S}, and, as computed from the relations highlighted in Section 5.3.1, v_{Ray}). Finally, the ratio of the longitudinal attenuation coefficient in the solid to the shear attenuation coefficient is held constant in the variation: $\alpha_{ratio} = \alpha_{2L}/\alpha_{2S} = \text{constant}$. The system can then be solved by row reduction and, given the assumptions used here, terms of order $(\alpha_{2S})^2$ or higher can be neglected.

The minimum of the reflection coefficient magnitude with respect to the attenuation occurs when the real part of the reflection coefficient is zero. Thus, setting that part equal to zero yields the approximation presented in Eq. (5.9) for the critical value of the shear attenuation coefficient:

$$\alpha_{2S}^{\star} \approx \frac{1}{4}\left(\frac{\rho_1 v_{1L}}{\rho_2 v_{2S}}\right)\left(\frac{v_{Ray}}{\sqrt{v_{Ray}^2 - v_{1L}^2}}\right)\frac{\omega}{V}, \tag{5.14}$$

where the quantity V (with units of velocity) is a function of only the wave speeds and attenuation ratio in the solid and is given by:

$$\begin{aligned} V(v_{2L}, v_{2S}, v_{Ray}, \alpha_{ratio}) = \varphi_S \left[v_{2S}^2 v_{Ray}^{-2}(1 + 2v_{2S}^2\varphi_S^{-2})\right] \\ - \varphi_L\big[v_{2S}^2\varphi_L^{-2} + v_{2L}^{-2}(v_{2S}^2 - v_{2L}^2/2) \\ + v_{2S}^3(v_{Ray}^{-2} + \varphi_S^{-2})(v_{2S}\varphi_L^{-2} + v_{2L}^{-1}\alpha_{ratio})\big], \end{aligned} \tag{5.15}$$

for which the quantities $\varphi_L = (v_{Ray}^{-2} - v_{2L}^{-2})^{-1/2}$ and $\varphi_S = (v_{Ray}^{-2} - v_{2S}^{-2})^{-1/2}$ have been introduced for the sake of convenience.

5.4 Numerical Results and Discussion

For the purpose of illustrating the effect of the degree of inhomogeneity of the incident plane wave on the reflection coefficient and transmitted intensity, a high-frequency water–stainless steel interface is considered here, with the incidence angle near the Rayleigh angle for the interface. Additionally, simultaneous variation of the inhomogeneity of the incident wave and the solid dissipation level is considered, and the exact results for the critical value of dissipation are directly compared with those

predicted by the approximation in Eq. (5.9). Since shear waves in the fluid medium are neglected, the incidence angle and degree of inhomogeneity of the incident wave can be simply written as θ_1 and γ_1, respectively, omitting the subscript L, without ambiguity. It should also be noted here that, as in Chapter 4, the boundary conditions at the interface, as well as the continuity of the energy flux normal to the interface, were verified for each parameter variation considered.

5.4.1 Low-loss Solid Interface: Water–Stainless Steel

For the water–stainless steel interface at a frequency of 10 MHz, the material properties were taken as those used by Borcherdt [66]: for water, $\rho_1 = 1000$ kg/m^3, $v_{1L} = 1490$ m/s, and $\alpha_{1L} = 2.530$ rad/m; and for stainless steel, $\rho_2 = 7932$ kg/m^3, $v_{2L} = 5740$ m/s, $v_{2S} = 3142$ m/s, $\alpha_{2L} = 39.95$ rad/m, and $\alpha_{2S} = 127.0$ rad/m. The Rayleigh wave speed, from the equations presented in Section 5.3.1, is $v_{Ray} \approx 2907$ m/s (where the imaginary part is negligible), and the Rayleigh angle is $\theta_{Ray} \approx 30.833°$.

Figure 5.3(a) shows the magnitude of the reflection coefficient as the incidence angle θ_1 is varied near the Rayleigh angle and the degree of inhomogeneity γ_1 is varied from 0° (homogeneous wave) to values near 90°. As is evident, with respect to the variation of the incidence angle, the lowest values of the reflection coefficient are achieved at the Rayleigh angle. More importantly, with incidence at the Rayleigh angle, the variation of the degree of inhomogeneity is observed to yield near-zero reflection values, and hence near-perfect energy transmission into the solid. The degree of inhomogeneity which yields the local minimum is $\gamma_1 \approx 88.85°$. This phenomenon is illustrated in Figure 5.3(b), where only the degree of inhomogeneity is varied, and the incidence angle is held constant at the Rayleigh angle. The value of the reflection coefficient at the local minimum is $|\tilde{R}| \approx 0.0203$, which represents a significant reduction from the value of $|\tilde{R}| \approx 0.295$ for homogeneous incident waves.

In order to illustrate the corresponding effect on the transmitted energy flux, Figure 5.4 presents the transmitted normal intensity I_z at the interface (i.e., at $z = 0$)

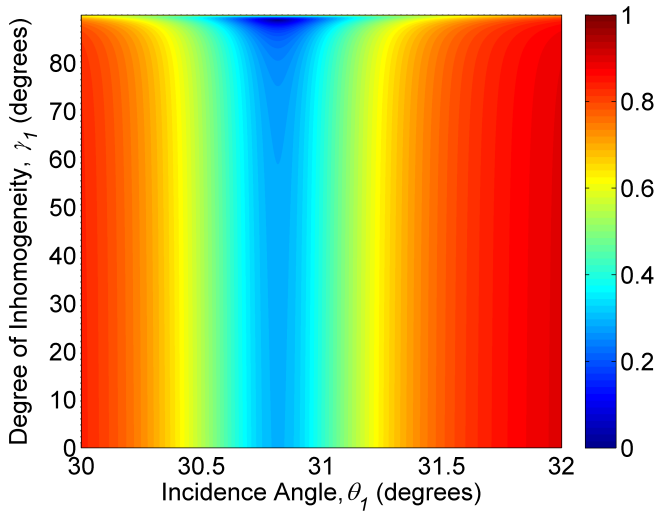

(a)

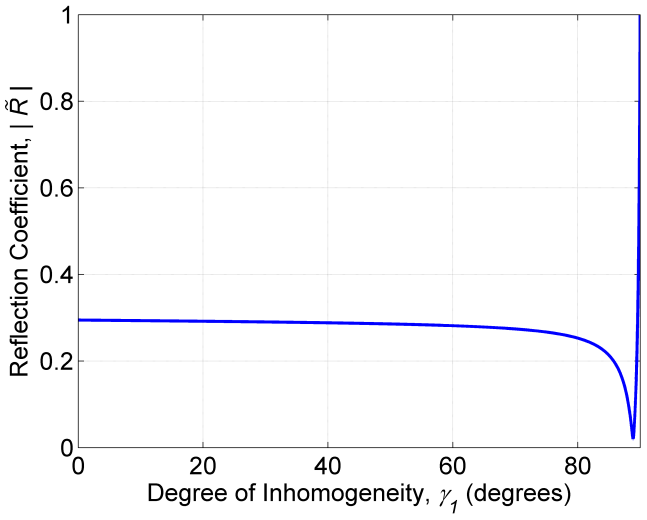

(b)

Figure 5.3. The magnitude of the reflection coefficient for the water–stainless steel interface at 10 MHz as a function of (a) incidence angle θ_1 and degree of inhomogeneity γ_1 of the incident wave, and (b) degree of inhomogeneity γ_1 of the incident wave at the Rayleigh angle $\theta_1 = \theta_{Ray} \approx 30.833°$.

and at the tangential position $x = 0$ as a function of the degree of inhomogeneity γ_1, with incidence again at the Rayleigh angle. The amplitude of the incident wave was

set as 1 Pa at $x = z = 0$, as for the analogous cases presented in Chapter 4 for lossless media. As is evident in Figure 5.4(a), the variation of the transmitted intensity with the inhomogeneity largely mirrors that of the reflection coefficient shown in Figure 5.3(b). However, the variation exhibited in the energy flux is somewhat smoother than that of the reflection coefficient, particularly near the local maximum in transmission. A close-up view near the local maximum at $\gamma_1 \approx 88.85°$, which corresponds to the location of the local minimum in reflection, is shown in Figure 5.4(b).

5.4.2 Variation of the Solid Dissipation Level and Incident Wave Inhomogeneity

Though a unique value of the degree of inhomogeneity of the incident wave can be found for low-loss solid interfaces to yield a local minimum of the reflection coefficient at the Rayleigh angle, no such value can be found if dissipation levels in the solid are above a critical level. Since the transmitted waves in such higher-loss solids inherently have considerable degrees of inhomogeneity when incidence is at the Rayleigh angle, no additional benefit is conferred by making the incident wave inhomogeneous. In order to illustrate this effect, the properties of the interface considered in Section 5.4.1 were used, except that the attenuation coefficients in the solid were varied along with the incident wave inhomogeneity. The ratio of the longitudinal to shear attenuation coefficients in the solid was held constant at the value computed from the parameters in Section 5.4.1: $\alpha_{ratio} = \alpha_{2L}/\alpha_{2S} = 0.3146$. The frequency was held constant at 10 MHz, and so the variation of the attenuation here is considered to be a simple variation of material parameters, rather than that from frequency-dependence.

Figure 5.5 presents the results for the reflection coefficient magnitude for simultaneous variation of the incident wave inhomogeneity γ_1 and solid dissipation level, as specified in terms of the shear attenuation coefficient α_{2S}. As can be observed, on the left side of the figure (i.e., at lower losses), there is a locus of small reflection values where, for each value of the attenuation, a unique, nonzero value of the inhomogeneity

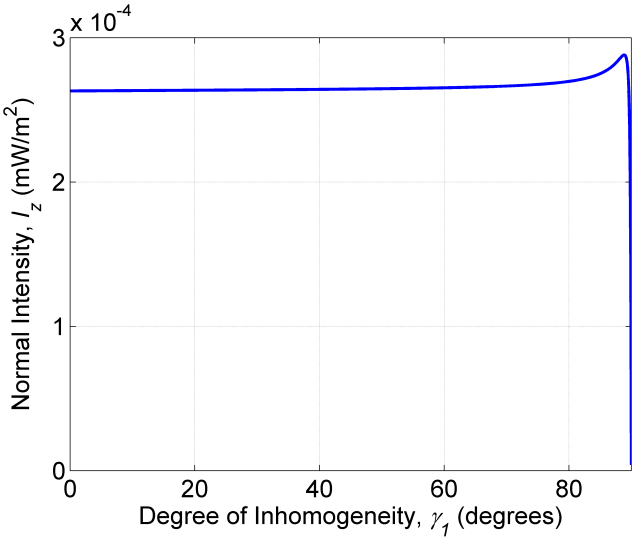

(a)

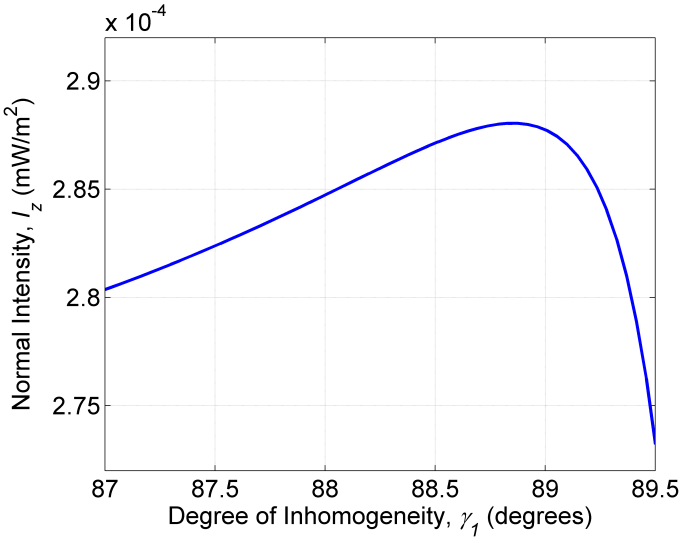

(b)

Figure 5.4. The transmitted normal intensity, at the interface and at tangential position $x = 0$, for the water–stainless steel interface at 10 MHz as a function of the degree of inhomogeneity γ_1 of the 1-Pa incident wave at the Rayleigh angle $\theta_1 = \theta_{Ray} \approx 30.833°$. A close-up view near the local maximum is shown in (b).

can be found to yield the minimum of the reflection coefficient. However, above a critical level of dissipation, no such local minima exist and there is simply a slight

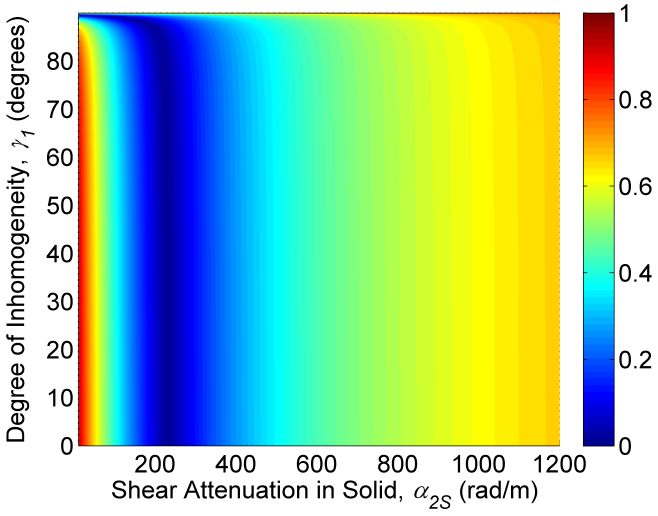

Figure 5.5. The magnitude of the reflection coefficient at 10 MHz, where the properties are those for the water–stainless steel interface except that the attenuation in steel is varied as shown, as a function of the shear attenuation coefficient in steel α_{2S} and the degree of inhomogeneity γ_1 of the incident wave. The incident wave is propagating at the Rayleigh angle and the ratio of the longitudinal to shear attenuation coefficients in steel is held constant at $\alpha_{ratio} = 0.3146$.

variation of the reflection coefficient with respect to the incident wave inhomogeneity, where the lowest values occur for homogeneous incident waves (i.e., at $\gamma_1 = 0°$).

Based on the variation along the line $\gamma_1 = 0°$ in Figure 5.5, it is clear that the critical value of the attenuation coincides with the local minimum in the reflection coefficient with respect to attenuation for a homogeneous incident wave, which was used in the derivation of the approximation for the critical value, Eq. (5.9). As such, for a homogeneous incident wave at the Rayleigh angle, Figure 5.6 presents a direct comparison between the exact result for the reflection coefficient, computed by solving the system in Eq. (5.6), and the result computed by solving the approximate system derived in Section 5.3.2, as the shear attenuation coefficient is varied. For both the magnitude shown in Figure 5.6(a) and the phase shown in Figure 5.6(b), for low values of the attenuation, the approximation is very close to the exact result, as anticipated based on the assumptions used in the approximation. The results diverge,

but remain relatively close, as the attenuation is increased towards the critical value, at which point the magnitude is a minimum and the phase passes through $-90°$. With further increases in the attenuation values, the approximation diverges since the low-loss assumptions are violated. The prediction for the critical value based on the approximation, Eq. (5.9), is $\alpha_{2S}^{\star} \approx 217.9$ rad/m, which yields an error of 6.2% compared to the exact value of $\alpha_{2S}^{\star} = 232.2$ rad/m. In the context of applications which seek to maximize the energy transmitted into the solid, the critical value of the dissipation provides an upper bound below which inhomogeneous incident waves may improve the transmission.

5.4.3 Application to a Low-frequency Air–Solid Interface

Finally, in order to illustrate the phenomena discussed in this chapter in the context of air–solid interfaces, particularly for solids resembling polymer-based binders used in energetic systems and at low frequencies (which may permit reasonable stand-off distances), an air–Sylgard® 184 interface is considered here, with the frequency set at 1000 Hz. The properties of air were again taken as those specified in Chapter 4, at 20 °C and 1 atm: density $\rho_1 = 1.21$ kg/m^3 and longitudinal wave speed $v_{1L} = 343$ m/s [78]. The longitudinal wave attenuation coefficient in dry air (0% relative humidity) at 1000 Hz can be computed as $\alpha_{1L} = 0.176$ rad/km [69]. The elastic properties of Sylgard® were set as those used in Chapter 3: density $\rho_2 = 1030$ kg/m^3 [158], longitudinal wave speed $v_{2L} = 1100$ m/s [161], and shear wave speed $v_{2S} = 570$ m/s [161]. Since no suitable values could be found in the literature for the attenuation coefficients of Sylgard® in the low-frequency regime, the attenuation levels will be varied in a similar way as in Figure 5.5, as detailed below.

First, the shear attenuation coefficient was set at an arbitrary low value for the purpose of illustrating the effect of the incidence angle and degree of inhomogeneity on the reflection coefficient. That shear attenuation value was set as $\alpha_{2S} = 1$ rad/km, and the longitudinal attenuation value was computed using the ratio of the coefficients that

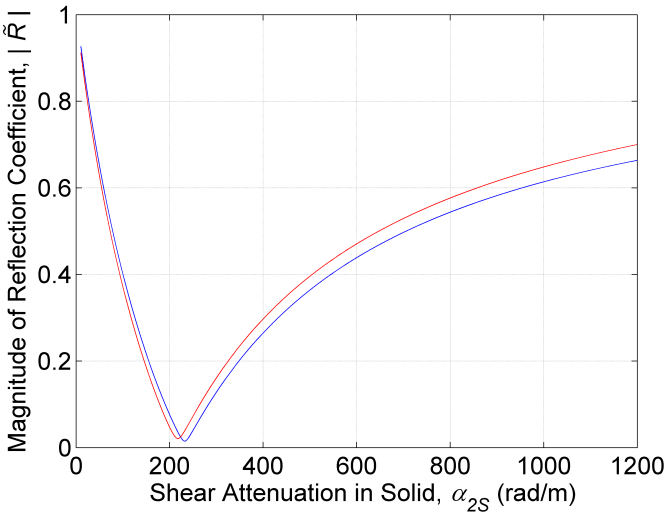

(a)

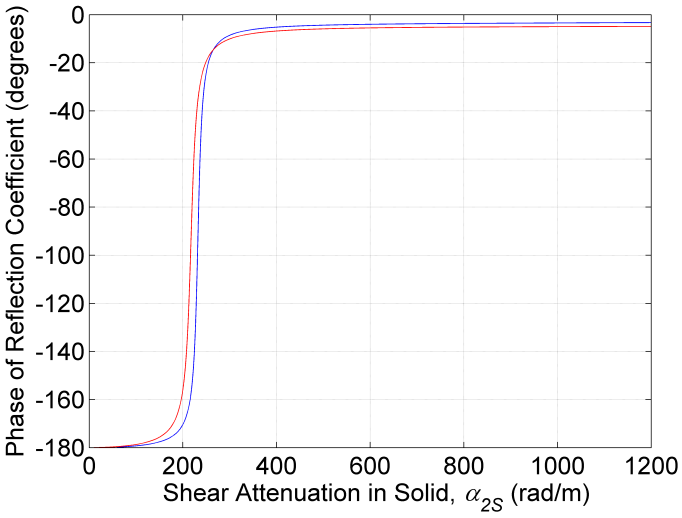

(b)

Figure 5.6. The (a) magnitude and (b) phase of the reflection coefficient at 10 MHz, where the properties are those for the water–stainless steel interface except that the attenuation in steel is varied as shown, as a function of the shear attenuation coefficient in steel α_{2S}. The incident wave is homogeneous and is propagating at the Rayleigh angle, and the ratio of the longitudinal to shear attenuation coefficients in steel is held constant at $\alpha_{ratio} = 0.3146$. The blue curve corresponds to the exact solution, as computed from Eq. (5.6), and the red curve corresponds to the approximation, as derived in Section 5.3.2.

can be calculated from the properties given in Chapter 3 ($\alpha_{ratio} = \alpha_{2L}/\alpha_{2S} = 0.518$), to yield $\alpha_{2L} = 0.518$ rad/km. Figure 5.7(a) presents the magnitude of the reflection coefficient as the incidence angle θ_1 is varied near the Rayleigh angle ($\theta_{Ray} \approx 40.321°$) and the degree of inhomogeneity γ_1 is varied from 0° to values near 90°. As for the high-frequency water–stainless steel interface investigated in Figure 5.3, it is clear that tuning the degree of inhomogeneity at the Rayleigh angle yields much lower reflection values for the air–Sylgard® interface, with the local minimum observed at $\gamma_1 \approx 78.88°$. Figure 5.7(b) shows the direct dependence on the degree of inhomogeneity, with the incidence angle held constant at the Rayleigh angle. The reflection coefficient at the local minimum is $|\tilde{R}| \approx 0.00027$ for the low level of dissipation assumed in Sylgard®, a reflection value which is significantly lower than the value of $|\tilde{R}| \approx 0.263$ for homogeneous incident plane waves.

The dependence of the interface phenomena on the material dissipation level in Sylgard® is also considered here. As noted above, no values could be found in the literature for the attenuation coefficients in the low-frequency regime. The attenuation values are thus varied here, as in Section 5.4.2 for steel, by setting the ratio of the longitudinal to shear coefficients to a constant, nominal value: $\alpha_{ratio} = \alpha_{2L}/\alpha_{2S} = 0.518$. Figure 5.8 shows the results for the reflection coefficient magnitude as the incident wave inhomogeneity γ_1 and solid dissipation level are varied simultaneously, as specified in terms of the shear attenuation coefficient α_{2S}. As was previously observed in Figure 5.5, a locus of small reflection values is evident for attenuation values up to a critical level ($\alpha_{2S}^{\star} = 1.636$ rad/km in this case), below which a unique, nonzero value of the inhomogeneity can be found to yield the minimum of the reflection coefficient. However, above that critical attenuation value, no local minima exist and homogeneous plane waves yield lower reflection coefficient values. This result suggests that, if the wave attenuation levels at low frequencies in Sylgard® and other polymers used as binder materials are found to lie above the specified threshold, then inhomogeneous incident waveforms may confer no benefit in terms of the subsurface energy transmission.

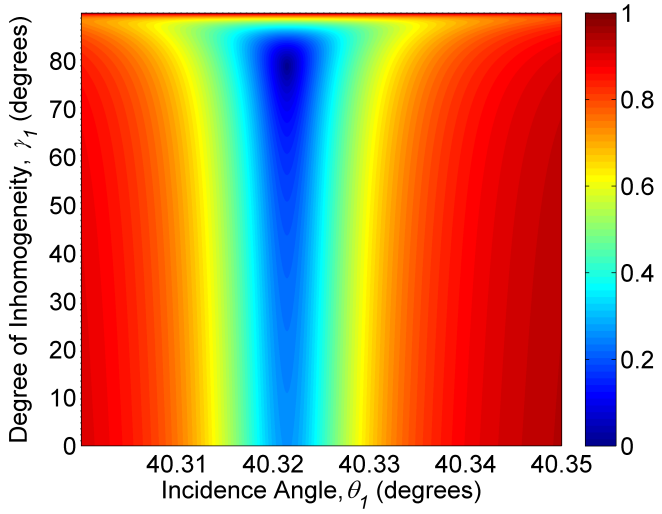

(a)

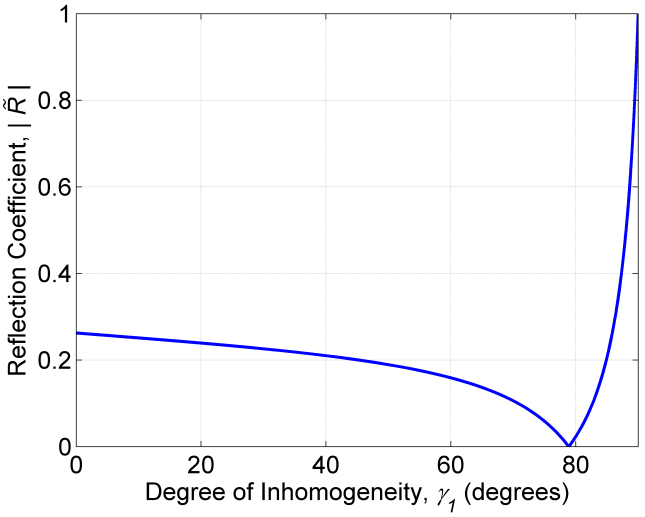

(b)

Figure 5.7. The magnitude of the reflection coefficient for the air–Sylgard® interface at 1000 Hz as a function of (a) incidence angle θ_1 and degree of inhomogeneity γ_1 of the incident wave, and (b) degree of inhomogeneity γ_1 of the incident wave at the Rayleigh angle $\theta_1 = \theta_{Ray} \approx 40.321°$.

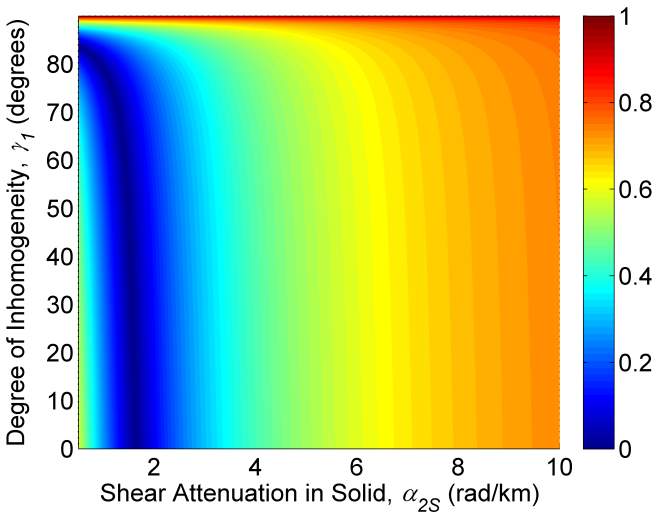

Figure 5.8. The magnitude of the reflection coefficient at 1000 Hz, where the properties are those for the air–Sylgard® interface except that the attenuation in Sylgard® is varied as shown, as a function of the shear attenuation coefficient in Sylgard® α_{2S} and the degree of inhomogeneity γ_1 of the incident wave. The incident wave is propagating at the Rayleigh angle and the ratio of the longitudinal to shear attenuation coefficients in Sylgard® is held constant at $\alpha_{ratio} = 0.518$.

5.5 Conclusions

In this chapter, a model for the transmission of inhomogeneous plane waves across dissipative fluid–solid interfaces has been presented, where a linear hysteretic damping model was assumed. For low-loss solids, inhomogeneous incident waves were shown to substantially reduce the magnitude of the reflection coefficient in comparison with homogeneous waves, and thus increase the energy transmission, for incidence at the Rayleigh angle. Moreover, a unique value of the degree of inhomogeneity could be found which yields the local minimum of the reflection coefficient and, therefore, the maximum energy transmission into the solid at a given frequency. This result is analogous to that for lossless fluid–solid interfaces, as discussed in Chapter 4. However, above a critical level of material dissipation in the solid, inhomogeneous incident waves were found to yield slightly higher reflection values than homogeneous waves, which is attributable to the high degrees of inhomogeneity inherent in the transmitted waves in higher-loss solids. An analytical approximation was derived for the critical dissipation value, and it was found to give predictions close to the exact result for the exemplary interface under consideration.

In the context of the excitation of polymer-bonded energetic materials, the result showing a critical level of solid dissipation above which the use of inhomogeneous plane waves does not improve the energy transmission suggests that the specific material composition and frequency range under consideration will play an integral role in determining the optimal waveform. That is, if the material losses are small in comparison with the elastic wave propagation properties, then the use of inhomogeneous waves may offer substantial transmission increases. But if those relative losses are high, then an inhomogeneous wave may confer no benefit.

Also, since bounded acoustic waves can be described by a decomposition of plane waves, the work presented in Chapter 4 and in this chapter suggests that the construction of beam profiles of limited spatial extent for optimal energy transmission may be informed by inhomogeneous plane wave theory. The construction of such bounded

waveforms, particularly the parameters which enhance the surface wave excitation efficiency, is the subject of Chapter 6.

6. BOUNDED INHOMOGENEOUS WAVE PROFILES FOR OPTIMAL SURFACE WAVE EXCITATION EFFICIENCY

6.1 Introduction

Though plane wave theory may provide insight into the acoustic wave profiles which optimize the energy transmission into solid materials, as detailed in Chapters 4 and 5, bounded waves must be used in practice. It is thus the purpose of this chapter to investigate incident wave profiles of limited spatial extent, again with incidence near the Rayleigh angle. In the study of bounded waves, the surface wave excitation efficiency is a metric of particular utility, since it accounts for the penetration of the incident wave energy at specified points along the interface, which is subsequently reradiated in the form of the Rayleigh-type surface wave [113, 117]. With polymer-bonded energetic materials as the target surfaces, this metric may ultimately be insightful as a quantitative measure of the fraction of the incident energy transmitted near the solid surface, which may prove useful in designing wave profiles to elicit maximal heating near the surface. As such, the investigations presented in this chapter seek to maximize the surface wave excitation efficiency by varying the incident wave profile.

A versatile form of the incident profile based on the work of Vanaverbeke et al. [117] is considered, which contains a component of exponential decay perpendicular to the propagation direction (analogous to that of inhomogeneous plane waves). Such "bounded inhomogeneous wave" profiles are compared with the more commonly-studied Gaussian and square profiles. The Fourier method is used to decompose the incident profiles and then compute the reflected wave profiles, from which the energy fluxes and surface wave excitation efficiencies can be subsequently calculated. In addition, the correspondence between the local reflection coefficient as a function of the

incident wave decay rate and that predicted by plane wave theory is also considered. The results reveal that unique values of the incident wave decay rate and beamwidth can be found which yield the global maximum of the surface wave excitation efficiency with incidence near the Rayleigh angle, a result that is analogous to the minimal reflection values observed for plane waves. Moreover, inhomogeneous plane wave theory predicts, to a close approximation, the location of the minimum in the local reflection coefficient with respect to the decay rate for the bounded inhomogeneous waves, which is exact in the limit of large beamwidths. Major portions of this chapter were submitted in a manuscript to the Journal of the Acoustical Society of America [176].

6.2 Fourier Decomposition of Bounded Inhomogeneous Wave Profiles

A bounded harmonic acoustic wave, with an arbitrary incident profile, in a semi-infinite fluid medium is considered here. The two-dimensional wave propagating in the xz-plane is incident at a solid interface, and the rectangular coordinate systems are shown in Figure 6.1. The fluid is assumed to be linear, isotropic, homogeneous, and lossless. The solid is also assumed to be linear, isotropic, and homogeneous, but may be either lossless or linear viscoelastic.

By using the form presented by Vanaverbeke et al. [117] for the particle displacement, the wave potential of a longitudinal, bounded inhomogeneous incident wave can be modeled, in the frame of the wave and at $z' = 0$, by the analytical expression:

$$\tilde{\Phi}_{inc}(x', 0) = \tilde{\Phi}_0 e^{\left[\beta x' - \frac{1}{c}\left(\frac{|x'|}{W}\right)^c\right]} e^{-j\omega t}, \tag{6.1}$$

where β is the decay parameter, W is the half beamwidth, c is the steepness parameter, ω is the angular frequency, t is the time variable, and $\tilde{\Phi}_0$ is the wave potential amplitude. This versatile form of the profile not only allows for an exponentially decaying term that is analogous to the decay of inhomogeneous plane waves perpendicular to the propagation direction, but it also facilitates the modeling of other waveforms, including Gaussian and square profiles [117]. Note that the term "bounded" is used to describe profiles of this type since the amplitude takes on very small values

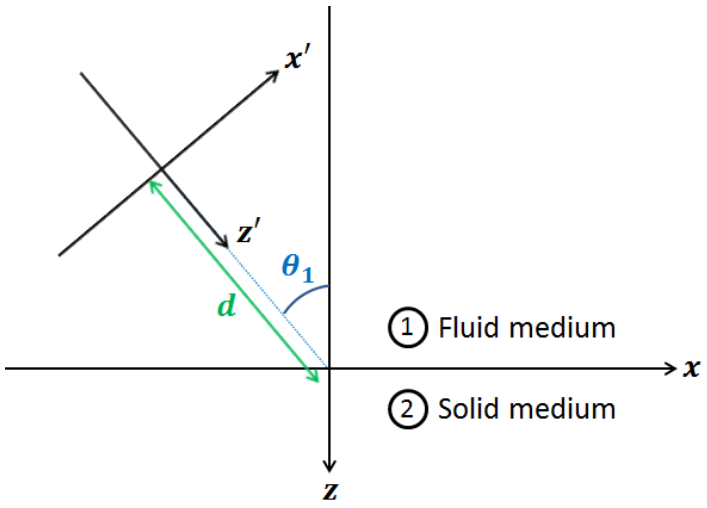

Figure 6.1. A diagram showing the utilized rectangular coordinate systems at the fluid–solid interface. The unprimed system lies in the frame of the interface, and the primed system lies in the frame of the incident wave, which propagates in the positive z'-direction.

outside of the spatial region near $x' = 0$, a spatial windowing which is controlled by the term $e^{-\frac{1}{c}\left(\frac{|x'|}{W}\right)^c}$ in Eq. (6.1). The function is, however, defined over the entire x'-axis.

The Fourier transform can be applied to this incident profile in a straightforward way in order to subsequently obtain the reflected wave profile in the frame of the interface (i.e., in the xz-frame). For the sake of brevity, the details of the derivation, which are given in the literature [77, 111, 113–117], are omitted here. The profile of the incident wave at the interface can be approximated as:

$$\tilde{\Phi}_{inc}(x,0) = \tilde{\Phi}_0 e^{\left[\beta_0 x - \frac{1}{c}\left(\frac{|x|}{W_0}\right)^c\right]} e^{j(k_0 x + k_{1L} d - \omega t)}, \tag{6.2}$$

where k_{1L} is the longitudinal material wavenumber in the fluid, $k_0 = k_{1L}\sin(\theta_1)$ is the x-component of the mean wavevector, $\beta_0 = \beta\cos(\theta_1)$ is the projected decay parameter, and $W_0 = W/\cos(\theta_1)$ is the projected half beamwidth. The phase propagation effect has been incorporated through the term $e^{jk_0 x}$, which accounts

for the variation along the interface, and through the plane wave propagation term $e^{jk_{1L}d}$ [111, 113, 117]. The Fourier transform in the interface frame is then given as:

$$\tilde{F}_{inc}(k_x) = \int_{-\infty}^{+\infty} \tilde{\Phi}_{inc}(x,0)e^{-jk_x x}\mathrm{d}x, \tag{6.3}$$

and the wave potential profile of the reflected wave is thus:

$$\tilde{\Phi}_{refl}(x,0) = \frac{1}{2\pi}\int_{-\infty}^{+\infty} \tilde{R}(k_x)\tilde{F}_{inc}(k_x)e^{jk_x x}\mathrm{d}k_x, \tag{6.4}$$

where $\tilde{R}$ is the plane wave reflection coefficient, which, as previously discussed, has been presented in the literature for both the lossless fluid–solid interface [77] (see Chapter 4) and the viscoelastic fluid–solid interface [66, 106, 107, 110] (see Chapter 5). The term $e^{jk_{1L}d}$ in Eq. (6.2), which introduces a constant factor due to the offset distance d between the frame of the incident wave and the frame of the interface, will be omitted in subsequent calculations (i.e., d is set to 0) for the sake of simplicity.

6.3 Efficiency of Rayleigh-type Surface Wave Excitation

When a bounded acoustic beam is incident at a solid surface near the Rayleigh angle, a portion of the incident energy is transmitted into the solid and carried within the solid medium along the interface (i.e., in the x-direction in Figure 6.1) [111, 113, 117]. This energy flux generates a Rayleigh-type surface wave on the solid, which then reradiates energy into the fluid to form the displaced portion of the reflected profile. This shift of the reflected wave along the interface has been described in detail for Gaussian incident profiles [111, 113] and for bounded inhomogeneous incident profiles [117]. There thus exists, near the incident beam, an energy flux at any given position x along the interface which will be reradiated into the fluid by the excitation of the surface wave.

In order to quantify the surface wave generation by bounded inhomogeneous incident waves, the surface wave excitation efficiency, as a function of the position along the interface, can be defined as the difference between the incident and reflected inten-

sities normal to the interface, integrated from $-\infty$ to x and normalized with respect to the total incident normal intensity [113, 117]:

$$\eta_{eff}(x) = \frac{\int_{-\infty}^{x} [\, |I_{inc,z}(\Xi,0)| - |I_{refl,z}(\Xi,0)| \,] \, \mathrm{d}\Xi}{\int_{-\infty}^{+\infty} |I_{inc,z}(\Xi,0)| \mathrm{d}\Xi}, \tag{6.5}$$

where $I_{inc,z}(x,z)$ and $I_{refl,z}(x,z)$ are the normal intensities of the incident and reflected waves, respectively. The intensities for each wave, denoted with the subscript m, are straightforward to compute in the lossless fluid as $I_{m,z} = \mathrm{Re}\left[-\tilde{\sigma}_{m,zz}\, \partial \tilde{u}^{*}_{m,z}/\partial t\right]/2$, where Re denotes the real part of the argument, the asterisk denotes the complex conjugate, $\tilde{\sigma}_{m,zz} = -\rho_1 \omega^2 \tilde{\Phi}_m$ is the associated normal stress (ρ_1 is the density of the fluid), and $\tilde{u}_{m,z}$ is the associated normal displacement:

$$\begin{aligned} \tilde{u}_{inc,z}(x,0) &= \frac{\omega}{2\pi} \int_{-\infty}^{+\infty} \tilde{k}_z \tilde{F}_{inc}(k_x) e^{jk_x x} \mathrm{d}k_x, \\ \tilde{u}_{refl,z}(x,0) &= \frac{\omega}{2\pi} \int_{-\infty}^{+\infty} -\tilde{k}_z \tilde{R}(k_x) \tilde{F}_{inc}(k_x) e^{jk_x x} \mathrm{d}k_x, \end{aligned} \tag{6.6}$$

where $\tilde{k}_z = (k_{1L}^2 - k_x^2)^{1/2}$ is evaluated as the principal square root [66] and is the z-component of the constituent wavevector. The surface wave excitation efficiency takes on its maximum value at a position x_{max}, beyond which point the reflected normal intensity exceeds the incident intensity. However, it should be noted that, for the case of a plane incident wave, the excitation efficiency is independent of the position along the interface, since the ratio of the incident and reflected wave amplitudes is a function of only the plane wave reflection coefficient. Eq. (6.5) thus simplifies, for a plane wave, to $\eta_{eff} = 1 - |\tilde{R}|^2$.

6.4 Numerical Results and Discussion

In order to illustrate the effect of the spatial decay rate of the incident wave on the surface wave generation at fluid–solid interfaces, a water–stainless steel interface is considered here. The interface is first treated as lossless, and then viscoelastic losses in stainless steel are incorporated in the results. The frequency was set to $f = 4$ MHz ($f = \omega/[2\pi]$), which is within the range for typical ultrasonic nondestructive

testing applications (referred to here as a discipline in which surface wave excitation is commonly employed). The densities and wave speeds of the two media were taken to be those used by Vanaverbeke et al. [117]: for water, density $\rho_1 = 1000$ kg/m^3 and longitudinal wave speed $v_{1L} = 1480$ m/s; and for stainless steel, density $\rho_2 = 7900$ kg/m^3, longitudinal wave speed $v_{2L} = 5790$ m/s, and shear wave speed $v_{2S} = 3100$ m/s. For the case in which viscoelastic losses in stainless steel are included, which is considered in Section 6.4.2, the longitudinal and shear wave attenuation coefficients at the given frequency were taken, respectively, to be $\alpha_{2L} = 16.0$ rad/m and $\alpha_{2S} = 50.8$ rad/m, which were computed from the inverse quality factors used by Borcherdt [66] for stainless steel. The steepness parameter in Eq. (6.1) was set to $c = 8$ for the bounded inhomogeneous incident profiles [117], and the wave potential amplitude $\tilde{\Phi}_0$ was taken to be an arbitrary constant.

To illustrate the form of the incident and reflected wave profiles, several incident profiles are presented in Figure 6.2(a), and an incident profile along with the corresponding reflected profile at the lossless water–stainless steel interface is shown in Figure 6.2(b), with incidence at $\theta_1 = 30.968°$, near the Rayleigh angle. The shift of the peak in the reflected wave profile along the interface is analogous to the shift observed for Gaussian incident waves [111, 113]. For a detailed account of the form of the incident and reflected profiles, the reader is referred to the work of Vanaverbeke et al. [117].

In addition to the surface wave excitation efficiency defined by Eq. (6.5), the local reflection coefficient [117], defined as the ratio $|\tilde{\Phi}_{refl}|/|\tilde{\Phi}_{inc}|$, was considered at $x = z = 0$ as a measure of the local transmission efficiency at this point. Specifically, the effect of the decay parameter β was of interest here. It should also be noted that convergence of the numerical implementation of the Fourier decomposition and incident wave reconstruction was verified for all of the cases considered here. Moreover, the boundary conditions at the interface and the conservation of the energy flux carried by the incident, reflected, and transmitted waves were verified as well.

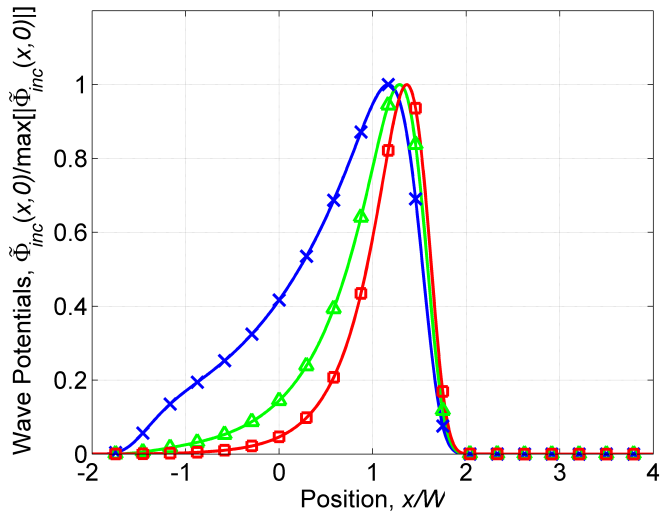

(a)

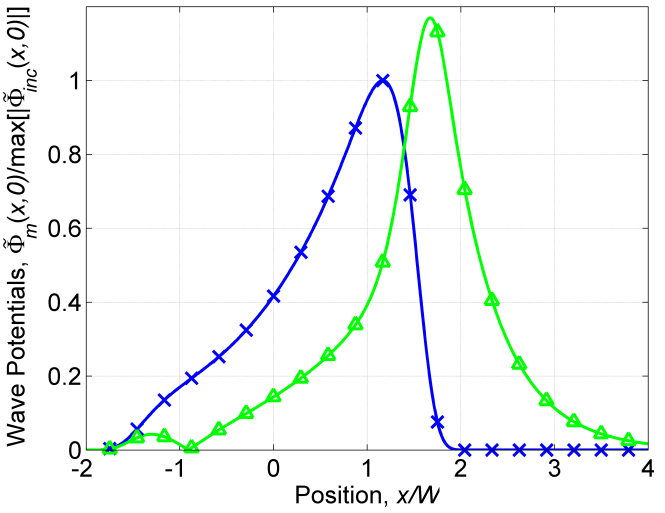

(b)

Figure 6.2. (a) Several incident bounded wave profiles ($c = 8$) of half beamwidth $W = 20$ mm, with decay parameters $\beta = 50$ rad/m ($\times$ markers), $\beta = 100$ rad/m (triangular markers), and $\beta = 200$ rad/m (square markers); and (b) an incident bounded wave profile ($W = 20$ mm, $\beta = 50$ rad/m, $c = 8$; $\times$ markers) along with the reflected wave profile (triangular markers) for the water–stainless steel interface at 4 MHz, with losses neglected.

6.4.1 Water–Stainless Steel Interface

For the lossless water–stainless steel interface, the magnitude of the reflection coefficient for an incident inhomogeneous plane wave and the magnitude of the local reflection coefficient for several bounded inhomogeneous incident waves are presented in Figure 6.3 as a function of the decay parameter β. The waves are incident at the angle that minimizes the reflection coefficient, $\theta_1 \approx 30.968°$, which is near the Rayleigh angle. For the plane wave, the decay parameter gives the rate of exponential decay perpendicular to the propagation direction, as was detailed in Chapter 4. As is evident, the form of the plane wave reflection coefficient, including the location of the minimum, is closely matched by the local reflection coefficients for the higher beamwidths. The decay parameter which yields the minimum for the profile with the half beamwidth $W = 30$ mm is $\beta \approx 110.8$ rad/m, which gives a 0.18% error with respect to the value for the plane incident wave, $\beta \approx 111.0$ rad/m. Moreover, as expected, the correspondence between this decay value for bounded waves and that predicted by plane wave theory is found to be exact in the limit of large beamwidths. The profile with the smallest beamwidth in Figure 6.3, however, shows a considerable shift to a lower value of the decay parameter to yield the minimum. This is due to the fact that smaller beamwidths inherently possess a greater degree of inhomogeneity (as the spatial windowing dominates over a larger portion of the profile), and so less inhomogeneity must be introduced through the exponentially decaying term in order to achieve the optimal level of inhomogeneity. Also of note in Figure 6.3(b) is the small nonzero value of the reflection coefficient at the minimum for the bounded wave profiles, as opposed to the zero value for the incident plane wave. The nonzero minimum value is attributable to the effect of the presence of the suboptimal wavevector components which are inherent in the bounded wave profile and which are quantified by the decomposition in Eq. (6.3).

Figure 6.4(a) shows the surface wave excitation efficiency, evaluated at the critical point x_{max} that yields the maximum efficiency, as a function of the decay parameter

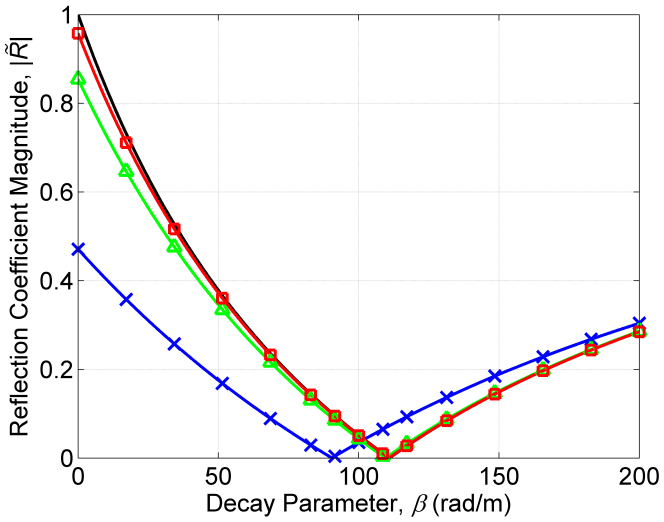

(a)

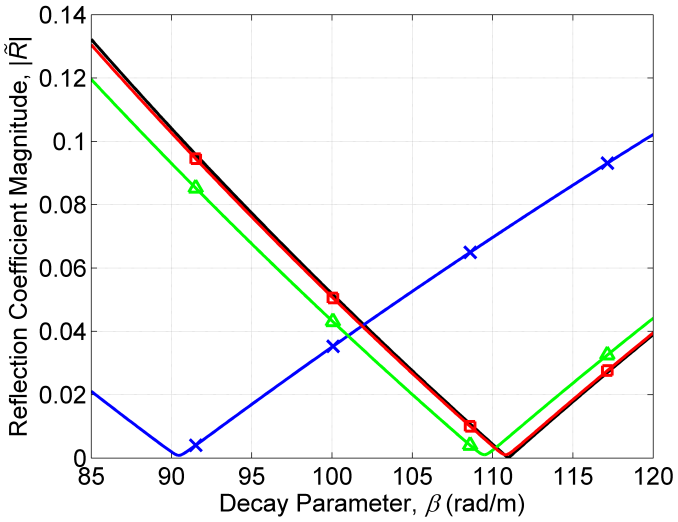

(b)

Figure 6.3. The magnitude of the reflection coefficient for the water–stainless steel interface at 4 MHz, with losses neglected, as a function of the incident wave decay parameter β. The incident waves are specified as an inhomogeneous plane wave (unmarked curve), and bounded wave profiles ($c = 8$) of half beamwidths $W = 10$ mm ($\times$ markers), $W = 20$ mm (triangular markers), and $W = 30$ mm (square markers). The curves for the inhomogeneous plane wave and bounded wave profile of half beamwidth $W = 30$ mm are nearly coincident. Note that (b) gives a zoomed-in view near the local minima.

and half beamwidth of the incident wave. The global maximum of the excitation efficiency is observed at a decay parameter of $\beta \approx 134.2$ rad/m and a half beamwidth of $W \approx 7.7$ mm, which yield an efficiency of $\eta_{eff}(x_{max}) \approx 92.8\%$. Vanaverbeke et al. [117] noted the local maximum with respect to the beamwidth, and the results presented here indicate that a maximum with respect to the decay parameter can also be located. As a point of comparison with more common incident wave profiles, the peaks in the excitation efficiency with respect to the beamwidth for Gaussian ($\beta = 0$, $c = 2$) and square ($\beta = 0$, $c = 8$; i.e., an approximation to a square profile) waves are found to be approximately 80.2% and 80.9%, respectively. The use of the bounded inhomogeneous profiles considered here, with the optimal decay parameter and beamwidth, thus yields an improvement of around $12 - 13\%$ over those more common profiles. This improvement is even more pronounced for beamwidths which are larger than that at the peak value, and the relative increase in the excitation efficiency at a half beamwidth of 50 mm, for example, exceeds 50% as compared to both Gaussian and square incident waves (see also [117]). As is evident in Figure 6.4(a), the value of the decay parameter which yields the global maximum lies above the value which yields the reflection coefficient minimum, and this result is attributable to the greater spatial concentration of the incident wave's energy for the higher spatial decay rates. As such, the peak in the fraction of the energy flux available for surface wave generation is larger for greater decay rates, and the energy is reradiated over a larger distance (i.e., the peak in the reflected wave profile is shifted farther along the interface). Moreover, for beamwidths larger than the width which yields the global maximum, the optimal decay parameter is shifted to higher values since the greater spatial concentration of the incident wave provided by larger decay values is more significant for the larger beamwidths. This effect is balanced by the increased transmission at the local minimum of the reflection coefficient at lower decay parameter values.

Figure 6.5(a) presents the surface wave excitation efficiency as a function of only the decay parameter at the same half beamwidths as were used for calculating the

reflection coefficients shown in Figure 6.3, along with a plane incident wave, where the decay parameter range is increased to show the maximum for each beamwidth. For the plane wave, the peak in the excitation efficiency (which reaches an efficiency of 100%) is observed to occur at the exact decay value which yields the zero of the reflection coefficient, and the shift in the optimal decay rate to higher values for the bounded waves, which increases with beamwidth, is readily apparent. It should also be noted that, for the case of a homogeneous plane incident wave (i.e., $\beta = 0$), though stress fields are induced near the solid surface, at any given point along the interface, the energy from the incident wave is entirely reflected back into the fluid, and thus no energy is available for surface wave excitation at other points on the interface, which is shown by the zero value of the efficiency in Figure 6.5(a).

6.4.2 Effect of Viscoelastic Losses in the Solid Medium

The effect of viscoelastic losses in the solid medium is considered here for the water–stainless steel interface. The magnitude of the reflection coefficient for an incident inhomogeneous plane wave and for several bounded inhomogeneous incident waves (using the local reflection coefficient, as before, at $x = z = 0$) is presented in Figure 6.6, with the waves again incident near the Rayleigh angle to minimize the reflection coefficient. It should be noted that this optimal angle, $\theta_1 \approx 30.973°$, is slightly shifted relative to the lossless case. As is evident in Figure 6.6, the main effect of the incorporation of the viscoelastic losses is the shift in the minimum of the reflection coefficient to significantly smaller values of the decay parameter. Since losses in the solid medium introduce additional levels of inhomogeneity in the transmitted waves, a smaller degree of inhomogeneity is necessary to optimize the transmission, as was previously noted for the case of incident inhomogeneous plane waves (see Chapter 5). Moreover, the plane wave reflection coefficient magnitude remains less than unity even when the incident wave is homogeneous ($\beta = 0$), due to the losses in the solid. As can be observed, the reflection coefficients for the bounded wave profiles

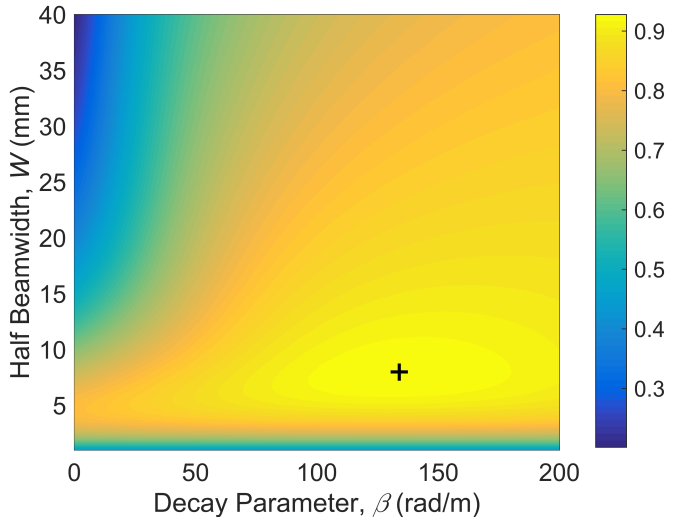

(a)

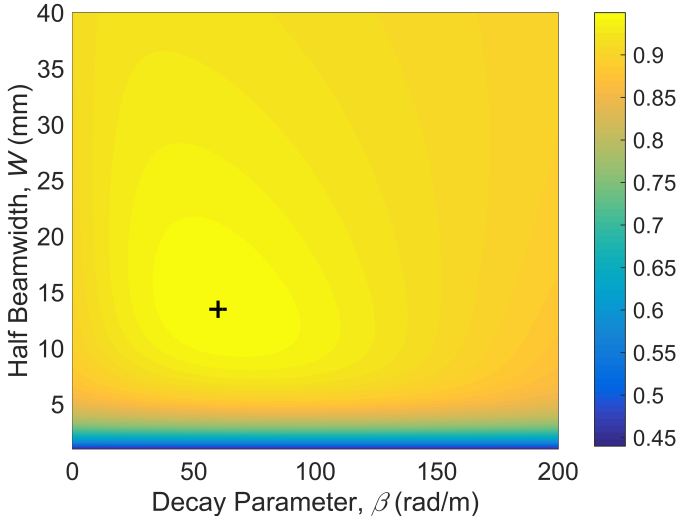

(b)

Figure 6.4. The surface wave excitation efficiency, evaluated at the critical point x_{max}, for the water–stainless steel interface at 4 MHz (a) with losses neglected and (b) with the viscoelastic losses in steel included, as a function of the incident wave decay parameter β and half beamwidth W for the bounded incident wave profiles ($c = 8$). The + marker indicates the global maximum.

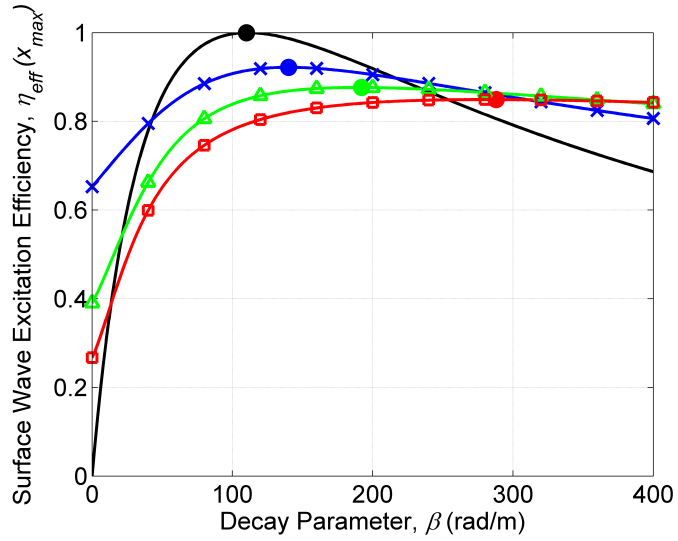

(a)

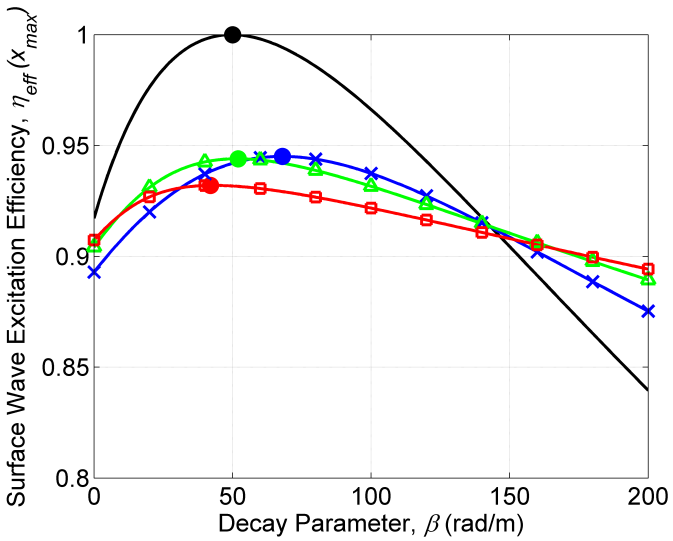

(b)

Figure 6.5. The surface wave excitation efficiency, evaluated at the critical point x_{max}, for the water–stainless steel interface at 4 MHz (a) with losses neglected and (b) with the viscoelastic losses in steel included, as a function of the incident wave decay parameter β. The incident waves are specified as an inhomogeneous plane wave (unmarked curve), and bounded wave profiles ($c = 8$) of half beamwidths $W = 10$ mm ($\times$ markers), $W = 20$ mm (triangular markers), and $W = 30$ mm (square markers). The solid, circular markers indicate the maxima for the respective incident waves.

again closely match that of the plane wave for the larger beamwidths. Also of note is the increase in the reflection coefficient value at the minimum as compared to the lossless case, which is particularly evident for the smallest beamwidth, $W = 10$ mm, in Figure 6.6(b). This result also follows from the introduction of material damping, which increases the value at the local minimum.

Referring back to Figure 6.4, for which results were discussed above for the lossless case, Figure 6.4(b) shows the surface wave excitation efficiency, again evaluated at the critical point x_{max}, as a function of the decay parameter and half beamwidth with the viscoelastic losses in stainless steel included. A global maximum can again be found but, with respect to the lossless case, the corresponding decay parameter is shifted to a lower value and the corresponding beamwidth is shifted to a higher value. This optimal decay rate, however, is still above the decay rate which yields the minimum of the reflection coefficient for the viscoelastic case. Interestingly, for beamwidths larger than that which yields the global maximum of the excitation efficiency, the optimal decay parameter decreases with increasing beamwidth, and this decay value ultimately falls below that which gives the reflection coefficient minimum. This effect may be due to the greater levels of inhomogeneity introduced in the transmitted waves by the material damping for the larger beamwidths, since these wave profiles experience the effects of the viscoelastic losses over a greater distance along the interface.

Finally, referring back to Figure 6.5, Figure 6.5(b) gives the surface wave excitation efficiency as a function of just the decay parameter for the same half beamwidths as were previously considered, along with a plane incident wave, with viscoelastic losses included. As for the lossless case, the excitation efficiency for the plane incident wave reaches its maximum at the value of the decay parameter which yields the minimum of the reflection coefficient. Since the half beamwidth $W = 10$ mm lies below that which gives the global maximum for this case, the decay parameter which yields the peak efficiency is shifted to larger values, whereas the other two beamwidths shown in Figure 6.5(b) lie above the global maximum and therefore show shifts to smaller

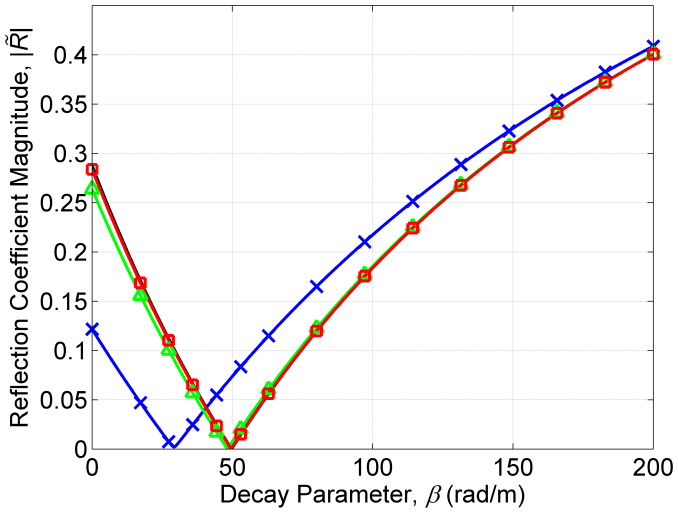

(a)

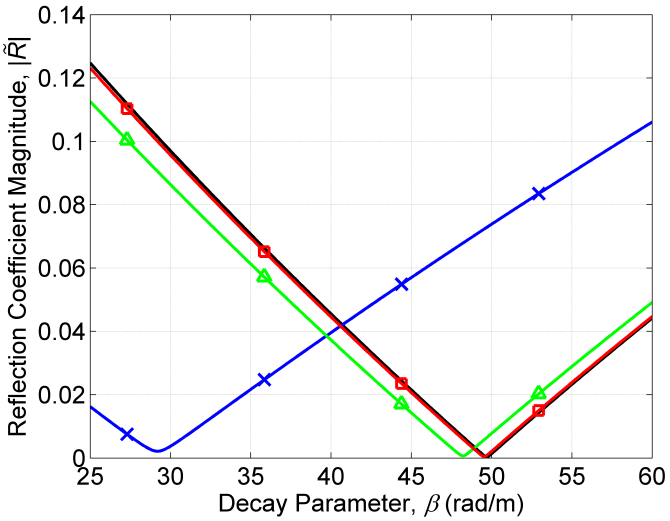

(b)

Figure 6.6. The magnitude of the reflection coefficient for the water–stainless steel interface at 4 MHz, with the viscoelastic losses in steel included, as a function of the incident wave decay parameter β. The incident waves are specified as an inhomogeneous plane wave (unmarked curve), and bounded wave profiles ($c = 8$) of half beamwidths $W = 10$ mm ($\times$ markers), $W = 20$ mm (triangular markers), and $W = 30$ mm (square markers). The curves for the inhomogeneous plane wave and bounded wave profile of half beamwidth $W = 30$ mm are nearly coincident. Note that (b) gives a zoomed-in view near the local minima.

decay parameter values to yield the respective peaks in excitation efficiency. Also note that the value of the efficiency for the homogeneous plane wave case ($\beta = 0$) is nonzero due to the losses in the solid. It follows that the excitation efficiency for the bounded wave profiles increases with increasing beamwidth in the limit of small values of the decay parameter.

6.4.3 Application to a Low-frequency Air–Solid Interface

Similar to the investigation in Section 5.4.3, an air–Sylgard® 184 interface at 1000 Hz is briefly considered here, in order to illustrate the surface wave excitation efficiency optimization using bounded inhomogeneous waves in the context of low-frequency air–solid interfaces, with the solid resembling polymer-based binders used in energetic systems. The material properties utilized are the same as those given in Section 5.4.3: for air at 20 °C and 1 atm (approximated here as lossless at 1000 Hz), density $\rho_1 = 1.21$ kg/m^3 and longitudinal wave speed $v_{1L} = 343$ m/s [78]; and for Sylgard®, density $\rho_2 = 1030$ kg/m^3 [158], longitudinal wave speed $v_{2L} = 1100$ m/s [161], and shear wave speed $v_{2S} = 570$ m/s [161].

Figure 6.7 presents the surface wave excitation efficiency for the low-frequency air–Sylgard® interface, likewise evaluated at the critical point x_{max} that yields the maximum efficiency, as the decay parameter and half beamwidth of the incident wave are varied, with the wave attenuation in Sylgard® neglected in the low-frequency regime. The incidence angle is set at $\theta_1 = 40.321°$, near the Rayleigh angle. As is evident, a global maximum in the efficiency can also be identified for this interface at unique values of the decay parameter and half beamwidth. Those optimal values are found to be $\beta \approx 2.5$ rad/km and $W \approx 3.1$ m, which yield an efficiency of $\eta_{eff}(x_{max}) \approx 93.0\%$. Note the lower values of the decay parameter and the larger values of the beamwidth as compared to the water–stainless steel case, which are primarily due to the much lower frequency under consideration, but also due to the differences in the material properties. The introduction of the nonzero (asymmetrical) spatial

exponential decay in the profile, as before, thus improves the efficiency of the surface wave excitation and energy transmission into the Sylgard® medium as compared to symmetrical waveforms. Moreover, this result suggests that tuning the form of the wave profile in this manner, which was informed by inhomogeneous plane wave theory, may ultimately improve the transmission, for certain compositions, in trace vapor detection applications that seek to employ standoff excitation. It should be further noted that, depending on the levels of longitudinal and shear wave attenuation in Sylgard® assumed at this frequency, similar results can be achieved with viscoelastic losses included, with an observed shift in the optimal decay parameter to lower values.

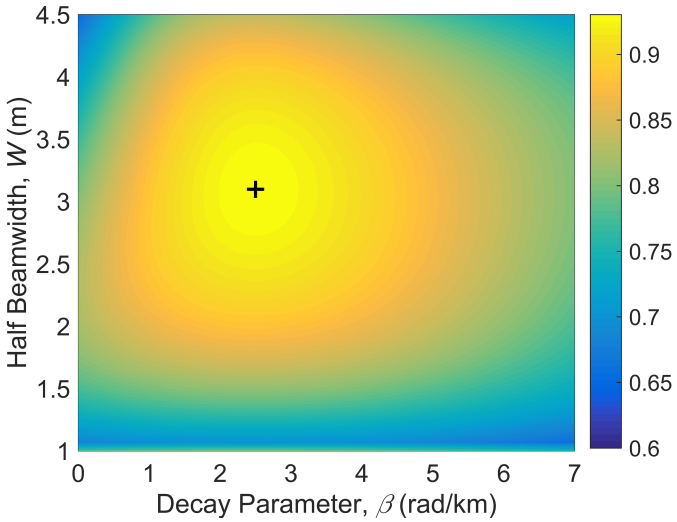

Figure 6.7. The surface wave excitation efficiency, evaluated at the critical point x_{max}, for the air–Sylgard® interface at 1000 Hz, with losses neglected in the low-frequency regime, as a function of the incident wave decay parameter β and half beamwidth W for the bounded incident wave profiles ($c = 8$). The + marker indicates the global maximum.

6.5 Conclusions

In this chapter, a comparison of the predictions for the reflection coefficient and for the surface wave excitation efficiency of incident plane waves and incident bounded

inhomogeneous waves as a function of the incident wave spatial decay rate has been presented for an exemplary lossless fluid–solid interface and also with viscoelastic losses included in the solid. This investigation extends that of Vanaverbeke et al. [117], who demonstrated that bounded inhomogeneous waves improve the surface wave excitation efficiency as compared to Gaussian and square waves, by examining the effect of tuning the decay parameter. It was shown here that the minimum in the plane wave reflection coefficient with respect to the decay parameter provides a good prediction of the minimum in the local reflection coefficient for bounded wave profiles, which is exact in the limit of large beamwidths. Inhomogeneous plane wave theory also provides an indication of the decay parameter value which maximizes the surface wave excitation efficiency, but this value is sensitive to the beamwidth of bounded waves and there is generally a shift to larger decay parameter values due to the greater spatial concentration of the incident wave energy at those larger decay rates. The incorporation of viscoelastic losses in the solid, however, has the effect of introducing additional inhomogeneity to the transmitted waves, and so lower values of the decay parameter were found to yield the maximum excitation efficiency with the losses included.

As was discussed in Section 6.4.3, for the application of the excitation of energetic materials, the results presented in this chapter suggest that the profile of incident acoustic waveforms of finite extent can be tuned to enhance the local energy transmission and surface wave generation. Namely, optimal values of the incident wave decay rate and beamwidth could be identified with incidence near the Rayleigh angle to maximize the surface wave excitation efficiency for the interfaces considered. Moreover, the generation of bounded inhomogeneous waves of the type considered in this work, in particular, was investigated by Declercq and Leroy [119], and it was noted that a reasonable approximation may be achievable in the near-field.

It should also be noted here that further investigation of the effective material properties of typical energetic materials, especially the attenuation coefficients and the frequency-dependence of the properties, would be needed in order to further assess

the viability of such incident wave profiles to enhance the energy transmission and surface wave excitation efficiency for those material compositions. In addition, the effect of barriers between the target material and air medium, such as metal shells or plastic casings, which often exist in practice, should be considered in the design of the incident waveform. Similarly, if the dimensions of the target sample are not sufficiently large in comparison with an acoustic wavelength, then the effect of the boundary conditions should also be taken into account in the consideration of the optimal wave profile. Though these considerations lie beyond the scope of the present work, their incorporation in expanded analytical models may ultimately shed additional light on the acoustic wave profiles which improve the energy transmission at fluid–solid interfaces in the application under consideration and in additional applications.

7. CONCLUSIONS AND FUTURE DIRECTIONS

In this dissertation, two main areas of research were investigated, namely the viscoelastic heating in polymer-bonded energetic and surrogate materials under applied excitation, and the increased acoustic energy transmission into solid media through the use of inhomogeneous incident wave profiles. As previously discussed, the vapor pressures of explosive materials generally exhibit a strong dependence on temperature, and thus the selective heating of hidden explosives may provide a pathway to improved trace vapor-based detection capabilities. The investigations presented in this work were undertaken in order to improve the understanding of the thermal response of polymer-based energetic systems as well as to investigate methods which may ultimately prove useful in providing standoff excitation to elicit temperature rises. This chapter summarizes the major contributions of the work, and then delineates several areas for related future endeavors.

7.1 Contribution of Research

7.1.1 Viscoelastic Heating in Polymer-Bonded Energetic and Surrogate Materials

In Chapter 2, an analytical model, which was based on a linear viscoelastic material model and classical Euler-Bernoulli beam theory, was presented for the volumetric heat generation within a polymer-based particulate composite beam under harmonic mechanical excitation. The HTPB binder material with embedded NH_4Cl crystal served as a surrogate material for polymer-bonded energetic compositions. The thermomechanical model was validated with experiments using an electrodynamic shaker, where good agreement was observed between the predicted and recorded mechanical and thermal responses of the beam. Though the presented viscoelastic model has

been previously characterized and utilized, such an analysis had not previously been applied to compute the bulk heat generation in this specific class of polymer-based particulate composite materials. Moreover, such an experimental investigation and corresponding prediction of the temperature distribution and evolution, where the stress and strain fields were computed analytically along with the heat generation term, had also not been previously undertaken and validated for this class of materials. The results show low-order, bulk-scale heating along the modal structure of the polymer-based system, dependent on the stress-strain distribution and particularly on the square of the strain magnitude for the one-dimensional stress state in a beam geometry. In addition to implications for the viscoelastic heating that may be attainable in systems designed for the mechanical excitation of energetic materials, these results also have implications for the thermal response of munitions, which may be subjected to significant excitation levels in the course of normal operation.

The viscoelastic heating model was extended in Chapter 3 to general three-dimensional stress-strain states, again under the assumption of steady-state harmonic loading. As in the one-dimensional model, the volumetric heat generation is based on the time-averaged losses in the strain energy density, and the generalized Hooke's law for linear viscoelastic media was applied in a straightforward manner in order to generalize the model to three-dimensional stress-strain states. This viscoelastic heat generation model had not been previously extended to general stress-strain states and applied to compute the thermal response in composite systems, particularly those resembling polymer-bonded energetic materials. In addition, though a previously-derived analytical model was employed to compute the stresses in the single crystal–binder system under plane wave excitation, an investigation of the predicted heat generation and temperatures had not been previously undertaken for the wave scattering problem. The results presented for exemplary materials and excitation parameters demonstrated substantial temperature rises near the crystal due to viscoelastic heating alone, with an area of major stress concentration and heating observed at the front edge of the crystal, attributable to scattering of the incident

wave. It is important to note that this effect was observed even in the absence of other mechanisms that are generally considered to contribute significantly to the localized heating in energetic systems, including initial voids or defects, thermal stresses near the crystal, debonding between the crystal and binder, and phase changes or chemical decomposition of the crystal; moreover, this observation had not been previously noted. These results have implications for the heating mechanisms which are significant in energetic systems under continuous excitation, particularly for the formation of hot spots near the crystals. Also, the viscoelastic heating model, which requires only knowledge of the stress state and material properties under harmonic excitation, has broad applicability to the thermal response of polymer-based and other viscoelastic systems subjected to external loading.

7.1.2 Inhomogeneous Waveforms for Acoustic Energy Transmission into Solid Media

In Chapters 4 and 5, inhomogeneous plane waves were investigated for the purpose of increasing the energy transmission at high impedance-difference material interfaces. Those studies showed increased transmission for a range of the inhomogeneity values of the incident wave. For the fluid–solid interface in particular, it was demonstrated that a local minimum of the reflection coefficient could be found by varying the inhomogeneity with the incidence angle for propagation near the Rayleigh angle. In the case of lossless media, this local minimum was further observed to yield a zero of the reflection coefficient, corresponding to perfect transmission of the incident acoustic energy normal to the interface. Such an investigation into the effect of the inhomogeneity on the attainable energy transmission had not been previously considered, nor had the local minimum of the reflection coefficient been illuminated in the context of energy transmission into higher-impedance solid media. Also, in the case of dissipative media, a strong dependence of the optimal incident wave parameters on the material dissipation levels in the solid material was observed. Furthermore, a critical level of

dissipation was uncovered above which no local minimum in reflection could be found (i.e., with respect to the incident wave inhomogeneity), and homogeneous plane waves yielded lower reflection values than inhomogeneous waves for the higher dissipation values. Though these investigations for plane waves were largely theoretical in nature, the results reveal that wave profiles resembling that of an inhomogeneous plane wave may improve the energy transmission in the acoustical or ultrasonic excitation of solid materials. For the application of the excitation of polymer-bonded energetic systems, the observation that higher material losses in the solid (which is typical of polymer-based materials) may hamper the energy transmission by inhomogeneous waves implies that the utility of these waveforms may be limited for those systems. However, the predictions of increased energy transmission through waveform design may prove useful in areas that include the nondestructive evaluation of materials and structures [70, 72, 73], medical ultrasound imaging [76, 177], and other applications in which the use of a couplant is undesirable [71, 74, 75].

The design of optimal wave profiles for energy transmission into solid media was extended to bounded waves in Chapter 6. By simultaneously tuning the beamwidth and inhomogeneity (i.e., the rate of one-sided spatial exponential decay), a global maximum of the surface wave excitation efficiency was observed. It was also noted that the effect of the inhomogeneity on the local reflection coefficient could be approximated by plane wave theory, an approximation that is exact in the limit of large beamwidths. Prior research in this area, particularly that of Vanaverbeke et al. [117], had observed that increased surface wave excitation efficiencies could be achieved through the use of bounded inhomogeneous waveforms, but no previous work had considered tuning the inhomogeneity and subsequently observed the global maximum in the excitation efficiency. As for the studies with plane incident waves, the predictions of enhanced energy transmission by tuning the incident wave profile may prove useful in nondestructive testing, ultrasound imaging, and similar applications. In nondestructive testing in particular, Rayleigh-type surface waves are often excited on solid surfaces through a contact transducer to detect structural defects. The re-

sults presented in this work suggest that the efficiency of that surface wave excitation could be improved by using a bounded inhomogeneous incident wave with a tailored rate of spatial exponential decay, either through contact excitation or through stand-off excitation, if a viable remote system could be designed. In the context of the excitation of energetic materials, if effective wave propagation property data could be obtained (particularly attenuation coefficients and the frequency-dependence of the material properties), the results discussed here also imply that further work on waveform design is warranted to efficiently excite such materials.

7.2 Future Directions

Several related areas of future research should be investigated to further the effort on the selective heating of polymer-bonded energetic materials. Those areas are summarized here and divided into efforts focused on understanding the thermomechanical response of such systems and efforts concerned with efficient excitation to elicit the thermal response.

7.2.1 Thermomechanical Response to Applied Excitation

- *Models for stresses and heating in many-crystal systems*: In Chapter 3, a single crystal–binder system was considered to isolate the effects of the wave scattering and heat generation near the crystal. However, typical energetic systems generally consist of a large number of embedded crystals. As such, the stresses induced in the composite matrix when subjected to external excitation should be investigated, as should the volumetric heat generation. Predictions may then be computed for the temperature increases in such systems through the use of numerical solvers.

- *Viscoelastic heating in additional compositions*: An HTPB binder material with embedded NH_4Cl crystals was used in the experimental study in Chapter 2, and

a Sylgard® binder with an embedded HMX crystal was considered in Chapter 3. Experimental investigations should be conducted on additional binder materials as well as with alternate energetic and surrogate particles. Provided that the applicable material properties can be obtained, the analysis for the prediction of the thermal response presented in this work should be applied to additional compositions as well. Those investigations would further illuminate the viscoelastic heating mechanisms in the context of the broad class of polymer-bonded energetic materials.

- *Heating mechanisms in the presence of defects*: In practice, samples often contain material defects, at which significant stress concentrations and heating may develop. Moreover, the effects of those stress concentrations may be exacerbated by harmonic excitation, particularly under fatigue loading. As such, the heating associated with defects should be characterized experimentally for polymer-bonded energetic and surrogate materials, and corresponding analytical and finite element models should be developed.

7.2.2 Methods for Acoustical Excitation

- *Waveform design for multi-layer systems*: In many cases applicable to hidden explosives detection, the target material is obscured by one or more intervening layers. For example, the explosive may be concealed behind a metal barrier or within a plastic packaging material, or may be hidden beneath a soil layer. In order to inform the efficient excitation of samples in such scenarios, waveform design efforts should be conducted for multi-layer systems, analogous to those efforts presented in Chapters 4, 5, and 6 for single fluid–solid interfaces. Specifically, plane and bounded incident wave parameters should be sought which enhance the energy transmission into the target media.

- *Generation of inhomogeneous waveforms*: Sound field reproduction techniques, such as phased arrays of sources, should be investigated for the generation of

inhomogeneous wave profiles of the type considered in this work. The errors associated with such an implementation, including the empirical source models that must be used in practice, should be quantified, as should the input power requirements. Also, the power requirements for the generation of these types of waves, if they are found to be notably higher than those for more conventional waveforms, should be assessed in relation to the improvement in energy transmission discussed in this work, in order to evaluate the practicality of those profiles for enhanced transmission.

- *Wave speed and attenuation coefficient measurements*: The longitudinal and shear wave speeds, as well as the respective attenuation coefficients, should be measured for polymer-bonded energetic and surrogate compositions of interest in this work. The frequency-dependence of the attenuation coefficients, in particular, would be useful in the evaluation of the predicted energy transmission by various incident wave profiles. Moreover, with accurate wave propagation and attenuation data, further assessment of the viability of bounded inhomogeneous waveforms for enhanced transmission into polymer-bonded energetic materials would be possible.

- *Experimental heat generation through standoff acoustical excitation*: In the context of low-frequency excitation, experiments should be conducted from a standoff distance using appropriate sources, such as phased arrays, to generate incident wave profiles of interest on the surfaces of polymer-bonded energetic samples. The thermal response should be measured, and the acoustical interface phenomena and elicited heat generation should be assessed in relation to the analyses presented in this work. Such an experimental investigation would shed further light on the attainable temperature rises and associated power requirements in a standoff excitation system for vapor-based detection applications.

LIST OF REFERENCES

LIST OF REFERENCES

[1] A. V. Kuznetsov and O. I. Osetrov, "Detection of improvised explosives (IE) and explosive devices (IED)," *Detection and Disposal of Improvised Explosives, NATO Security through Science Series B: Physics and Biophysics*, pp. 7–25, 2006.

[2] D. S. Moore, "Instrumentation for trace detection of high explosives," *Review of Scientific Instruments*, 75(8):2499–2512, 2004.

[3] D. S. Moore, "Recent advances in trace explosives detection instrumentation," *Sensing and Imaging*, 8(1):9–38, 2007.

[4] H. Östmark, S. Wallin, and H. G. Ang, "Vapor pressure of explosives: A critical review," *Propellants, Explosives, Pyrotechnics*, 37(1):12–23, 2012.

[5] P. Mostak and M. Stancl, "IEDs detection by existing detection techniques," *Detection and Disposal of Improvised Explosives, NATO Security through Science Series B: Physics and Biophysics*, pp. 33–41, 2006.

[6] V. Averianov, I. Gorshkov, A. Kuznetsov, and A. Evsenin, "Microwave system for inspection of luggage and people," *Detection and Disposal of Improvised Explosives, NATO Security through Science Series B: Physics and Biophysics*, pp. 43–50, 2006.

[7] G. W. Carriveau, "Associated particle imaging: An enabling technology of detection of improvised explosives," *Detection and Disposal of Improvised Explosives, NATO Security through Science Series B: Physics and Biophysics*, pp. 123–125, 2006.

[8] V. N. Tkach and G. N. Shcherbakov, "Use of non-linear junction detectors to ensure the safety of IED search," *Detection and Disposal of Improvised Explosives, NATO Security through Science Series B: Physics and Biophysics*, pp. 237–239, 2006.

[9] L. C. Pacheco-Londono, W. Ortiz-Rivera, O. M. Primera-Pedrozo, and S. P. Hernandez-Rivera, "Vibrational spectroscopy standoff detection of explosives," *Analytical and Bioanalytical Chemistry*, 395(2):323–335, 2009.

[10] J. S. Caygill, F. Davis, and S. P. Higson, "Current trends in explosive detection techniques," *Talanta*, 88(1):14-29, 2012.

[11] X. Pan, K. Tian, L. E. Jones, and G. P. Cobb, "Method optimization for quantitative analysis of octahydro-1, 3, 5, 7-tetranitro-1, 3, 5, 7-tetrazocine (HMX) by liquid chromatography–electrospray ionization mass spectrometry," *Talanta*, 70(2):455–459, 2006.

[12] A. N. Martin, G. R. Farquar, E. E. Gard, M. Frank, and D. P. Fergenson, "Identification of high explosives using single-particle aerosol mass spectrometry," *Analytical Chemistry*, 79(5):1918–1925, 2007.

[13] G. A. Buttigieg, A. K. Knight, S. Denson, C. Pommier, and M. B. Denton, "Characterization of the explosive triacetone triperoxide and detection by ion mobility spectrometry," *Forensic Science International*, 135(1):53–59, 2003.

[14] B. H. Clowers, W. F. Siems, H. H. Hill, and S. M. Massick, "Hadamard transform ion mobility spectrometry," *Analytical Chemistry*, 78(1):44–51, 2006.

[15] C. Lapthorn, F. Pullen, and B. Z. Chowdhry, "Ion mobility spectrometry–mass spectrometry (IMS–MS) of small molecules: Separating and assigning structures to ions," *Mass Spectrometry Reviews*, 32(1):43–71, 2013.

[16] L. C. Shriver-Lake, P. T. Charles, and A. W. Kusterbeck, "Non-aerosol detection of explosives with a continuous flow immunosensor," *Analytical and Bioanalytical Chemistry*, 377(3):550–555, 2003.

[17] G. P. Anderson and E. R. Goldman, "TNT detection using llama antibodies and a two-step competitive fluid array immunoassay," *Journal of Immunological Methods*, 339(1):47–54, 2008.

[18] O. M. Primera-Pedrozo, Y. M. Soto-Feliciano, L. C. Pacheco-Londono, and S. P. Hernandez-Rivera, "High explosives mixtures detection using fiber optics coupled: Grazing angle probe/Fourier transform reflection absorption infrared spectroscopy," *Sensing and Imaging: An International Journal*, 9(3):27–40, 2008.

[19] S. K. Sharma, A. K. Misra, and B. Sharma, "Portable remote Raman system for monitoring hydrocarbon, gas hydrates and explosives in the environment," *Spectrochimica Acta Part A: Molecular and Biomolecular Spectroscopy*, 61(10):2404–2412, 2005.

[20] J. C. Carter, S. M. Angel, M. Lawrence-Snyder, J. Scaffidi, R. E. Whipple and J. G. Reynolds, "Standoff detection of high explosive materials at 50 meters in ambient light conditions using a small Raman instrument," *Applied Spectroscopy*, 59(6):769–775, 2005.

[21] J. L. Gottfried, F. C. De Lucia Jr, C. A. Munson, and A. W. Miziolek, "Laser-induced breakdown spectroscopy for detection of explosives residues: A review of recent advances, challenges, and future prospects," *Analytical and Bioanalytical Chemistry*, 395(2):283–300, 2009.

[22] D. J. Funk, F. Calgaro, R. D. Averitt, M. L. T. Asaki, and A. J. Taylor, "THz transmission spectroscopy and imaging: Application to the energetic materials PBX 9501 and PBX 9502," *Applied Spectroscopy*, 58(4):428–431, 2004.

[23] Y. C. Shen, T. Lo, P. F. Taday, B. E. Cole, W. R. Tribe, and M. C. Kemp, "Detection and identification of explosives using terahertz pulsed spectroscopic imaging," *Applied Physics Letters*, 86(24):241116, 2005.

[24] N. Palka, "Identification of concealed materials, including explosives, by terahertz reflection spectroscopy," *Optical Engineering*, 53(3):031202, 2014.

[25] J. Otto, M. F. Brown, and W. Long, "Training rats to search and alert on contraband odors," *Applied Animal Behaviour Science*, 77(3):217–232, 2002.

[26] E. S. Carlsten, G. R. Wicks, K. C. Repasky, J. L. Carlsten, J. J. Bromenshenk, and C. B. Henderson, "Field demonstration of a scanning lidar and detection algorithm for spatially mapping honeybees for biological detection of land mines," *Applied Optics*, 50(14):2112–2123, 2011.

[27] T. L. King, F. M. Horine, K. C. Daly, and B. H. Smith, "Explosives detection with hard-wired moths," *IEEE Transactions on Instrumentation and Measurement*, 53(4):1113–1118, 2004.

[28] A. Gordin and A. Amirav, "SnifProbe: New method and device for vapor and gas sampling," *Journal of Chromatography A*, 903(1):155–172, 2000.

[29] R. Batlle, H. Carlsson, P. Tollbaeck, A. Colmsjo, and C. Crescenzi, "Enhanced detection of nitroaromatic explosive vapors combining solid-phase extraction-air sampling, supercritical fluid extraction, and large-volume injection-GC," *Analytical Chemistry*, 75(13):3137–3144, 2003.

[30] A. Amirav, A. Gordin, M. Poliak, and A. B. Fialkov, "Gas chromatography–mass spectrometry with supersonic molecular beams," *Journal of Mass Spectrometry*, 43(2):141–163, 2008.

[31] M. Makinen, M. Nousiainen, and M. Sillanpaa, "Ion spectrometric detection technologies for ultra-traces of explosives: A review," *Mass Spectrometry Reviews*, 30(5):940–973, 2011.

[32] M. Riskin, Y. Ben-Amram, R. Tel-Vered, V. Chegel, J. Almog, and I. Willner, "Molecularly imprinted Au nanoparticles composites on Au surfaces for the surface plasmon resonance detection of pentaerythritol tetranitrate, nitroglycerin, and ethylene glycol dinitrate," *Analytical Chemistry*, 83(8):3082–3088, 2011.

[33] H. Bao, T. Wei, X. Li, Z. Zhao, H. Cui, and P. Zhang, "Detection of TNT by a molecularly imprinted polymer film-based surface plasmon resonance sensor," *Chinese Science Bulletin*, 57(17):2102–2105, 2012.

[34] S. B. Ratner and V. I. Korobov, "Self-heating of plastics during cyclic deformation," *Polymer Mechanics*, 1(3):63–68, 1965.

[35] S. B. Ratner, V. I. Korobov, and S. G. Agamalyan, "Mechanical and thermal fracture of plastics under cyclic strains," *Soviet Materials Science: A Translation of Fiziko-Khimicheskaya Mekhanika Materialov/Academy of Sciences of the Ukrainian SSR*, 5(1):66–70, 1972.

[36] I. K. Senchenkov and V. G. Karnaukhov, "Thermomechanical behavior of nonlinearly viscoelastic materials under harmonic loading," *International Applied Mechanics*, 37(11):1400–1432, 2001.

[37] F. Dinzart, A. Molinari, and R. Herbach, "Thermomechanical response of a viscoelastic beam under cyclic bending; Self-heating and thermal failure," *International Applied Mechanics*, 60(1):59–85, 2008.

[38] M. A. Biot, "Linear thermodynamics and the mechanics of solids," in *Proceedings of the Third U.S. National Congress of Applied Mechanics, Providence, RI, USA*, pp. 1–18, 1958.

[39] R. B. Mignogna, R. E. Green, J. C. Duke, E. G. Henneke, and K. L. Reifsnider, "Thermographic investigation of high-power ultrasonic heating in materials," *Ultrasonics*, 19(4):159–163, 1981.

[40] E. G. Henneke, K. L. Reifsnider, and W. W. Stinchcomb, "Vibrothermography: Investigation, development, and application of a new nondestructive evaluation technique," Virginia Polytechnic Institute and State University, Department of Engineering Science and Mechanics: Report no. AD-A175 373, 1986.

[41] W. Luo, T. Yang, Z. Li, and L. Yuan, "Experimental studies on the temperature fluctuations in deformed thermoplastics with defects," *International Journal of Solids and Structures*, 37(6):887–897, 2000.

[42] J. Renshaw, J. C. Chen, S. D. Holland, and T. R. Bruce, "The sources of heat generation in vibrothermography," *NDT&E International*, 44(8):736–739, 2011.

[43] A. D. Dimarogonas and N. B. Syrimbeis, "Thermal signatures of vibrating rectangular plates," *Journal of Sound and Vibration*, 157(3):467–476, 1992.

[44] J. O. Mares, J. K. Miller, N. D. Sharp, D. S. Moore, D. E. Adams, L. J. Groven, J. F. Rhoads, and S. F. Son, "Thermal and mechanical response of PBX 9501 under contact excitation," *Journal of Applied Physics*, 113(8):084904, 2013.

[45] A. Katunin and M. Fidali, "Experimental identification of non-stationary self-heating characteristics of laminated composite plates under resonant vibration," *Kompozyty*, 11(3):214–219, 2011.

[46] A. Katunin and M. Fidali, "Self-heating of polymeric laminated composite plates under the resonant vibrations: Theoretical and experimental study," *Polymer Composites*, 33(1):138–146, 2012.

[47] T. B. Lewis and L. E. Nielsen, "Dynamic mechanical properties of particulate-filled composites," *Journal of Applied Polymer Science*, 14(6):1449–1471, 1970.

[48] K. Wakashima and H. Tsukamoto, "Mean-field micromechanics model and its application to the analysis of thermomechanical behaviour of composite materials," *Materials Science and Engineering: A*, 146(1):291–316, 1991.

[49] R. Arefinia and A. Shojaei, "On the viscosity of composite suspensions of aluminum and ammonium perchlorate particles dispersed in hydroxyl terminated polybutadiene – New empirical model," *Journal of Colloid and Interface Science*, 299(2):962–971, 2006.

[50] S. Y. Fu, X. Q. Feng, B. Lauke, and Y. W. Mai, "Effects of particle size, particle/matrix interface adhesion and particle loading on mechanical properties of particulate–polymer composites," *Composites Part B: Engineering*, 39(6):933–961, 2008.

[51] J. Paripovic and P. Davies, "Identification of the dynamic behavior of surrogate explosive materials," in *Proceedings of the ASME 2013 International Design Engineering Technical Conferences & Computers and Information in Engineering Conference, 25th Conference on Mechanical Vibration and Noise, Portland, OR, USA*, no. DETC2013-12755, 2013.

[52] J. K. Miller, D. C. Woods, and J. F. Rhoads, "Thermal and mechanical response of particulate composite plates under inertial excitation," *Journal of Applied Physics*, 116(24):244904, 2014.

[53] N. P. Loginov, S. M. Muratov, and N. K. Nazarov, "Initiation of explosion and kinetics of explosive decomposition under vibration," *Combustion, Explosion, and Shock Waves*, 12(3):367–370, 1976.

[54] N. P. Loginov, "Structural and physicochemical changes in RDX under vibration," *Combustion, Explosion, and Shock Waves*, 33(5):598–604, 1997.

[55] J. O. Mares, J. K. Miller, I. E. Gunduz, J. F. Rhoads, and S. F. Son, "Heat generation in an elastic binder system with embedded discrete energetic particles due to high-frequency, periodic mechanical excitation," *Journal of Applied Physics*, 116(20):204902, 2014.

[56] M. W. Chen, S. You, K. S. Suslick, and D. D. Dlott, "Hot spots in energetic materials generated by infrared and ultrasound, detected by thermal imaging microscopy," *Review of Scientific Instruments*, 85(2):023705, 2014.

[57] S. You, M. W. Chen, D. D. Dlott, and K. S. Suslick, "Ultrasonic hammer produces hot spots in solids," *Nature Communications*, 6(4):6581, 2015.

[58] J. K. Miller, J. O. Mares, I. E. Gunduz, S. F. Son, and J. F. Rhoads, "The impact of crystal morphology on the thermal responses of ultrasonically-excited energetic materials," *Journal of Applied Physics*, 119(2):024903, 2016.

[59] F. P. Bowden and A. D. Yoffe, *Initiation and Growth of Explosion in Liquids and Solids*. Cambridge University Press, 1952.

[60] C. L. Mader, "Shock and hot spot initiation of homogeneous explosives," *Physics of Fluids*, 6(3):375–381, 1963.

[61] M. M. Chaudhri and J. E. Field, "The role of rapidly compressed gas pockets in the initiation of condensed explosives," in *Proceedings of the Royal Society of London A: Mathematical, Physical and Engineering Sciences*, 340(1620):113–128, 1974.

[62] G. M. Swallowe and J. E. Field, "The ignition of a thin layer of explosive by impact; The effect of polymer particles," in *Proceedings of the Royal Society of London A: Mathematical, Physical and Engineering Sciences*, 379(1777):389–408, 1982.

[63] N. W. Tschoegl, *The Phenomenological Theory of Linear Viscoelastic Behavior: An Introduction*. Springer-Verlag, 1989.

[64] D. G. Jones, *Handbook of Viscoelastic Vibration Damping*. Wiley, 2001.

[65] H. F. Brinson and L. C. Brinson, *Polymer Engineering Science and Viscoelasticity: An Introduction*. Springer, 2008.

[66] R. D. Borcherdt, *Viscoelastic Waves in Layered Media*. Cambridge University Press, 2009.

[67] G. S. K. Wong, "Approximate equations for some acoustical and thermodynamic properties of standard air," *Journal of the Acoustical Society of Japan E*, 11(3):145–155, 1990.

[68] O. Cramer, "The variation of the specific heat ratio and the speed of sound in air with temperature, pressure, humidity, and CO_2 concentration," *Journal of the Acoustical Society of America*, 93(5):2510–2516, 1993.

[69] H. E. Bass, L. C. Sutherland, A. J. Zuckerwar, D. T. Blackstock, and D. M. Hester, "Atmospheric absorption of sound: Further developments," *Journal of the Acoustical Society of America*, 97(1):680–683, 1995.

[70] J. Yang, N. DeRidder, C. Ume, and J. Jarzynski, "Non-contact optical fibre phased array generation of ultrasound for non-destructive evaluation of materials and processes," *Ultrasonics*, 31(6):387–394, 1993.

[71] M. C. Bhardwaj, "Innovation in non-contact ultrasonic analysis: Applications for hidden objects detection," *Material Research Innovations*, 1(3):188–196, 1997.

[72] J. Peters, V. Kommareddy, Z. Liu, D. Fei, and D. Hsu, "Non-contact inspection of composites using air-coupled ultrasound," in *AIP Conference Proceedings*, 657(22):973–980, 2003.

[73] R. E. Green, "Non-contact ultrasonic techniques," *Ultrasonics*, 42(1):9–16, 2004.

[74] T. H. Gan, P. Pallav, and D. A. Hutchins, "Non-contact ultrasonic quality measurements of food products," *Journal of Food Engineering*, 77(2):239–247, 2006.

[75] S. Meyer, S. A. Hindle, J. P. Sandoz, T. H. Gan, and D. A. Hutchins, "Non-contact evaluation of milk-based products using air-coupled ultrasound," *Measurement Science and Technology*, 17(7):1838–1846, 2006.

[76] G. Rousseau, B. Gauthier, A. Blouin, and J. P. Monchalin, "Non-contact biomedical photoacoustic and ultrasound imaging," *Journal of Biomedical Optics*, 17(6):061217, 2012.

[77] L. M. Brekhovskikh, *Waves in Layered Media*. Academic Press, 1960.

[78] L. E. Kinsler, A. R. Frey, A. B. Coppens, and J. V. Sanders, *Fundamentals of Acoustics*. John Wiley & Sons, 1999.

[79] R. J. Urick, "Noise signature of an aircraft in level flight over a hydrophone in the sea," *Journal of the Acoustical Society of America*, 52(3B):993–999, 1972.

[80] R. J. Urick, *Principles of Underwater Sound*. McGraw-Hill, 1983.

[81] W. J. Richardson, C. R. Greene Jr, C. I. Malme, and D. H. Thomson, *Marine Mammals and Noise*. Academic Press, 1995.

[82] D. L. Lansing and D. J. Maglieri, "Comparison of measured and calculated sonic-boom ground patterns due to several different aircraft maneuvers," NASA Langley Research Center: Report no. NASA-TN-D-2730, 1965.

[83] D. J. Maglieri, D. A. Hilton, and N. J. McLeod, "Experiments on the effects of atmospheric refraction and airplane accelerations on sonic-boom ground-pressure patterns," NASA Langley Research Center: Report no. NASA-TN-D-3520, 1966.

[84] M. Downing, N. Zamot, C. Moss, D. Morin, E. Wolski, S. Chung, K. Plotkin, and D. Maglieri, "Controlled focused sonic booms from maneuvering aircraft," *Journal of the Acoustical Society of America*, 104(1):112–121, 1998.

[85] D. M. F. Chapman and P. D. Ward, "The normal-mode theory of air-to-water sound transmission in the ocean," *Journal of the Acoustical Society of America*, 87(2):601–618, 1990.

[86] D. M. F. Chapman, D. J. Thomson, and D. D. Ellis, "Modeling air-to-water sound transmission using standard numerical codes of underwater acoustics," *Journal of the Acoustical Society of America*, 91(4):1904–1910, 1992.

[87] N. N. Komissarova, "Sound field features in the coastal zone of a shallow sea with an airborne source of excitation," *Acoustical Physics*, 47(3):313–322, 2001.

[88] Z. Y. Zhang, "Modelling of sound transmission from air into shallow and deep waters," in *Proceedings of the Australian Acoustical Society Conference, Adelaide, Australia*, pp. 234–243, 2002.

[89] H. K. Cheng and C. J. Lee, "Sonic-boom noise penetration under a wavy ocean: Theory," *Journal of Fluid Mechanics*, 514(9):281–312, 2004.

[90] O. A. Godin, "Anomalous transparency of the water–air interface for low-frequency sound," *Journal of the Acoustical Society of America*, 119(5):3253–3253, 2006.

[91] O. A. Godin, "Low-frequency sound transmission through a gas–liquid interface," *Journal of the Acoustical Society of America*, 123(4):1866–1879, 2008.

[92] O. A. Godin, "Low-frequency sound transmission through a gas–solid interface," *Journal of the Acoustical Society of America*, 129(2):EL45–EL51, 2011.

[93] B. E. McDonald and D. C. Calvo, "Enhanced sound transmission from water to air at low frequencies," *Journal of the Acoustical Society of America*, 122(6):3159–3161, 2007.

[94] D. C. Calvo, M. Nicholas, and G. J. Orris, "Experimental verification of enhanced sound transmission from water to air at low frequencies," *Journal of the Acoustical Society of America*, 134(5):3403–3408, 2013.

[95] D. Trivett, L. Luker, S. Petrie, A. Van Buren, and J. Blue, "A planar array for the generation of evanescent waves," *Journal of the Acoustical Society of America*, 87(6):2535–2540, 1990.

[96] T. J. Matula and P. L. Marston, "Electromagnetic acoustic wave transducer for the generation of acoustic evanescent waves on membranes and optical and capacitor wave-number selective detectors," *Journal of the Acoustical Society of America*, 93(4):2221–2227, 1993.

[97] M. Deschamps, "Reflection and refraction of the evanescent plane wave on plane interfaces," *Journal of the Acoustical Society of America*, 96(5):2841–2848, 1994.

[98] H. Itou, K. Furuya, and Y. Haneda, "Evanescent wave reproduction using linear array of loudspeakers," in *Proceedings of the IEEE Workshop on Applications of Signal Processing to Audio and Acoustics, New Paltz, NY, USA*, pp. 37–40, 2011.

[99] A. Fujii, N. Wakatsuki, and K. Mizutani, "A planar acoustic transducer for near field acoustic communication using evanescent wave," *Japanese Journal of Applied Physics*, 53(7):07KB07, 2014.

[100] M. Hayes, "Energy flux for trains of inhomogeneous plane waves," in *Proceedings of the Royal Society of London, Series A: Mathematical and Physical Sciences*, 370(1742):417–429, 1980.

[101] O. Leroy, G. Quentin, and J. Claeys, "Energy conservation for inhomogeneous plane waves," *Journal of the Acoustical Society of America*, 84(1):374–378, 1988.

[102] R. D. Borcherdt, "Energy and plane waves in linear viscoelastic media," *Journal of Geophysical Research*, 78(14):2442–2453, 1973.

[103] R. D. Borcherdt and L. Wennerberg, "General P, type-I S, and type-II S waves in anelastic solids: Inhomogeneous wave fields in low-loss solids," *Bulletin of the Seismological Society of America*, 75(6):1729–1763, 1985.

[104] P. W. Buchen, "Plane waves in linear viscoelastic media," *Geophysical Journal International*, 23(5):531–542, 1971.

[105] L. Wennerberg and G. Glassmoyer, "Absorption effects on plane waves in layered media," *Bulletin of the Seismological Society of America*, 76(5):1407–1432, 1986.

[106] F. J. Lockett, "The reflection and refraction of waves at an interface between viscoelastic materials," *Journal of the Mechanics and Physics of Solids*, 10(1):53–64, 1962.

[107] H. F. Cooper, Jr. and E. L. Reiss, "Reflection of plane viscoelastic waves from plane boundaries," *Journal of the Acoustical Society of America*, 39(6):1133–1138, 1966.

[108] H. F. Cooper, Jr., "Reflection and transmission of oblique plane waves at a plane interface between viscoelastic media," *Journal of the Acoustical Society of America*, 42(5):1064–1069, 1967.

[109] M. Schoenberg, "Transmission and reflection of plane waves at an elastic–viscoelastic interface," *Geophysical Journal International*, 25(1–3):35–47, 1971.

[110] R. D. Borcherdt, "Reflection–refraction of general P- and type-I S-waves in elastic and anelastic solids," *Geophysical Journal International*, 70(3):621–638, 1982.

[111] H. L. Bertoni and T. Tamir, "Unified theory of Rayleigh-angle phenomena for acoustic beams at liquid–solid interfaces," *Applied Physics*, 2(4):157–172, 1973.

[112] A. N. Norris, "Back reflection of ultrasonic waves from a liquid–solid interface," *Journal of the Acoustical Society of America*, 73(2):427–434, 1983.

[113] T. Tamir and H. L. Bertoni, "Lateral displacement of optical beams at multilayered and periodic structures," *Journal of the Optical Society of America*, 61(10):1397–1413, 1971.

[114] M. A. Breazeale, L. Adler, and L. Flax, "Reflection of a Gaussian ultrasonic beam from a liquid–solid interface," *Journal of the Acoustical Society of America*, 56(3):866–872, 1974.

[115] M. A. Breazeale, L. Adler, and G. W. Scott, "Interaction of ultrasonic waves incident at the Rayleigh angle onto a liquid–solid interface," *Journal of Applied Physics*, 48(2):530–537, 1977.

[116] T. D. Ngoc and W. G. Mayer, "Numerical integration method for reflected beam profiles near Rayleigh angle," *Journal of the Acoustical Society of America*, 67(4):1149–1152, 1980.

[117] S. Vanaverbeke, F. Windels, and O. Leroy, "The reflection of bounded inhomogeneous waves on a liquid/solid interface," *Journal of the Acoustical Society of America*, 113(1):73–83, 2003.

[118] K. Van Den Abeele and O. Leroy, "On the influence of frequency and width of an ultrasonic bounded beam in the investigation of materials: Study in terms of heterogeneous plane waves," *Journal of the Acoustical Society of America*, 93(5):2688–2699, 1993.

[119] N. F. Declercq and O. Leroy, "A feasibility study of the use of bounded beams resembling the shape of evanescent and inhomogeneous waves," *Ultrasonics*, 51(6):752–757, 2011.

[120] D. C. Woods, J. K. Miller, and J. F. Rhoads, "On the thermomechanical response of HTPB composite beams under near-resonant base excitation," in *Proceedings of the ASME 2014 International Design Engineering Technical Conferences & Computers and Information in Engineering Conference, 26th Conference on Mechanical Vibration and Noise, Buffalo, NY, USA*, no. DETC2014-34516, 2014.

[121] D. C. Woods, J. K. Miller, and J. F. Rhoads, "On the thermomechanical response of HTPB-based composite beams under near-resonant excitation," *Journal of Vibration and Acoustics*, 137(5):054502, 2015.

[122] H. Markovitz, "Boltzmann and the beginnings of linear viscoelasticity," *Journal of Rheology*, 21(3):381–398, 1977.

[123] S. S. Rao, *Vibration of Continuous Systems*. John Wiley & Sons, 2007.

[124] S. P. Timoshenko and J. N. Goodier, *Theory of Elasticity*. McGraw-Hill, 1951.

[125] F. .P Incropera, D. P. DeWitt, T. L. Bergman, and A. S. Lavine, *Introduction to Heat Transfer*. John Wiley & Sons, 2007.

[126] J. V. Beck, K. D. Cole, A. Haji-Sheikh, and B. Litkouhi, *Heat Conduction Using Green's Functions*. Hemisphere Publishing Corporation, 1992.

[127] F. P. Beer, E. R. Johnston, J. T. DeWolf, and D. F. Mazurek, *Mechanics of Materials*. McGraw-Hill, 2009.

[128] J. Paripovic, Personal Communication, 2013.

[129] M. Paz, *Structural Dynamics: Theory and Computation*. Springer, 1997.

[130] S. E. Gustafsson, "Transient plane source techniques for thermal conductivity and thermal diffusivity measurements of solid materials," *Review of Scientific Instruments*, 62(3):797–804, 1991.

[131] B. R. Rich, "An investigation of heat transfer from an inclined flat plate in free convection," *Transactions of ASME*, 75:489–499, 1953.

[132] G. C. Vliet, "Natural convection local heat transfer on constant-heat-flux inclined surfaces," *Journal of Heat Transfer*, 91(4):511–516, 1969.

[133] R. J. Goldstein, E. M. Sparrow, and D. C. Jones, "Natural convection mass transfer adjacent to horizontal plates," *International Journal of Heat and Mass Transfer*, 16(5):1025–1035, 1973.

[134] C. M. Tarver, S. K. Chidester, and A. L. Nichols, "Critical conditions for impact- and shock-induced hot spots in solid explosives," *Journal of Physical Chemistry*, 100(14):5794–5799, 1996.

[135] E. C. Mattos, E. D. Moreira, R. C. L. Dutra, M. F. Diniz, A. P. Ribeiro, and K. Iha, "Determination of the HMX and RDX content in synthesized energetic material by HPLC, FT-MIR, and FT-NIR spectroscopies," *Química Nova*, 27(4):540–544, 2004.

[136] J. O. Mares, D. C. Woods, C. E. Baker, S. F. Son, J. F. Rhoads, J. S. Bolton, and M. Gonzalez, "Localized heating due to stress concentrations induced in a lossy elastic medium via the scattering of compressional waves by a rigid spherical inclusion," in *Proceedings of the ASME 2016 International Mechanical Engineering Congress & Exposition, Phoenix, AZ, USA*, no. IMECE2016-68219, 2016.

[137] J. O. Mares, D. C. Woods, C. E. Baker, S. F. Son, J. F. Rhoads, J. S. Bolton, and M. Gonzalez, "Localized heating near a rigid spherical inclusion in a viscoelastic binder material under compressional plane wave excitation," *Journal of Applied Mechanics*, Submitted, 2016.

[138] C. F. Ying and R. Truell, "Scattering of a plane longitudinal wave by a spherical obstacle in an isotropically elastic solid," *Journal of Applied Physics*, 27(9):1086–1097, 1956.

[139] Y. H. Pao and C. C. Mow, "Scattering of plane compressional waves by a spherical obstacle," *Journal of Applied Physics*, 34(3):493–499, 1963.

[140] S. A. Thau, "Radiation and scattering from a rigid inclusion in an elastic medium," *Journal of Applied Mechanics*, 34(2):509–511, 1967.

[141] C. C. Mow and Y. H. Pao, "The diffraction of elastic waves and dynamic stress concentrations," United States Air Force Project RAND: Report no. R-482-PR, 1971.

[142] M. A. Oien and Y. H. Pao, "Scattering of compressional waves by a rigid spheroidal inclusion," *Journal of Applied Mechanics*, 40(4):1073–1077, 1973.

[143] G. C. Gaunaurd and H. Uberall, "Theory of resonant scattering from spherical cavities in elastic and viscoelastic media," *Journal of the Acoustical Society of America*, 63(6):1699–1712, 1978.

[144] A. Beltzer, B. Robinson, and N. Rudy, "The effect of random compressional waves on a rigid sphere embedded in an elastic medium," *Journal of Sound and Vibration*, 66(4):513–519, 1979.

[145] A. I. Beltzer, "Random response of a rigid sphere embedded in a viscoelastic medium and related problems," *Journal of Applied Mechanics*, 47(3):499–503, 1980.

[146] J. P. Sessarego, J. Sageloli, R. Guillermin, and H. Uberall, "Scattering by an elastic sphere embedded in an elastic isotropic medium," *Journal of the Acoustical Society of America*, 104(5):2836–2844, 1998.

[147] R. Avila-Carrera and F. J. Sanchez-Sesma, "Scattering and diffraction of elastic P- and S-waves by a spherical obstacle: A review of the classical solution," *Geofsica Internacional*, 45(1):3–21, 2006.

[148] T. R. Tauchert, "Heat generation in a viscoelastic solid," *Acta Mechanica*, 3(4):385–396, 1967.

[149] O. P. Chervinko and I. K. Senchenkov, "The coupled thermomechanical state of a notched viscoelastic rectangular plate under harmonic loading," *International Applied Mechanics*, 38(2):209–216, 2002.

[150] O. P. Chervinko, "Calculating the critical parameters characterizing the thermal instability of a viscoelastic prism with a stress concentrator under harmonic compression," *International Applied Mechanics*, 40(8):916–922, 2004.

[151] O. P. Chervinko, I. K. Senchenkov, and N. N. Yakimenko, "Vibrations and self-heating of a viscoelastic prism with a cylindrical inclusion," *International Applied Mechanics*, 43(6):647–653, 2007.

[152] C. Zener, "Internal friction in solids II: General theory of thermoelastic internal friction," *Physical Review*, 53(1):90–99, 1938.

[153] E. C. Ting, "Dissipation function of a viscoelastic material with temperature-dependent properties," *Journal of Applied Physics*, 44(11):4956–4960, 1973.

[154] J. E. Bishop and V. K. Kinra, "Equivalence of the mechanical and entropic descriptions of elastothermodynamic damping in composite materials," *Mechanics of Composite Materials and Structures*, 3(2):83–95, 1996.

[155] R. Lakes, "Thermoelastic damping in materials with a complex coefficient of thermal expansion," *Journal of the Mechanical Behavior of Materials*, 8(3):201–216, 1997.

[156] B. Bradie, *A Friendly Introduction to Numerical Analysis*. Pearson Prentice Hall, 2006.

[157] Dow Corning Corporation, *Information about High Technology Materials Sylgard® 182 & 184 Silicone Elastomers*. Data sheet no. 61-113C-01, 1986.

[158] Dow Corning Corporation, *Product Information, Sylgard® 184 Silicone Elastomer*. Data sheet no. 11-3184B-01, 2014.

[159] Los Alamos Data Center for Dynamic Material Properties (eds. T. R. Gibbs and A. Popolato), *LASL Explosive Property Data*. University of California Press, 1980.

[160] T. Shepodd, R. Behrens, D. Anex, D. Miller, and K. Anderson, "Degradation chemistry of PETN and its homologues," Sandia National Laboratories: Report no. SAND-97-8684C, 1997.

[161] J. C. F. Millett, G. Whiteman, S. M. Stirk, and N. K. Bourne, "Shear strength measurements in a shock loaded commercial silastomer," *Journal of Applied Physics*, 44(18):185403, 2011.

[162] K. A. Garvin, D. C. Hocking, and D. Dalecki, "Controlling the spatial organization of cells and extracellular matrix proteins in engineered tissues using ultrasound standing wave fields," *Ultrasound in Medicine & Biology*, 36(11):1919–1932, 2010.

[163] T. Pritz, "Frequency dependences of complex moduli and complex Poisson's ratio of real solid materials," *Journal of Sound and Vibration*, 214(1):83–104, 1998.

[164] T. Pritz, "Measurement methods of complex Poisson's ratio of viscoelastic materials," *Applied Acoustics*, 60(3):279–292, 2000.

[165] J. P. Agrawal, *High Energy Materials: Propellants, Explosives and Pyrotechnics*. John Wiley & Sons, 2010.

[166] P. M. Morse and K. U. Ingard, *Theoretical Acoustics*. McGraw-Hill, 1968.

[167] D. C. Woods, J. S. Bolton, and J. F. Rhoads, "On the use of evanescent plane waves for low-frequency energy transmission across material interfaces," *Journal of the Acoustical Society of America*, 138(4):2062–2078, 2015.

[168] J. W. Strutt, "On waves propagated along the plane surface of an elastic solid," in *Proceedings of the London Mathematical Society*, 17(1):4–11, 1885.

[169] J. D. N. Cheeke, *Fundamentals and Applications of Ultrasonic Waves*. CRC Press, 2012.

[170] R. T. Beyer and S. V. Letcher, *Physical Ultrasonics*. Academic Press, 1969.

[171] F. L. Becker and R. L. Richardson, "Critical-angle reflectivity," *Journal of the Acoustical Society of America*, 45(3):793–794, 1969.

[172] F. L. Becker and R. L. Richardson, "Influence of material properties on Rayleigh critical-angle reflectivity," *Journal of the Acoustical Society of America*, 51(5B):1609–1617, 1972.

[173] D. C. Woods, J. S. Bolton, and J. F. Rhoads, "Enhanced acoustic transmission into dissipative solid materials through the use of inhomogeneous plane waves," in *Proceedings of the 12th International Conference on Recent Advances in Structural Dynamics, Southampton, England, United Kingdom*, no. RASD2016-2600, 2016.

[174] D. C. Woods, J. S. Bolton, and J. F. Rhoads, "Enhanced acoustic transmission into dissipative solid materials through the use of inhomogeneous plane waves," *Journal of Physics: Conference Series*, 744(1):012188, 2016.

[175] T. L. Szabo and J. Wu, "A model for longitudinal and shear wave propagation in viscoelastic media," *Journal of the Acoustical Society of America*, 107(5):2437–2446, 2000.

[176] D. C. Woods, J. S. Bolton, and J. F. Rhoads, "Bounded inhomogeneous wave profiles for increased surface wave excitation efficiency at fluid–solid interfaces," *Journal of the Acoustical Society of America*, Submitted, 2016.

[177] L. Gao, K. J. Parker, R. M. Lerner, and S. F. Levinson, "Imaging of the elastic properties of tissue: A review," *Ultrasound in Medicine & Biology*, 22(8):959–977, 1996.

VITA

VITA

Daniel Woods was raised in Carrollton, Kentucky. He completed his Bachelor of Science in Mechanical Engineering in May of 2012 at the University of Kentucky in Lexington, Kentucky. After starting the Direct-PhD program in August of 2012, he received his Master of Science in Mechanical Engineering from Purdue University in 2014.

Journal Publications

- **D. C. Woods**, T. A. Kyle, R. Tiwari, J. S. Bolton, and J. F. Rhoads, "The generation of low-frequency wave profiles by a linear acoustic array for improved surface wave excitation efficiency at fluid–solid interfaces," *Journal of the Acoustical Society of America*, In preparation, 2016.
- J. O. Mares, **D. C. Woods**, C. E. Baker, S. F. Son, J. F. Rhoads, J. S. Bolton, and M. Gonzalez, "Localized heating near a rigid spherical inclusion in a viscoelastic binder material under compressional plane wave excitation," *Journal of Applied Mechanics*, Submitted, 2016.
- **D. C. Woods**, J. S. Bolton, and J. F. Rhoads, "Bounded inhomogeneous wave profiles for increased surface wave excitation efficiency at fluid–solid interfaces," *Journal of the Acoustical Society of America*, Submitted, 2016.
- **D. C. Woods**, J. S. Bolton, and J. F. Rhoads, "Enhanced acoustic transmission into dissipative solid materials through the use of inhomogeneous plane waves," *Journal of Physics: Conference Series*, 744(1):012188, 2016.
- **D. C. Woods**, J. S. Bolton, and J. F. Rhoads, "On the use of evanescent plane waves for low-frequency energy transmission across material interfaces," *Journal of the Acoustical Society of America*, 138(4):2062–2078, 2015.

- **D. C. Woods**, J. K. Miller, and J. F. Rhoads, "On the thermomechanical response of HTPB-based composite beams under near-resonant excitation," *Journal of Vibration and Acoustics*, 137(5):054502, 2015.
- J. K. Miller, **D. C. Woods**, and J. F. Rhoads, "Thermal and mechanical response of particulate composite plates under inertial excitation," *Journal of Applied Physics*, 116(24):244904, 2014.
- S. Malkowski, R. Adhikari, J. Boissevain, C. Daurer, B. Filippone, B. Hona, B. Plaster, **D. Woods**, and H. Yan, "Overlap technique for end-cap seals on cylindrical magnetic shields," *IEEE Transactions on Magnetics*, 49(1):651–653, 2013.
- S. Malkowski, R. Adhikari, B. Hona, C. Mattie, **D. Woods**, H. Yan, and B. Plaster, "Technique for high axial shielding factor performance of large-scale, thin, open-ended, cylindrical Metglas magnetic shields," *Review of Scientific Instruments*, 82(7):075104, 2011.

Conference Proceedings

- J. O. Mares, **D. C. Woods**, C. E. Baker, S. F. Son, J. F. Rhoads, J. S. Bolton, and M. Gonzalez, "Localized heating due to stress concentrations induced in a lossy elastic medium via the scattering of compressional waves by a rigid spherical inclusion," in *Proceedings of the ASME 2016 International Mechanical Engineering Congress & Exposition, Phoenix, AZ, USA*, no. IMECE2016-68219, 2016.
- **D. C. Woods**, J. S. Bolton, and J. F. Rhoads, "The construction of acoustic waveforms from plane wave components to enhance energy transmission into solid media," in *Proceedings of the ASME 2016 International Design Engineering Technical Conferences & Computers and Information in Engineering Conference, 28th Conference on Mechanical Vibration and Noise, Charlotte, NC, USA*, no. DETC2016-59272, 2016.

- **D. C. Woods**, J. S. Bolton, and J. F. Rhoads, "Enhanced acoustic transmission into dissipative solid materials through the use of inhomogeneous plane waves," in *Proceedings of the 12th International Conference on Recent Advances in Structural Dynamics, Southampton, England, United Kingdom*, no. RASD2016-2600, 2016.
- **D. C. Woods**, J. S. Bolton, and J. F. Rhoads, "Low-frequency energy transmission across material interfaces using incident evanescent waves," in *Proceedings of the ASME 2015 International Design Engineering Technical Conferences & Computers and Information in Engineering Conference, 27th Conference on Mechanical Vibration and Noise, Boston, MA, USA*, no. DETC2015-46533, 2015.
- **D. C. Woods**, J. K. Miller, and J. F. Rhoads, "On the thermomechanical response of HTPB composite beams under near-resonant base excitation," in *Proceedings of the ASME 2014 International Design Engineering Technical Conferences & Computers and Information in Engineering Conference, 26th Conference on Mechanical Vibration and Noise, Buffalo, NY, USA*, no. DETC2014-34516, 2014.

Conference Abstracts

- **D. C. Woods**, J. S. Bolton, and J. F. Rhoads, "Stress and energy transmission by inhomogeneous plane waves into dissipative media." *The 170th Meeting of the Acoustical Society of America, Jacksonville, FL, USA*, no. 5aPA8, 2015.
- **D. C. Woods**, J. S. Bolton, and J. F. Rhoads, "Use of evanescent plane waves for low-frequency energy transmission across material interfaces." *The 169th Meeting of the Acoustical Society of America, Pittsburgh, PA, USA*, no. 1aPA6, 2015.
- **D. C. Woods**, J. K. Miller, and J. F. Rhoads, "Thermomechanical response of HTPB-based composite beams subjected to near-resonant inertial excita-

tion." *The 51st Annual Society of Engineering Science Technical Meeting, West Lafayette, IN, USA*, no. 1075, 2014.

- **D. C. Woods**, "Overview of Dr. L. L. Beranek's 2006 paper on Analysis of Sabine and Eyring equations and their application to concert hall audience and chair absorption." *The 2014 U.S. National Conference on Noise Control Engineering, Fort Lauderdale, FL, USA*, no. NC14-180, 2014.
- **D. C. Woods**, J. K. Miller, and J. F. Rhoads, "Thermomechanical response of HTPB composite beams under resonant inertial excitation." *The 17th U.S. National Congress on Theoretical and Applied Mechanics, East Lansing, MI, USA*, no. D-02-650, 2014.